INFORMATION TO USERS

This manuscript has been reproduced from the microfilm master. UMI films the text directly from the original or copy submitted. Thus, some thesis and dissertation copies are in typewriter face, while others may be from any type of computer printer.

The quality of this reproduction is dependent upon the quality of the copy submitted. Broken or indistinct print, colored or poor quality illustrations and photographs, print bleedthrough, substandard margins, and improper alignment can adversely affect reproduction.

In the unlikely event that the author did not send UMI a complete manuscript and there are missing pages, these will be noted. Also, if unauthorized copyright material had to be removed, a note will indicate the deletion.

Oversize materials (e.g., maps, drawings, charts) are reproduced by sectioning the original, beginning at the upper left-hand corner and continuing from left to right in equal sections with small overlaps.

Photographs included in the original manuscript have been reproduced xerographically in this copy. Higher quality 6" x 9" black and white photographic prints are available for any photographs or illustrations appearing in this copy for an additional charge. Contact UMI directly to order.

ProQuest Information and Learning
300 North Zeeb Road, Ann Arbor, MI 48106-1346 USA
800-521-0600

UMI®

Reproduced with permission of the copyright owner. Further reproduction prohibited without permission.

University of Alberta

Micro-Mechanics of Emulsion Drops

by

Kevin Leslie Moran ©

A thesis submitted to the Faculty of Graduate Studies and Research in partial fulfillment
of the requirements for the degree of Doctor of Philosophy

in

Chemical Engineering

Department of Chemical and Materials Engineering

Edmonton, Alberta
Fall, 2001

National Library
of Canada

Acquisitions and
Bibliographic Services

395 Wellington Street
Ottawa ON K1A 0N4
Canada

Bibliothèque nationale
du Canada

Acquisitions et
services bibliographiques

395, rue Wellington
Ottawa ON K1A 0N4
Canada

Your file Votre référence

Our file Notre référence

0-612-68975-1

University of Alberta

Library Release Form

Name of Author: Kevin Leslie Moran

Title of Thesis: Micro-Mechanics of Emulsion Drops

Degree: Doctor of Philosophy

Year this Degree Granted: 2001

Kevin Moran

Kevin Moran
303 – 8640 108 Street
Edmonton, AB
T6E 4M4

August 10, 2001

University of Alberta

Faculty of Graduate Studies and Research

The undersigned certify that they have read, and recommend to the Faculty of Graduate Studies and Research for acceptance, a thesis entitled *Micro-Mechanics of Emulsion Drops* in partial fulfillment of the requirements for the degree of Doctor of Philosophy in Chemical Engineering.

Dr. Jacob H. Masliyah (supervisor)

Dr. Anthony K.C. Yeung (supervisor)

Janet Elliott

Dr. Janet A.W. Elliott

Daniel Kwok

Dr. Daniel Y. Kwok

Dr. Krishnaswamy Nandakumar

Dr. Lee R. White (external examiner)

Date: August 3, 2001

Abstract

A fundamental appreciation for the mechanics of emulsion drops is essential to understanding many processes, such as emulsification. Experiments have suggested that the mechanical properties at emulsion drop surfaces may be size-dependent and must therefore be studied using micron-scale techniques. To date, no such work has been reported in the literature.

Novel micron-scale techniques are developed to explore the mechanical behaviour of emulsion drops. The method involves glass capillaries (micropipettes) whose tips are typically several microns in diameter. One micropipette is shaped into a cantilever to allow for direct force measurements. In a static technique, stress-strain behaviour is noted by capturing and deforming a single emulsion drop between two micropipettes. Alternatively, the dynamic shape recovery of a deformed drop upon release from one micropipette is observed. Based on these experiments, the mechanical properties of emulsion drops can be evaluated *in situ*.

The interfacial tension and viscosity of bitumen (a heavy crude oil) drops in aqueous environments are quantified using micropipette techniques; these are measurements that have not been attainable with traditional methods. In addition, this is the first study to document the surface plasticity of bitumen drops in an aqueous environment expected to be detrimental to the extraction of bitumen from oil sands on a commercial scale.

This research presents novel methods to examine the mechanics of emulsion drops *in situ*. Results from this research will allow for improved insights into the microrheology of emulsions and may contribute to advances in emulsion technologies.

Acknowledgements

Many thanks are extended to my supervisors, Drs. **Jacob Masliyah** and **Anthony Yeung**, for their encouragement and support. I sincerely appreciate their enthusiasm towards advising me in, and teaching the finer details of, this project. Their sharp insights and expertise in physical phenomena and interfacial science are invaluable. I am indebted to Dr. **Jan Czarnecki**, of Syncrude Canada, for guidance, stimulating discussions and providing a truly outstanding environment for research and learning. I also would like to thank my peers and colleagues at the University of Alberta and the Syncrude Research Centre; they helped to make my experience most enjoyable.

This study was possible due to the financial assistance of many organizations. Scholarships provided by the National Science and Engineering Research Council (NSERC), the University of Alberta and Petro-Canada are gratefully acknowledged. In addition, aid through the NSERC Industrial Research Chair in Oil Sands Engineering, held by Dr. Masliyah, allowed this research to be conducted at the Syncrude Edmonton Research Centre, offering a unique and wonderful experience.

Finally, I wish to thank my wife, **Kathryn**, for her understanding, patience and support.

Table of Contents

List of Tables

Chapter 2

Chapter 4

Chapter 6

List of Figures

Chapter 2

Chapter 3

Chapter 4

Chapter 5

Chapter 6

Appendices

Nomenclature

a	series coefficient set, $\{a\} = [\Pi, A_n, B_n, C_n, D_n]$, $n \geq 2$	(-)
A	area	(m^2)
b	cylindrical diameter	(m)
B_o	Bond number, $B_o = \Delta\rho g R_d^2/\gamma$	(-)
Br	Brinkman number, $Br = (\mu[dL/dt]^2)/(k_T\Delta T)$	(-)
C_p	specific heat capacity	(m^2/s^2K)
D	diffusion coefficient	(m^2/s)
E	energy per unit volume	($kg/m\ s^2$)
f	applied force	($kg\ m/s^2$)
F_y	surface plastic stress	(kg/s^2)
G	drop extension rate, ~ $d\ln L/dt$	(s^{-1})
I_n	Gegenbauer function of order n	(-)
J	mean drop curvature, $J = 1/R_1 + 1/R_2$	(m^{-1})
k	Boltzmann constant, $k = 1.381 \times 10^{-23}$ J/K	($kg\ m^2/s^2K$)
k_b	cantilever stiffness	(kg/s^2)
k_T	thermal conductivity	($kg\ m/s^3K$)
L	axial drop length	(m)
N	number of terms in series solutions (equations 4.6 and 4.7)	(m)
p	pressure field	($kg/m\ s^2$)
P_n	Legendre polynomial of order n	(-)
r	cylindrical coordinate	(m)
R	spherical coordinate	(m)
R_a	effective radius of an aggregate	(m)
R_d	spherical drop radius	(m)
R_1	merdional radius of curvature (in s direction)	(m)
R_2	azimuthal radius of curvature (about z axis)	(m)
s	curvilinear distance along drop surface, from $z = 0$	(m)
t	time	(s)

T	temperature	(K, °C)
$\boldsymbol{T}$	capillary stress vector	(kg/ms^2)
$\boldsymbol{u}$	velocity field	(m/s)
W	Weber number, $W = \mu G R_d / \gamma$	(-)
V	volume	(m^3)
x	mean diffusion path length	(m)
z	cylindrical coordinate, axis of symmetry	(m)

Greek

ε	error functional	
ϕ	angle between axisymmetric axis (z) and spherical coordinate R	(-)
γ	interfacial tension	(kg/s^2)
λ	viscosity ratio, $\lambda = \mu / \bar{\mu}$	(-)
μ	dynamic viscosity	(kg/ms)
ρ	density	(kg/m^3)
σ	hydrodynamic stress tesnsor	(kg/ms^2)
θ	spherical coordinate	(-)
υ_1, υ_2	projected volume	(m^3)
ψ	transformation angle	(-)

Subscripts

c	critical
f	final
i	reference point
o	maximum, initial

Superscripts

–	external phase
*	dimensionless

Chapter 1

Introduction

Emulsions (or, more precisely, macroemulsions) are colloidal systems in which at least one liquid is dispersed as drops throughout an immiscible liquid. In such systems, the drops are on the order of one to ten microns in radius (Hunter, 1986; Davis, 1988). The significance of emulsions cannot be underestimated as they are common to the food (Krog et al., 1985; Dalgleish, 2001), pharmaceutical (Mulley, 1974), petrochemical (Matsumoto, 1974) and petroleum (Graham, 1988; Czarnecki, 2001; Salager et al., 2001) industries, among others. Emulsion rheology[1] is of consequence to many technological processes. Some emulsions provide an energy efficient means to transport viscous oils (Zakin et al., 1979), while the flow behaviour of crude oil-water emulsions is important to crude oil production (Simon and Poynter, 1968; Davis, 1988; Nunez et al., 2000).

As lyophobic (solvent-hating) colloids, emulsions are thermodynamically unstable since the interfacial area represents an extra energy cost. As such, there is a tendency to minimize surface area, through drop coalescence, leading to phase separation (demulsification). However, some surfactants and lyophilic substances can provide a degree of kinetic stability to emulsions. These species may sterically inhibit drop coalescence by preventing direct contact, and by resisting drainage of thin continuous phase films between emulsion drops[2] (Hunter, 1986; Everett, 1988). Surfactants, such as fatty acid soaps, are characterized by polar groups and paraffinic chains. Due to their amphiphilic nature, surfactants have a high affinity for interfaces and preferentially adsorb at drop surfaces to minimize the free energy of an emulsion. Interfacially adsorbed substances which stabilize emulsions also include macromolecules (proteins and polymers) and even solid particles. The extent of adsorption of these materials at drop surfaces is dictated by surface activities or wetting characteristics (Shaw, 1970;

---

[1] Rheology is the study of material deformation and flow in response to applied mechanical stress (Hunter, 1986).

[2] From a thermodynamic perspective, stability is provided since work must be done to displace adsorbates from drop surfaces. Note that stability may be compromised by other higher affinity surfactants that can promote demulsification (by displacing adsorbed stabilizing agents).

Adamson, 1976). Once adsorbed, these stabilizing agents can alter the mechanical properties at emulsion drop surfaces (Hunter, 1986). In doing so, the mechanical behaviour of the emulsion drops is also affected.

Processes such as drop coalescence and emulsification are influenced by the mechanics of emulsion drops. In addition, emulsion rheology is a direct result of the interactions between stabilized emulsion drops and depends on many factors. These factors include the disperse phase volume fraction, the rheology of both disperse and continuous phase liquids, and the surface properties of the emulsion drops (Walstra, 1974; Sherman, 1983; Tadros, 1994). Theories describing the viscosity of dilute emulsions reflect these properties while assuming that the emulsion drops remain nearly spherical (Taylor, 1932; Oldroyd, 1955; Danov, 2001). However, the close proximity of emulsion drops observed in concentrated emulsions or during drop coalescence indicates that the drops may be forced into non-spherical shapes (Nunez et al., 2000; Princen, 2001). Also, highly non-spherical drop shapes are observed during emulsification processes (Grace, 1982; Walstra, 1993). Understanding the mechanics of emulsion drop deformations will provide fresh insights into emulsion rheology and related processes.

As noted above, the surface properties of emulsion drops are important to many emulsion phenomena and are affected by adsorbed species. The most fundamental property of any liquid-liquid interface is the interfacial tension, defined as the work required to create a unit of surface area. Alternatively, it can be viewed as a force per unit length resisting such an area increase (Hunter, 1986). The interfacial tension is, in general, lowered as surfactants accumulate at an interface. In terms of emulsion drop mechanics, this implies that drops will be more readily deformed in the presence of surfactants. For curved interfaces, such as those of emulsion drops, Young (1805) and Laplace (1805) described the equilibrium mechanical relationship between the liquid phases and the tension at the interface as

$$\Delta p = \gamma\left(\frac{1}{R_1}+\frac{1}{R_2}\right). \qquad (1.1)$$

In equation 1.1, Δp is the pressure difference across an arbitrary curved interface, γ is the interfacial tension and the term in brackets is the mean curvature, where R_1 and R_2 are the principal radii of curvature (Adamson, 1976). Note that a more familiar form of this equation is observed for spherical drops of radius R_d, in which the mean curvature is given by $2/R_d$. Assuming that the equilibrium interfacial tension is the only surface material property, deformability of emulsion drops may be quantified by the Young-Laplace equation (Walstra, 1993).

In addition to the interfacial tension, other surface properties may influence the mechanical behaviour of emulsion drops. Interfacial viscosities, which are intrinsic dissipative properties, were first noted by Plateau (1869) and further defined by Boussinesq (1913). Purely dissipative interfaces are described by a two-dimensional analogue to a Newtonian fluid (Scriven, 1960; Evans and Skalak, 1980). Elastic interfacial properties have also been considered in detail and descriptions of viscoelastic interfaces are available (Evans and Skalak, 1980; Edwards et al., 1991). The dissipative surface properties will affect the rate of drop deformation, while the elastic surface properties will affect the magnitude of such a process.

Almost all techniques used to study rheological properties of interfaces are performed at length scales of millimeters or larger (Edwards et al., 1991; Miller et al., 1996); these are orders of magnitude above the relevant length scales of emulsion drops. This has tremendous consequences when the specific area (surface area-to-volume ratio) of an emulsion is important, such as in the partitioning of surfactants. Recently, it has been discovered that surfactant-adsorbed interfaces exhibit different interfacial tension values depending on the length scale considered and, consequently, on the measurement technique utilized (Yeung et al., 1998). It is, therefore, reasonable to infer that other interfacial mechanical properties may vary based on the length scale considered. Since the mechanical behaviour of an emulsion drop depends on its surface rheology, it is imperative to study the mechanics of such a drop *in situ* at length scales appropriate to emulsion systems.

The mechanical behaviour of crude oil drops in water, often encountered in the oil sands industry, is of particular interest in this study. Oil sands represent a significant hydrocarbon resource and rivals that of conventional crude oil (Demaison, 1977; Ruhl, 1982; Czarnecki, 2001). With the continuing decline in conventional reserves, fuels acquired from oil sands will become increasingly important. Nearly half of the global oil sands reserves, approximately 1700 billion barrels, are located in northeastern Alberta, Canada (Czarnecki, 2001; Salager et al., 2001). Typically, Alberta (the Athabasca region) oil sands consist of ~10 wt% bitumen[3], a heavy crude oil, while the remainder is mainly inorganics such as silica sands and, to a lesser extent, fine clays (Shaw et al., 1996).

Before bitumen can be sent to the refineries, it must first be separated from the sand. This is accomplished using a water-based extraction process (Clark and Pasternack, 1932; Shaw et al., 1996; Czarnecki, 2001). In this process, a slurry composed of oil sands (obtained from an open pit mining operation), hot water[4] (~50-80°C) and caustic (sodium hydroxide) is agitated inside tumblers or pipelines. The caustic is required to release natural surfactants from within the bitumen, allowing for improved recovery. The mechanical agitation enables the liberation of bitumen drops from the sand particles and also serves to aerate the bitumen drops. This 'conditioned' slurry is transferred to a quiescent flotation vessel to allow the coarse sand particles to sink to the bottom of the vessel and the aerated bitumen drops to float to the top and form a bitumen-rich froth layer. Some of the liberated drops in the slurry approach an emulsion dimension (10-40 microns in diameter) and represent the difficult-to-recover bitumen fraction (Shaw et al., 1996). It is clear that the deformation and coalescence of these small, dispersed bitumen drops is a critical aspect to the extraction process (Lam et al., 1995).

The present research is aimed at studying the mechanics of emulsion drops *in situ*; that is, describing their mechanical behaviours within an emulsion system. As such, the objective is to develop novel mechanical techniques that allow for the manipulation of individual emulsion drops *in situ*. Particular focus will be given to the surface properties of these drops. The information gained will provide insights into the mechanical behaviour of emulsion drops and may have important consequences to emulsion technology, such as the rheological properties of emulsions or the processes of

---

[3] The United Nations Institute for Training and Research defines bitumen as a hydrocarbon with a viscosity greater than 10^4 mPa·s (at deposit temperature) and a density greater than 1000 kg/m^3 at 15.6 °C (Shaw et al., 1996).

[4] Recently, an economically advantageous low energy operation has been introduced which allows for water-based extraction at ~ 25°C (Mankowski et al., 1999; Czarnecki, 2001).

emulsification and drop coalescence. As a particular experimental system, the mechanical behaviour and properties of bitumen drops in aqueous environments, that are representative of industrial oil sands extraction operations, will be examined. The theme of this research is developed in the following paragraphs.

Chapter 2 details an emulsion-scale *microcantilever* technique that allows for *in situ* study of the static mechanical behaviour of single emulsion drops. This novel technique, along with an analysis based on the Young-Laplace equation, is used to evaluate the interfacial tension of dispersed drops involving simple liquids.

The microcantilever technique is ideally suited for density-matched systems in which at least one phase is highly viscous (e.g., bitumen-water systems). In chapter 3, the interfacial tension of bitumen-in-water emulsion drops is examined using the microcantilever technique. This is the first tensiometric technique to examine these systems; the study of such systems has not been possible with traditional methods.

Chapter 4 introduces a second technique for the *in situ* study of emulsion drops. This novel *drop shape recovery* technique involves observing the dynamic behaviour of a deformed emulsion drop. In addition to these experiments, a theoretical analysis is implemented to analyze systems in which the viscosity of one phase is vastly different from the other phase – systems for which traditional analyses experience difficulties.

In chapter 5, the drop shape recovery technique is used to evaluate some material properties of bitumen. The viscosity of bitumen, which is extremely high at room temperature, is quantified in a manner that completely circumvents the problem of viscous heating. This method can also be used to measure the interfacial tension of bitumen drops in alkaline environments, where the tension is expected to be very low (below the sensitivity of the microcantilever technique).

In chapter 6, the micropipette techniques are adapted to explore more complex rheological behaviours. In particular, the properties of bitumen drops in water containing calcium ions and montmorillonite clays, an environment expected to be detrimental to oil sands extraction processes, is examined.

Finally, the contributions of this research and suggestions for future work are summarized in chapter 7.

Chapter 2

Equilibrium Mechanics of Emulsion Drops: Microcantilever Technique

2.1 Equilibrium Mechanical Behaviour of Emulsion Drops

Mechanics studies the behaviour of a material in reaction to an applied stress and can involve both reversible (equilibrium) and irreversible responses. A mechanically reversible behaviour is characteristic of an elastic material in that the system returns to its original configuration following the removal of external stress. Irreversible behaviour is characterized by permanent plastic deformation resulting from dissipative flow of the material.

The equilibrium mechanical behaviour of emulsion drops is crucial to many applications. For example, in concentrated emulsions (disperse phase ≥ 70 vol%) common to the petroleum industry, stabilized drops may experience significant static deformation, which can affect the structure and properties of the entire emulsion (Nunez et al., 2000; Princen, 2001).

A *microcantilever* technique is developed to directly study the equilibrium mechanical behaviour of individual emulsion drops. This technique involves distorting (stretching) an otherwise spherical drop using two suction pipettes and quantifying the stretching force with a glass cantilever. For reversible systems, the experimental force-drop deformation relation is well described by the Young-Laplace equation, which is a statement of mechanical equilibrium between interfacial and externally applied forces. (This assumes that the interface is characterized by a uniform interfacial tension alone.) Because of this, the microcantilever technique can be used to evaluate interfacial tensions at emulsion drop surfaces. This method of "*in situ* tensiometry" is applied to emulsions composed of pure simple liquids (in the absence of surfactants) and the results are in good agreement with literature values.

Interfacial tension (IFT), defined as the work to create a unit of new surface between two immiscible fluids (Hunter, 1986), is perhaps the most important physical property of liquid-liquid interfaces. In emulsion studies, knowledge of the interfacial tension is crucial to understanding phenomena such as the adsorption of stabilizers, the drainage of thin films (a precursor to drop coalescence), and the formation of new emulsion drops (Tadros and Vincent, 1983a; Verhoeckx et al., 1987; Overbeek et al., 1987; Ruckenstein, 1988; Walstra, 1993). Clearly, in such situations, it is the tension at the surfaces of the dispersed drops that is of relevance. It has recently been demonstrated that, in the presence of surfactants, the interfacial tension of micron-sized emulsion drops may differ appreciably from IFT values quantified on the "lab" scale, i.e., involving sample sizes that are millimeters or larger. Such discrepancies are due to dissimilar partitionings of surfactants, which in turn result from the vastly different surface-to-volume ratios of the systems (Yeung et al., 1998). Thus, in order to delineate the effects of interfacial tension on emulsion properties, it is necessary to conduct tensiometric studies on length scales characteristic of the individual drops (i.e., on the micron scale). On a broader scope, such tensiometric studies will necessitate development of micromechanical techniques, which may find applications in other areas involving microvolumes – such as the study of food colloids or microcapsules used in drug delivery (Dalgleish, 1996; Pieper et al., 1998).

Numerous techniques of interfacial tension measurement have been developed in the past, some dating back more than a century and have withstood the scrutiny of time. Descriptions of the established methods, as well as their strengths and limitations, can be found in most colloids textbooks and review articles (Adamson, 1976; Tadros and Vincent, 1983b; Hunter, 1986). Common examples of such techniques are: the Wilhelmy plate and Du Noüy ring, which measure the force needed to traverse an object through an interface; the drop volume method, based on the balance of gravity forces against capillary effects; the spinning drop method, which studies drop distortion caused by centripetal acceleration; and the pendant and sessile drop methods that involve analysis of gravity-distorted drop shapes. It is noted that all of these methods require sample sizes of millimeters or larger and are incapable of dealing with individual emulsion drops.

Recently, a micropipette technique was developed to measure the interfacial tension of micron-sized water drops in non-polar media (Yeung et al., 1998). This technique, adapted from the field of biophysics (Evans, 1980; Evans and Needham, 1987), involves capturing individual emulsion drops at the tips of glass suction pipettes; the pipette diameter, typically of several microns, must be smaller than the drop size. From this configuration, the minimum pressure required to draw in the drop is a direct measure of the interfacial tension. Such a technique, despite merits for its simplicity, is applicable only to interfaces that do not wet or adhere to the pipette's inner wall (drops which adhere to the pipette require much higher pressures to be drawn in); this can be a serious limitation when dealing with emulsion drops that are, for example, adsorbed with macromolecules.

The microcantilever technique represents an alternative that circumvents such difficulties associated with the minimum pressure micropipette method. As noted above, in this new technique, an emulsion drop is elongated from its natural spherical shape using two suction pipettes and the required pulling force is measured. The resistance offered by the drop is due to an interfacial tension acting at its surface, which tends to restore the drop to a minimum area configuration (i.e., a sphere). By quantifying the force-drop deformation relation, the interfacial tension of an individual drop can be determined. Such an experiment involves no relative motion between the interface and the pipette wall and is therefore ideal for examining drops with "sticky" surfaces. In this study, a *microcantilever* is used as the "force transducer." Similar methods of force detection have been reported in recent literature, with applications to pulp and paper research (Yeung and Pelton, 1996) and thin liquid film studies (Aveyard et al., 1996).

2.2 Theoretical Background

2.2.1 Drop profile and mechanical equilibrium

In this section, the theoretical background for the microcantilever method is developed. Figure 2.1 illustrates the stretching of a drop. The drop, with a radius of R_d in free suspension, is elongated to a length L by two suction pipettes of radii r_1 and r_2.[5] The drop maintains a constant volume throughout its deformation (figures 2.1a and 2.1b).

---

[5] As will be discussed in the next section, one of these pipettes is shaped as a cantilever and is thus capable of quantifying stretching forces.

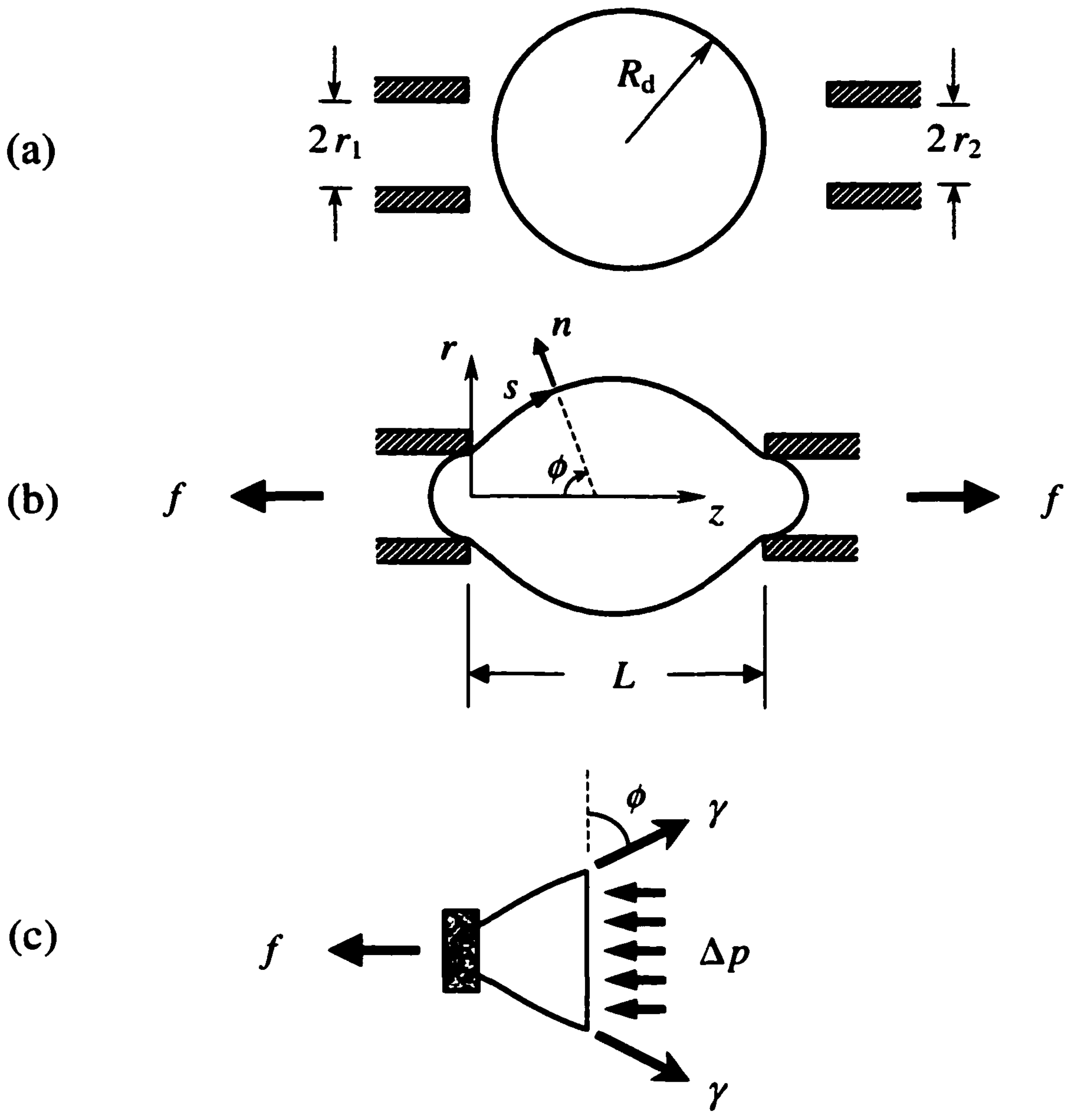

Figure 2.1. Depiction of an experiment conducted in this study; a spherical drop is stretched, at constant volume, using two suction pipettes (figures 2.1a and 2.1b). The two pipettes are aligned along a common axis, which also coincides with the axis of symmetry of the deformed drop. One of the *micropipettes* is shaped into a cantilever to allow for force measurements. The free body diagram of a drop segment is shown in figure 2.1c.

For drops that are microns in size, all gravitational body forces are inconsequential in comparison to capillary effects. This is made clear by evaluating the Bond number, which measures the ratio of gravitational to capillary forces. It is given by $B_o = \Delta\rho g R_d^{\,2} / \gamma$, where γ is the interfacial tension, g is gravitational acceleration, and $\Delta\rho$ denotes the density difference between the two fluids. Typical values in this study are R_d~10μm, γ~10mN/m, and $\Delta\rho$~100 kg/m^3. This leads to a Bond number of $B_o \sim 10^{-5}$. Without the influence of gravity, the elongated drop shape is determined solely by the balance of capillary forces against the applied stretching force. By aligning the two pipettes along a common z axis as shown in figure 2.1, it is clear that the deformed drop will be axisymmetric about the same axis. Such a shape can, in general, be characterized by cylindrical coordinates (r, z) as shown in figure 2.1b. The same geometry can alternatively be specified by (s,ϕ), where s is the curvilinear distance (here, measured from $z = 0$) and ϕ is the angle between the surface normal and the axis of symmetry. These two sets of coordinates are interrelated by

$$\cos\phi = \frac{\mathrm{d}r}{\mathrm{d}s}\,; \qquad \sin\phi = \frac{\mathrm{d}z}{\mathrm{d}s}\,, \tag{2.1}$$

with the understanding that r, z and ϕ are all functions of s. When describing drop shapes, it is also important to quantify the local curvatures of the interface. Here, the two principal radii of curvature are given by

$$\frac{1}{R_1} = \frac{\mathrm{d}\phi}{\mathrm{d}s}\,; \qquad \frac{1}{R_2} = \frac{\sin\phi}{r}\,, \tag{2.2}$$

where R_1 is the radius of curvature in the s direction, and R_2 is the radius of curvature in the circumferential direction. From equations 2.1 and 2.2, it is easy to show that the local mean curvature, defined as the sum of the principal curvatures, can be written as

$$\frac{1}{R_1} + \frac{1}{R_2} = \frac{1}{r}\frac{\mathrm{d}}{\mathrm{d}r}\left(r\sin\phi\right). \tag{2.3}$$

Now, consider the condition of mechanical equilibrium. The free body diagram of a segment of the drop is shown in figure 2.1c. As the pipette on the left (including the small drop protrusion inside it) behaves as a rigid body, it is depicted as a solid block subjected to an axial force *f*. The quantity Δp represents the pressure difference across the interface, with a positive value denoting higher interior pressure and vice versa. With γ being the interfacial tension, the balance of axial forces is

$$f = 2\pi r \sin\phi \cdot \gamma - \pi r^2 \Delta p. \tag{2.4}$$

It is clear that, at equilibrium, the resultant axial force *f* must be a constant at any cross section perpendicular to the z-axis. By requiring d*f* = 0 in equation 2.4, we have

$$\gamma \cdot \mathrm{d}(r \sin\phi) - \Delta p\, r \cdot \mathrm{d}r = 0.$$

Combining the above relation with equation 2.3, we arrive at the familiar Young-Laplace equation

$$\Delta p = \gamma\left(\frac{1}{R_1} + \frac{1}{R_2}\right). \tag{2.5}$$

This equation, not surprisingly, results from the balance of forces on a curved interface. Note that in the absence of hydrostatic gradients (i.e., at low Bond numbers), the pressure drop Δp across the interface is uniform over the drop surface. It follows from the Young-Laplace equation (equation 2.5) that the elongated drop shape is one of *constant* mean curvature given by the ratio $\Delta p / \gamma$.

2.2.2 *Evaluation of force-drop shape relation*

The shape of an elongated drop under an axial load *f* must now be evaluated. As in pendant drop analyses, a numerical approach is unavoidable. Here, the constant mean curvature profile is obtained by solving three simultaneous ordinary differential equations (ODE's). The first two ODE's are given in equation 2.1. They are rewritten here, along with initial conditions (at $s = 0$) in accordance with figure 2.1:

$$\frac{\mathrm{d}r(s)}{\mathrm{d}s} = \cos\phi \; ; \quad r(0) = r_1 \tag{2.6a}$$

$$\frac{\mathrm{d}z(s)}{\mathrm{d}s} = \sin\phi \; ; \quad z(0) = 0. \tag{2.6b}$$

The third ODE is derived from mechanical equilibrium. From equations 2.4 and 2.5, the constant mean curvature is given by

$$\frac{1}{R_1} + \frac{1}{R_2} = \frac{\Delta p}{\gamma} = \frac{2\sin\phi}{r} - \frac{f}{\pi r^2 \gamma}.$$

Combining with equation 2.2, the final ODE, representing the meridional drop curvature R_1^{-1}, takes the form

$$\frac{\mathrm{d}\phi(s)}{\mathrm{d}s} = \frac{\sin\phi}{r} - \frac{f}{\pi r^2 \gamma}; \quad \phi(0)=\phi_o. \tag{2.7}$$

An alternative thermodynamic derivation for equation 2.7 is given in Appendix A. For a prescribed value of axial force *f*, equations 2.6 and 2.7 are integrated simultaneously (e.g., with a fourth order Runge-Kutta routine) until the drop profile connects with the pipette on the right hand side, where $r = r_2$ (see figure 2.1b). The drop length L, which depends on the stretching force *f*, is given by the value of z at this end point. Such a procedure is, as yet, arbitrary as the initial angle ϕ_o in equation 2.7 is not specified. The value of ϕ_o must be determined from the constant volume constraint. The volume V of the elongated drop (also evaluated numerically) is matched to the volume of the undeformed drop, less the two protrusions inside the pipettes; that is

$$V = \frac{4}{3}\pi R_d^3 - \left(v_1 + v_2\right), \tag{2.8}$$

where v_1 and v_2 are the projected volumes in the pipettes (which, in many cases, can be approximated as hemispherical caps of radii r_1 and r_2). In practice, the initial angle ϕ_o is used as an iterative parameter to satisfy volume conservation (equation 2.8).[6] By non-dimensionalizing the above equations with the characteristic parameters R_d and γ, all variables will have magnitudes of order unity or less (a desirable condition for numerical

---

[6] As a digression, it is noted here that the angle ϕ_o bears no relation to wetting phenomena at the glass surface. The contact angle appearing in Young's equation (Hunter, 1986) is the angle between the interface and a line *tangent* to the solid surface at the perimeter of contact. As the glass surface also undergoes a discontinuity in angle (a 90° bend) at this location, the notion of a three-phase contact angle becomes ill-defined in theory and irrelevant in practice.

calculations). Thus, the axial force f is scaled by the product γR_d, while all geometric dimensions are expressed in terms of the initial drop radius R_d. The numerical procedures, as outlined above, compute the following functional dependence

$$\frac{f}{\gamma R_d} = \text{function of}\left(\frac{L-L_i}{R_d};\frac{r_1}{R_d};\frac{r_2}{R_d}\right), \tag{2.9}$$

where L_i is the drop length corresponding to $f = 0$ (i.e., when the exterior drop segment is spherical). Equation 2.9 is evaluated based on the conditions of mechanical equilibrium and volume conservation. In the process, a detailed profile of the elongated drop is also obtained from integration of equations 2.6 and 2.7. The numerical code used to calculate equilibrium axisymmetric drop shapes, based on the above analysis, is given in Appendix B.

2.3 Materials and Methods

2.3.1 Emulsion preparation

Although the microcantilever technique presently discussed is equally applicable to oil-in-water dispersions, only water-in-oil emulsions are studied in this chapter. Five non-polar solvents are chosen as the continuous oil phases; they are: ethyl acetate, chloroform, benzene, toluene and "heptol" (i.e., a 1:1 mixture, by volume, of n-heptane and toluene). These solvents, all purchased as HPLC grade products, are used with no further purification. Filtered and deionized distilled water is used as the aqueous (dispersed) phase. To make an emulsion, 100μL of water is introduced into 10mL of solvent (i.e., 1% water by volume). The mixture is agitated for 10 seconds in a water bath sonicator (Fisher Scientific, model no. FS6), creating an emulsion of water drops that are 5 to 50μm in diameter. Such an emulsion, composing only of pure fluids, is clearly unstable. However, in this study, the volume fraction of the dispersed phase is sufficiently low (1%) that individual emulsion drops are not likely to encounter each other in a quiescent environment. To avoid dissolution of water into the oil phase, each solvent is pre-saturated with water prior to emulsion preparation (e.g. by leaving a solvent/water mixture in a closed container overnight).

2.3.2 The micropipette experimental set-up

This is a technique of studying the mechanics of micron-sized objects with the use of small suction pipettes. Originally developed in the field of biophysics for studying blood cells and surfactant membranes (Evans, 1980; Evans and Needham, 1987), this technique has recently been adapted for applications in other areas of colloid science (Yeung and Pelton, 1996; Yeung et al., 1998). Basic aspects of the micropipette setup are shown in figure 2.2. Approximately 50μL of an emulsified solution is placed in a sample cell assembled from microscope cover slips. As shown, the emulsion is retained by capillary forces in a gap of width 1.2mm. Micron-sized drops in the emulsion can be observed with an inverted microscope that utilizes transmission bright-field illumination (Carl Zeiss Canada; Axiovert 100). To manipulate individual drops, two small suction pipettes are extended into the sample cell from opposite sides. The pipettes are mounted on micromanipulators (Narishige, Tokyo) to enable their continuous motions on the micrometer scale. A blow-up view of the sample cell and micropipettes is also shown in figure 2.2. A video system (CCD camera (model KP M3U, Hitachi Denshi, Japan), videocassette recorder (SLV-R1000, Sony) and TV monitor) is connected to the microscope for the monitoring, in real time, of micropipette experiments. These sequences are also recorded on tape for subsequent analyses.

The micropipettes are made from 1mm OD, 0.7mm ID glass capillary tubes (Kimble Glass Inc., batch no. 32829-020). Using a hot wire pipette puller (David Kopf Instruments, Tujunga, CA; model 730), the capillaries are stretched axially under high temperature, resulting in tapered hollow tubes whose end dimensions are on the sub-micron scale. Next, with the use of a home-made forging device, the tapered ends are truncated to produce pipette tips that have inside diameters ranging typically between 5 and 10 microns. In this application, as the pipettes are intended for the manipulation of water drops, the tips must be pre-treated with a methylating agent to prevent spreading of the drops onto the glass surfaces; the methylating chemical may, for example, be dichlorodimethylsilane (Aldrich Chemicals) applied at 20× dilution in cyclohexane. To capture individual drops, controllable suction pressures are applied at the pipette tip. This is accomplished by connecting the other end of the pipette (the large, untapered end) to a

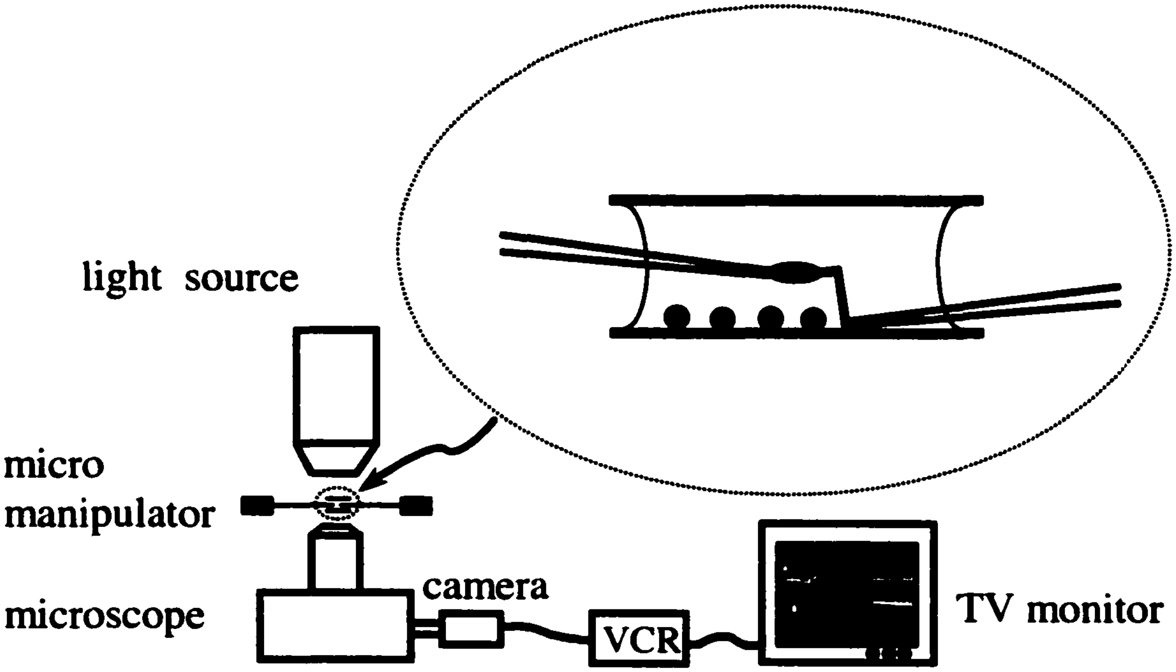

Figure 2.2. A schematic of the micropipette setup. Emulsion drops are placed in a small holding cell (also shown in the blow-up view) and can be individually manipulated by two suction pipettes. The pipette on the right is shaped as a cantilever to enable force measurements. A yet closer view of the cantilever pipette is shown in figure 2.3.

60mL syringe through flexible tubing. If required, this suction pressure is measured using commercial pressure transducers (e.g., Omega Engineering, Stamford, CT).

The straight micropipette, as described above, is suitable for capturing and translating individual emulsion drops, but is otherwise insensitive to the axial force it is subjected to. An additional force-measuring capability can be provided by creating two right-angle bends in a micropipette as shown in figure 2.3. Such a pipette will be called a "microcantilever." The bends are made by gently pushing local regions of a straight pipette against a heated platinum wire; the temperature of the wire is such that it will soften the glass material but does not cause melting. The first bend is made approximately 30 to 60 microns from the tip. The second bend, separated from the first by about 6mm, is turned in the opposite direction while maintaining an overall planar shape; the average pipette diameter between the first and second bend is approximately 25μm. The resulting structure remains a connected hollow tube and therefore continues to allow for the control of suction pressures at its tip. As in the case for straight pipettes, microcantilevers used in this study must be treated with a methylating agent to provide for hydrophobic surfaces.

Due to its unique shape, a microcantilever will deflect under a horizontal force applied at its tip. Here, the descriptions "horizontal," "up" and "down" are not in reference to the gravitational field, but are as indicated in figure 2.3. It is seen in figure 2.3 that the cantilever "elbow" is rested against a solid support (the wall of the sample cell). Without such support, horizontal deflections of the tip will be accompanied by downward displacements of the same order of magnitude, which can disrupt the coaxial alignment of an experiment. Knowing the Young's modulus of the pipette material (approximately 0.7×10^{11} Pa for borosilicate glass), and provided with detailed dimensions of the microcantilever, the elastic stiffness k_b in the horizontal direction can be calculated from beam theory (Crandall et al., 1972). The microcantilever stiffness is strongly dependent on its dimensions. By varying geometric features such as the length, diameter, and degree of tapering, k_b can be made to range from 1 to 10^5 mN/m. In this study, the beam stiffness k_b is normally between 20 to 60 mN/m. For capillary forces of order γR_d applied at the pipette tip, the maximum strain created within the

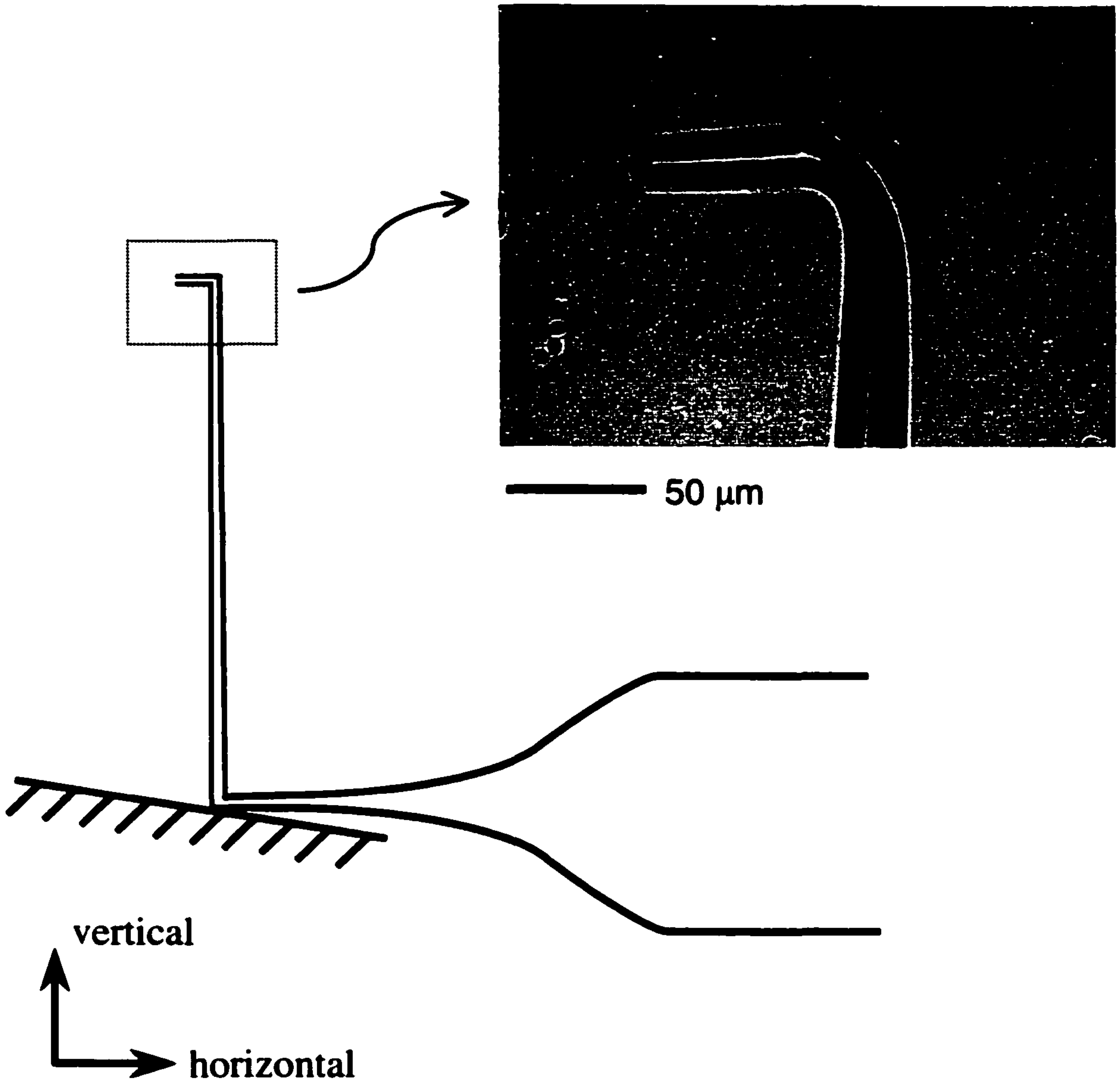

Figure 2.3. A sketch of the microcantilever; the blow-up view is an actual photograph. Shaped like a periscope, the cantilever is a continuous hollow tube with end diameters of 1mm on the untapered side and ~10μm at the tip. The vertical section is roughly 25μm in diameter and has a length of 5-6mm. The structure, supported as shown, has an effective stiffness of ~10mN/m.

microcantilever is estimated to be $\sim 10^{-5}$, which is well within the linear elastic regime for glass (cf. brittle failure at strain levels of several percent). It is therefore safe to assume that, for the present application, the deflection of a microcantilever is *directly proportional* to its axial load. Details of the cantilever stiffness calculations can be found in Appendix C.

2.3.3 Calibrating the microcantilever

Due to the extremely small strains involved, the deflection of a microcantilever is directly proportional to the applied axial load. A very good estimate of the proportionality constant k_b can be provided by linear elastic theories (see Appendix C); such an estimate is often accurate to within a few percent. For higher order corrections, the cantilever must be calibrated with known forces. This can be done by suspending a weight, such as a 300-500μm glass bead, at the tip of the cantilever and determining the resulting deflection. Because the weight of an object varies as the third power of its size, the resulting uncertainty in the "known" force is often larger than that of the calculated stiffness. In this study, we have chosen to use the capillary forces between simple fluids to provide for the axial load, i.e., the cantilever is calibrated by stretching a water drop in a hydrocarbon whose interfacial tension with water is well known. This approach apparently embodies a contradiction in reasoning; the same drop-stretching process that is used to calibrate the cantilever, assuming a known IFT, is also used for measuring interfacial tensions, assuming the cantilever stiffness is accurately known. In practice, such a dilemma is circumvented by a *self-consistent* approach: Before measuring the IFT of an "unknown" system (e.g., between water and toluene), the microcantilever is first used to verify at least three documented IFT values (e.g., between water and heptane, chloroform and benzene) based on a calculated beam stiffness. A *consistent* discrepancy between the measured IFT's and the literature values, typically of a few percent, suggests a correction factor for the cantilever stiffness. The corrected k_b value is then used to determine the IFT between the fluids with unknown tensions.

2.3.4 Drop deformation experiment

The drop deformation experiment, as illustrated in figure 2.1, is conducted with a straight pipette on the left and a microcantilever on the right. To begin, the dimensions of the pipette tips and the emulsion drop (i.e., r_1, r_2, and R_d in figure 2.1a) are obtained from video images. Calibration for length measurements is performed by recording the image of a stage micrometer under the same magnification. Before proceeding with drop deformation, the tip position of a stress-free microcantilever is noted; this coordinate will be needed in evaluating cantilever deflections caused by axial loads. Next, suction pressures are applied at the pipette tips to firmly grasp an emulsion drop at opposite ends. By retracting the straight pipette while keeping the thick end of the microcantilever stationary, both the drop and the cantilever tip are pulled to the left. A sequence of photographs depicting such a process is shown in figure 2.4, where a water drop is being stretched in chloroform. Note the deflection of the flexible cantilever on the right, as indicated by its tip positions relative to the vertical reference line. The elongation of the drop is also evident from these photographs. The two quantities which define the force-drop deformation relation can now be determined: the drop length L (as shown by the arrows in figure 2.4) is obtained directly from image analysis, while the axial force f is given by the product of the cantilever deflection and the beam stiffness k_b. For each emulsion drop, approximately ten measurements of (f, L) are made at different stages of the drop stretching process. Image analysis is performed with the software Sigmascan Pro (Jandel Scientific, version 4). The spatial resolution, estimated to be two pixels in the digitized images, corresponds roughly to 0.2μm.

The interfacial tension is obtained from the force-drop deformation data as follows: It is seen from equation 2.9 that, given the geometric dimensions r_1, r_2, and R_d (and hence the ratios r_1/R_d and r_2/R_d), the dependence of $f/(\gamma R_d)$ on $(L-L_i)/R_d$ can be calculated from the procedures outlined above. The two experimental unknowns in these dimensionless groups are the interfacial tension γ and the reference drop length L_i.[7]

---

[7] Although measurable in principle, L_i (the length corresponding to zero axial force) is difficult to quantify experimentally due to problems such as image diffraction at the pipette tip.

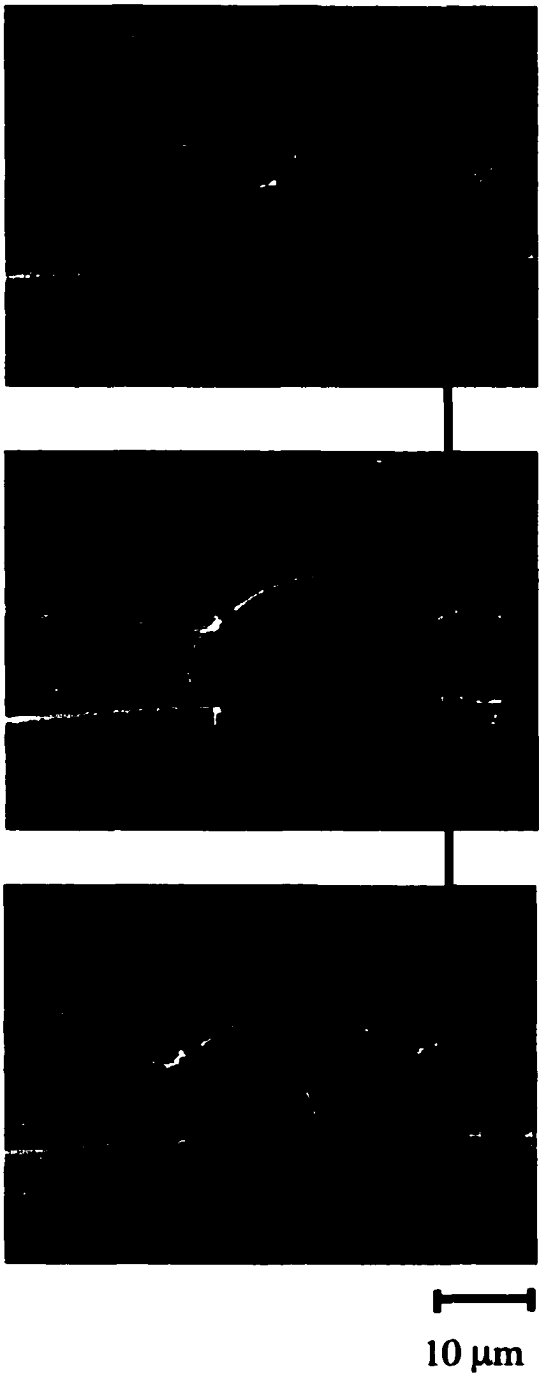

Figure 2.4. Photographs of an actual drop stretching experiment. In this case, a water drop is being elongated while submerged in chloroform. The pipette on the right is a flexible cantilever (cf. figure 2.3). From the deflection of the cantilever, as evidenced by its tip positions relative to the solid vertical line, the stretching force can be determined. The length of the stretched drop is also obtained from these images (shown by the arrows).

By allowing γ and L_i to be adjustable parameters, their values can be determined from a least squares fit of the (f, L) data to the theoretical $f/(\gamma R_d)$ vs. $(L-L_i)/R_d$ relation using, for example, Gauss-Newton regression techniques. In the end, the value of γ which optimizes the fitting criteria will serve as a measure of the interfacial tension between the two fluids.

2.4 Results and Discussion

The microcantilever technique is applied to emulsions composed of simple liquids to study the static mechanical behaviour of their emulsion drops, which is primarily described by the interfacial tension at the drop surface. In the absence of surfactants, the interfacial tension between two pure immiscible fluids must exhibit the same value – whether it is quantified at the surface of an emulsion drop or by other tensiometric methods (this is not necessarily true when surfactants are present; see Yeung et al., 1998). Thus, with agreement established between microcantilever data and literature IFT values in these simpler cases, meaningful results can be assured when the new technique is extended to more complex emulsion systems.

The method of determining the pulling force f and the drop length L was outlined in the previous section and also illustrated in figure 2.4. Experimental data thus obtained for several water-in-oil systems are plotted in figure 2.5 in dimensional form. In figure 2.5, the continuous oil phases are: toluene, benzene and ethyl acetate – with interfacial tensions against water being 36.1, 34.1 and 6.8mN/m, respectively (Donahue and Bartell, 1952). The radii of the water drops are close to 10μm in all three cases. It should be noted that a reference length L_i is subtracted from L before it is plotted on the horizontal axis; this is to facilitate comparison of the three force-deformation relations. Two observations are made from these plots:

1. Oil-water mixtures with very similar IFT's (e.g., 36.1mN/m for toluene-water versus 34.1mN/m for benzene-water) are almost indistinguishable from the initial slopes of figure 2.5. Their differences, however, become more apparent as the drop extensions increase to values comparable to the initial drop radius (here, to roughly 10μm).

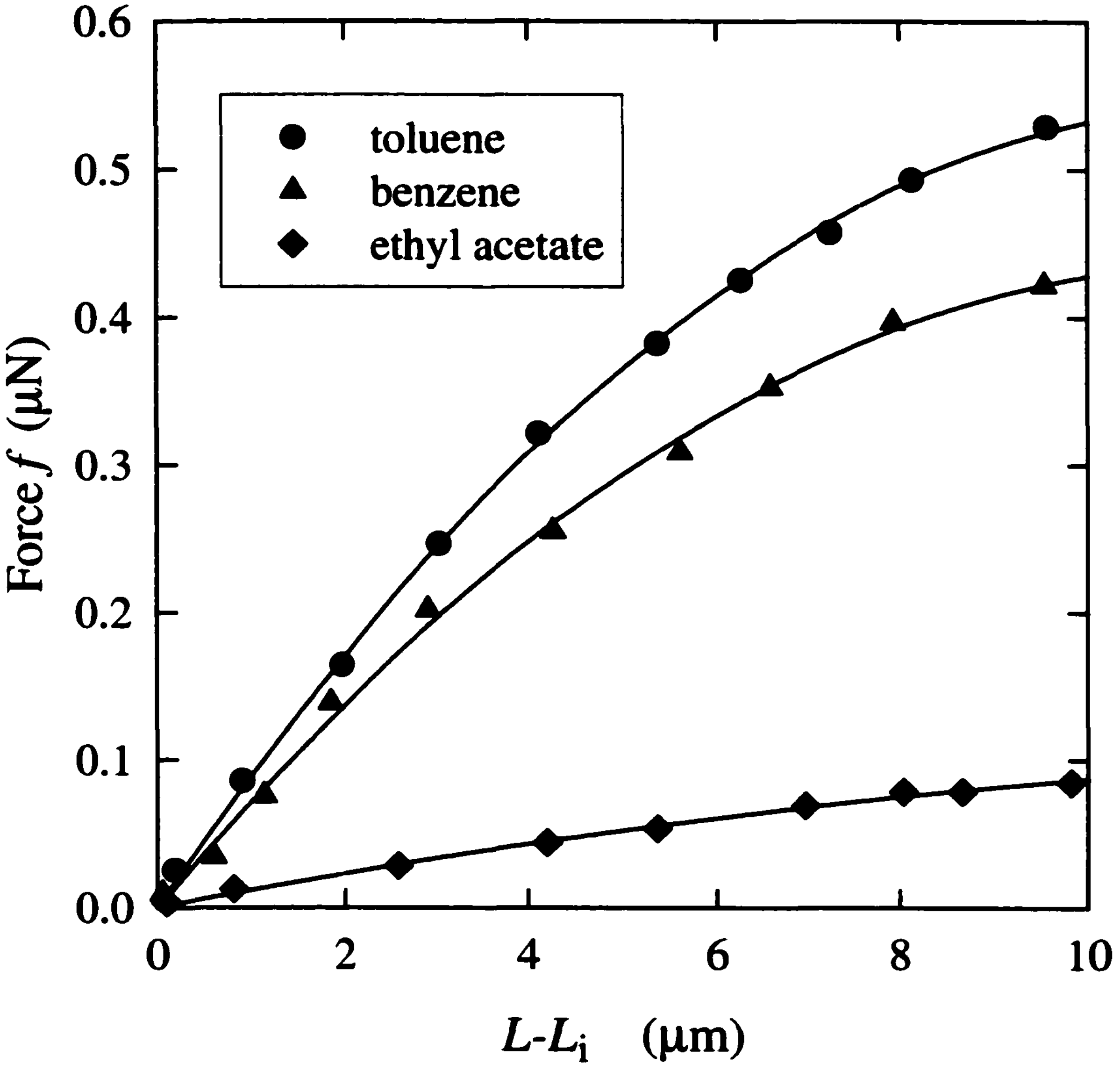

Figure 2.5. Experimental measurements of the stretching force f versus the drop deformation $L - L_i$. The three cases involved water drops dispersed in toluene, benzene and ethyl acetate, with corresponding interfacial tensions of 36.1, 34.1 and 6.8 mN/m, respectively. The lines are quadratic regressions through the data points. Note that 1μN is roughly the weight of 0.1 milligram.

2. The initial slopes of the curves in figure 2.5, which represent the effective "spring stiffness'" of the stretched drops, appear to be consistently 2-3 times the corresponding interfacial tensions.

The first observation concerns the sensitivity of the microcantilever technique. It is demonstrated in figure 2.5 that IFT's differing by about 1mN/m can be easily resolved. For this, it is necessary to subject the emulsion drop to larger extensions, of up to one R_d, at which point non-linear characteristics of the force-deformation relation become significant. The second observation was first noted by Evans et al. (1991, 1995) in their studies of biological cells. They showed that, for pressurized cells undergoing small extensions (relative to its initial size), the *apparent* spring constant is roughly given by

$$\frac{df}{dL} \approx \frac{2\pi\gamma}{\ln(R_d/r_1) + \ln(R_d/r_2)} \tag{2.10}$$

where γ is the interfacial tension. The above relation is very instructive: It shows how two of the dimensionless parameters in equation 2.9, namely, r_1/R_d and r_2/R_d, have only a weak (logarithmic) influence on the force-drop deformation relation. This implies, in practice, uncertainties in estimating pipette dimensions (e.g. problems associated with optical diffraction and aberrations) will not seriously affect measurements of interfacial tensions. Despite its usefulness in exposing functional dependencies, equation 2.10 remains a first order approximation and is therefore not suitable for studies requiring higher precisions. A more accurate model of the force-drop deformation relation, one that also accounts for the non-linear features at large extensions, can be obtained through the numerical procedures described in this chapter.

As an example, the least squares fit of a theoretical force-deformation relation to the (f, L) data is illustrated in figure 2.6, with the interfacial tension γ being the end product of such an analysis. Here, the experimental data are taken from the process depicted in figure 2.4.

Table 2.1 summarizes the interfacial tension values quantified by the microcantilever technique, together with corresponding literature values obtained from Donahue and Bartell (1952) and Yeung and coworkers (1998). The microcantilever

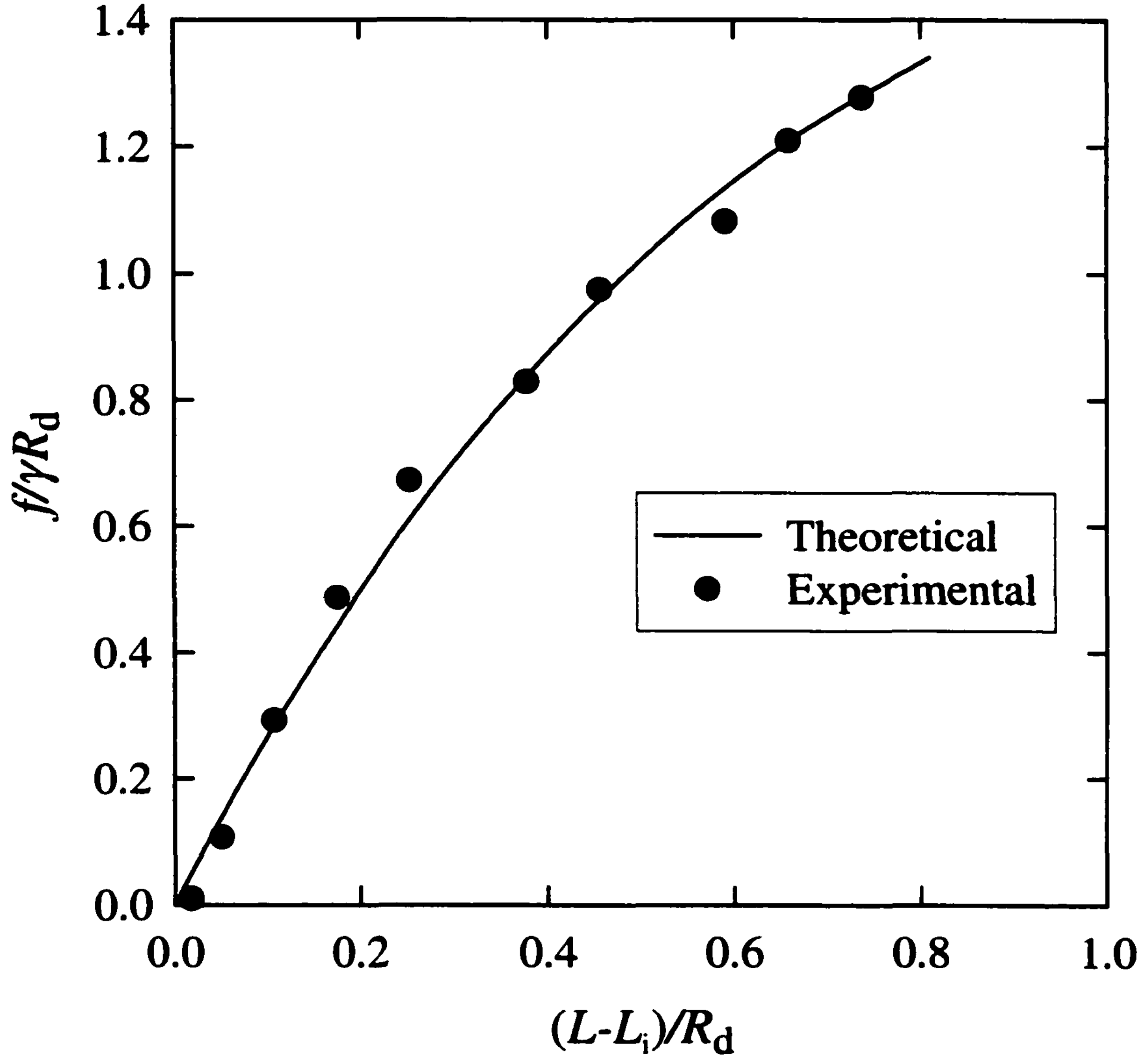

Figure 2.6. Fitting experimental force-deformation data to the theoretical predictions based on the Young-Laplace equation. The measurements are taken from the process in figure 2.4, where a water drop is stretched in chloroform. Adjustable parameters in the fitting procedure are the interfacial tension γ and the reference length L_i ; the latter corresponds to zero axial force.

technique is applied to five water-in-hydrocarbon emulsion systems. The hydrocarbons are: ethyl acetate, chloroform, benzene, toluene and heptol. For each system, 20 to 40 individual drops are studied, with a minimum of ten (f, L) data points taken for each drop. The quoted errors are standard deviations based on the 20 to 40 drops tested.

Table 2.1. Interfacial tensions of solvent-water systems. All measurements are done at room temperature.

Continuous phase	*Experimental Interfacial Tension (mN/m)*	*Literature Value (mN/m)*
Ethyl acetate	6.78 ± 0.58	6.8
Chloroform	30.9 ± 1.6	31.6
Benzene	33.7 ± 0.7	34.1
Toluene	36.4 ± 0.8	36.1
Heptol	40.3 ± 1.1	39.6

As seen from Table 2.1, agreement between measured and literature values is very good. These results document the applicability of the microcantilever technique in quantifying IFT's ranging from 6 to 40 mN/m (from ethyl acetate to heptol), with a resolution of ±1 mN/m or better (i.e., the ability to distinguish between toluene and benzene).

The calculated drop shapes, shown in figure 2.7, also appear to be in excellent agreement with the microscope images (cf. figure 2.4).

2.5 Conclusions

A microcantilever technique has been developed to quantify the static mechanical behaviour of individual emulsion drops. It involves stretching a drop using micropipettes and measuring the force-drop deformation relation. By fitting the experimental data to theoretical predictions based on the Young-Laplace equation, an accurate measure of the interfacial tension at emulsion drop surfaces is obtained. The method has been applied successfully to the measurement of interfacial tensions ranging from 6 to 40 mN/m. Such a technique has also opened the possibility of directly examining transport processes and rheological properties at the surfaces of emulsion drops and other similarly-sized microvolumes, such as food colloids or the microcapsules employed in drug delivery. This is an advantage not shared by any current method of interfacial rheometry.

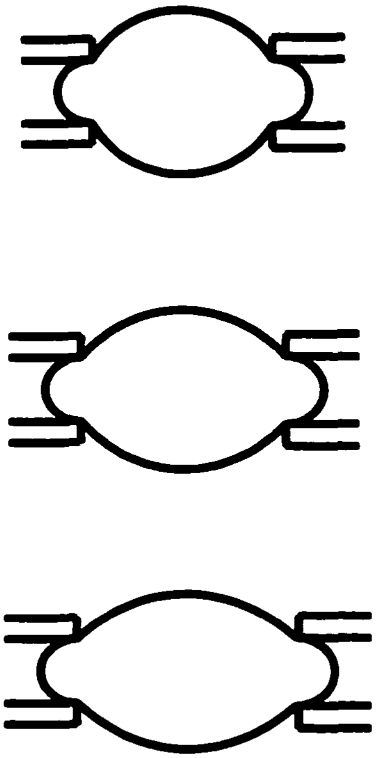

Figure 2.7. Theoretical drop shapes which simulate the three stages in figure 2.4. The shapes are calculated based on the measured axial forces, which are in turn determined from cantilever deflections.

Chapter 3

Interfacial Tension of Bitumen-in-Water Emulsions: An Application of the Microcantilever Method

3.1 Introduction

Measuring the interfacial tension (IFT) between density-matched fluids has been a serious challenge in the study of tensiometry. These measurements can be further complicated when one or both of the fluids possess high viscosities. The microcantilever technique (chapter 2) circumvents such difficulties. It is shown that, for mechanical experiments conducted on the 1-10μm scale, as in the present application, gravitational body forces and viscous effects can be neglected (provided relaxation times of several seconds are allowed). The system of present interest is that of Athabasca bitumen[8] drops in water at room temperature, in which the densities of the two phases are nearly equal (to within 1%), and the viscosity of bitumen is extremely high (more than 10^5 times that of water). This is the first study of bitumen-water interfacial tensions at room temperature over a range of pH and salt concentrations.

Tensiometric techniques predicated on density differentials (e.g., pendant drop, spinning drop, drop volume) become ineffective for systems of nearly matched densities. For such methods to be useful, heavy water ($\rho \sim 1100$ kg/m^3) has to be substituted as the aqueous phase (Isaacs and Smolek, 1983). At first glance, force-based techniques such as the Wilhelmy plate (Drelich and Miller, 1994) seem immune to vanishing density differences. Disregarding for the moment the common drawback of requiring zero contact angles, such techniques also assume, implicitly, that the extent of the meniscus is much smaller than the dimensions of the measuring plate. As the characteristic size of the meniscus, given by the capillary constant, diverges as $\Delta\rho^{-1/2}$, Wilhelmy plate-type techniques are, in general, inappropriate for systems with vanishing density differentials. The only means of IFT measurement that is truly unaffected by small $\Delta\rho$ appears to be the maximum bubble pressure method (Pandit et al., 1995). However, this technique is

---

[8] Athabasca bitumen is a heavy crude oil found in the oil sands deposits in northern Alberta, Canada. Refer to chapter 1 for further details.

limited to low viscosities systems and often must be operated at elevated temperatures to avoid molasses-like flow properties exhibited by fluids such as polymer melts and bitumen.

The measurement of bitumen-water IFT's has been, to date, a somewhat awkward process due primarily to the small density difference $\Delta\rho$ between the two phases. Over a temperature range of industrial significance (25-80 °C), the densities of water and bitumen differ by at most 10 kg/m^3, or by less than 1% (Liu, 1989; Pandit et al., 1995; Basu et al., 1996). As the oil sands industry is striving to operate at progressively lower temperatures (Mankowski et al., 1999), where the viscosity of bitumen is extremely high[9], techniques which allow for the study of bitumen-water IFT at these temperatures (~ 25 °C) are essential. In the previous chapter, a novel method has been developed to measure the IFT of micron-sized emulsion drops dispersed in an immiscible phase (Moran et al., 1999). As will be discussed below, this novel micron-scale technique avoids all difficulties typically encountered in IFT measurements of bitumen-water systems (i.e., vanishing density difference, high viscosity) and provides an *in situ* means of examining the surface properties of the bitumen drops.

The bitumen-water IFT is a decidedly important surface property to the coalescence of bitumen drops and, as a consequence, to the overall recovery of bitumen from oil sands (Shaw et al., 1996). It has been noted that the bitumen-water interfacial tension is reduced (Takamura and Isaacs, 1989; Drelich et al., 1995; Drelich and Miller, 1994), and bitumen recovery improves (Sanford and Seyer, 1979; Takamura, 1985), as the solution pH increases. In addition, the salt concentration of the aqueous phase may significantly affect bitumen-water IFT (Takamura and Isaacs, 1989). This chapter examines the IFT of bitumen-in-water emulsion drops over a range of pH values and salt concentrations and, in the process, demonstrates the unique applicability of the microcantilever technique to highly viscous, density-matched systems. It should be emphasized here that, although the discussion is centered mainly on bitumen, it is equally valid for interfacial tension measurements for highly viscous liquid systems with vanishing density differences (e.g., polymer melts in immiscible media).

---

[9] At room temperature, viscosity of bitumen is on the order of 10^5 times greater than conventional crude oil (Ruhl, 1982; Seyer and Gyte, 1989).

3.2 Preliminary Considerations

The interfacial tension of a bitumen drop is determined from conditions of mechanical equilibrium as it is distorted on the micron-scale (chapter 2). Before proceeding with the analysis, it is first shown that the two additional contributions to mechanical equilibrium, namely, forces due to gravitational and viscous effects, are inconsequential. The insignificance of gravity can be established by showing the Bond number, which is a measure of the ratio of gravitational to capillary forces, is much less than unity. The Bond number is given by $B_o = \Delta\rho g R_d^2 / \gamma$, where γ is the interfacial tension, g is gravitational acceleration, R_d is the spherical drop radius, and $\Delta\rho$ denotes the density difference between the two fluids. Typical values in this study are $R_d \sim 10\mu\text{m}$, $\gamma \sim 10\text{mN/m}$, and $\Delta\rho \sim 10$ kg/m^3, giving rise to a Bond number of $B_o \sim 10^{-6}$. Without the influence of gravity, and with the two pipettes aligned along a common axis (as shown in figure 2.1), it is clear that the deformed drop will be rotationally symmetric about the same axis. With regard to viscous effects, the ratio of viscous to capillary forces is expressed by the Weber number $W = \mu G R_d / \gamma$, where G is the rate of drop extension ($\sim \mathrm{d}\ln L / \mathrm{d}t$) and μ, the viscosity of bitumen, is typically 10^5 - 10^6 mPa·s at room temperature (note that 1 mPa·s is roughly the viscosity of water). For the viscous forces to be appreciable, i.e., for $W \sim 1$, the axial extension rate G must be of order 1s^{-1}. In practice, viscous effects are easily avoided by allowing deformed bitumen drops to equilibrate for sufficiently long times (typically for 3-4 seconds).

3.3 Materials and Methods

3.3.1 Emulsion preparation

Bitumen-in-water emulsions are prepared by introducing approximately one milliliter of "coker-feed" bitumen (Syncrude Canada Ltd.) into 20 mL of an aqueous solution. This mixture is then placed in a sonicator bath (Fisher Scientific, model no. FS6) at 80°C for one to two minutes. Bitumen drops in the resulting emulsions range between 5 and 30 μm in diameter.

In this study, the aqueous phases of most of the bitumen emulsions are designed to simulate the chemistry of process water in commercial oil sands extraction. This simulated process water (SPW) is composed of several salts (Fisher Scientific): NaCl (25 mM), $NaHCO_3$ (15 mM), and Na_2SO_4 (2 mM). In some experiments, $CaCl_2$ (0.3 mM) and $MgCl_2$ (0.3 mM), both obtained from Fisher Scientific, are added to the simulated process water to reflect the divalent cationic environments observed in some process waters (Shaw et al., 1996). This solution is referred to as "DSPW". Furthermore, to evaluate the effect of salts on bitumen-water interfacial tension, aqueous solutions of NaCl are prepared in concentrations ranging from 0 to 700 mM. The water used in all experiments is filtered and deionized.

The pH of the aqueous phase is controlled with drop-wise addition of HCl or NaOH (both from Fisher Scientific) and measured using a digital pH probe (Orion Research, model 701A). The amounts of acid/base required to achieve the desired pH have virtually no effect on the ionic strength of the final aqueous phase.

3.3.2 Bitumen-water IFT measurement: The microcantilever technique

The microcantilever technique provides a means by which applied forces on micron-sized emulsion drops may be quantified through the use of suction pipettes. In this technique an emulsion drop is captured between two suction micropipettes and elongated from its spherical shape. The resisting force offered by the drop as it is distorted is due to the IFT acting at its surface. This force is measured using a special microcantilever. By quantifying the force-drop deformation relation, the IFT can be determined. Details of this technique are provided in chapter 2 and elsewhere (Moran et al., 1999; Moran et al., 2000). Although theoretical calculations are used to determine the stiffness k_b of the cantilever (Appendix C), to allow for sufficient accuracy in IFT determination, the stiffness must be calibrated using known loads. In this study, the capillary forces of a simple fluid system, chloroform-in-water, are utilized to provide for the axial load (i.e., the cantilever is calibrated by stretching a chloroform drop whose interfacial tension with water is known). A consistent discrepancy between the measured IFT's and the literature value (Donahue and Bartell, 1952), typically of a few percent, provides a correction factor for the cantilever stiffness. The corrected k_b value is then used to determine the IFT between the bitumen drop and the aqueous phase.

A bitumen drop deformation experiment is depicted in a series of photographs (figure 3.1a), in which the micropipette is on the left and the microcantilever on the right. From figure 3.1a, it is seen that as the axial force is increased through the retraction of the micropipette (the one on the left), both the bitumen drop and the cantilever pipette are progressively deformed. The bitumen drop undergoes obvious elongations while the cantilever is increasingly deflected (as evidenced by its tip positions relative to the reference vertical line). The force-drop deformation relationship can now be quantified by measuring two experimental parameters – the applied force f and the corresponding axial drop length L. For each applied axial load, an equilibration time of a few seconds is allowed for the highly viscous bitumen drop to attain its equilibrium configuration. The equilibration time is given by $t \sim \mu R_d/\gamma$. This suggests a relaxation process driven by the interfacial tension γ and rate-limited by the viscosity μ of the drop. In this study, it is assumed that $\mu = 10^3$ Pa·s (Seyer and Gyte, 1989), $R_d \sim 10^{-5}$ m, and $\gamma \sim 10^{-2}$ N/m, resulting in a time constant of $t \sim 1$ second. To allow for equilibrium drop shapes, it is necessary to maintain a constant axial load for several time constants.

3.4 Results and Discussion

Before any results are discussed, an interesting wetting characteristic of bitumen is noted. In the present work, it is found that bitumen-glass interaction is strongly affected by the pH of the surrounding aqueous medium: At high pH values, bitumen does not exhibit any spreading on the glass surfaces (figure 3.2a). However, as the pH is lowered, there is a greater tendency for bitumen to spread on the micropipettes (figure 3.2b). This difference in wetting clearly indicates that the surface properties of bitumen are strongly influenced by the pH of the surrounding water. It also points to another advantage of the microcantilever technique; wetting characteristics of the drop have no bearing on the determination of IFT through drop stretching experiments.

Experimental $f - L$ data is presented in figure 3.3 over a wide range of pH values. The applied load f is calculated as the product of the microcantilever stiffness and the cantilever deflection. Note that the drop deformation is expressed as $L - L_i$ on the abscissa to allow for simultaneous comparison of several experiments. As the pH increases, less force is required to achieve the same axial deformation of a bitumen drop.

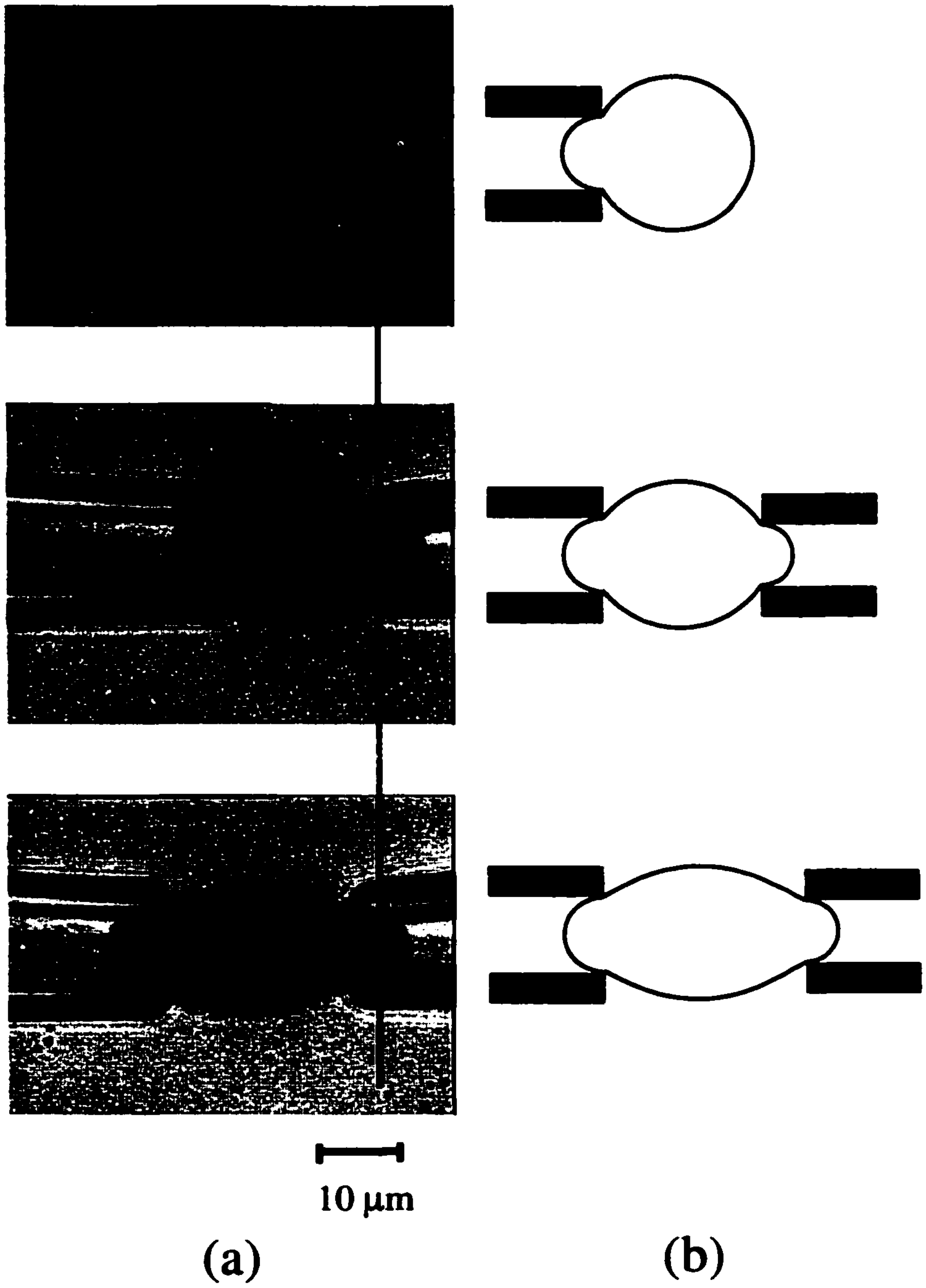

Figure 3.1. Photographs of bitumen drops being elongated in simulated process water. (a) At pH = 9.1: Axial forces can be determined from the deflections of the microcantilever (suction pipette on the right), as indicated by the tip positions relative to the reference vertical line. (b) Theoretical drop shapes, calculated based on experimental conditions in (a), show excellent agreement with video images.

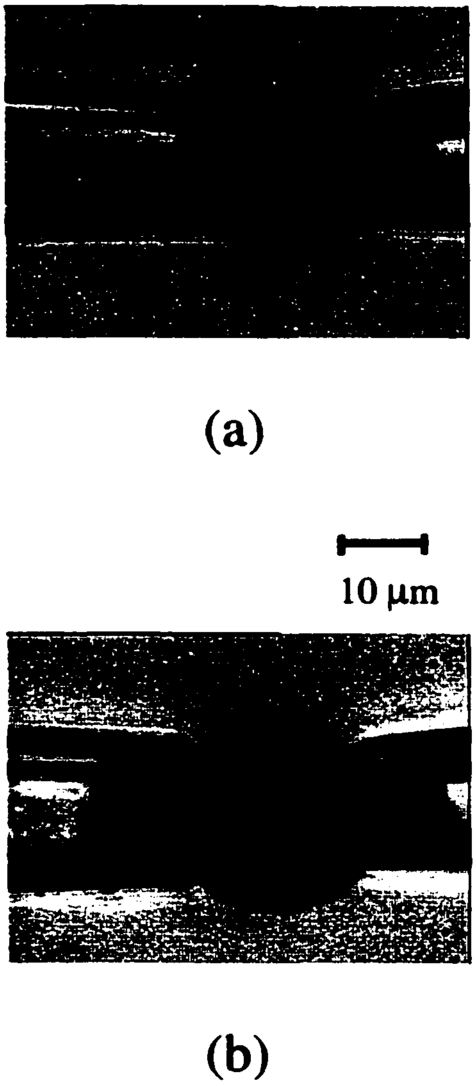

Figure 3.2. Photographs depicting the pH-dependent nature of the wetting properties of bitumen drops. (a) At pH = 9.1: The bitumen does not wet the glass surfaces. (b) At pH = 4.1: Note the spreading of bitumen at the tips and within the hollow cores of the pipettes.

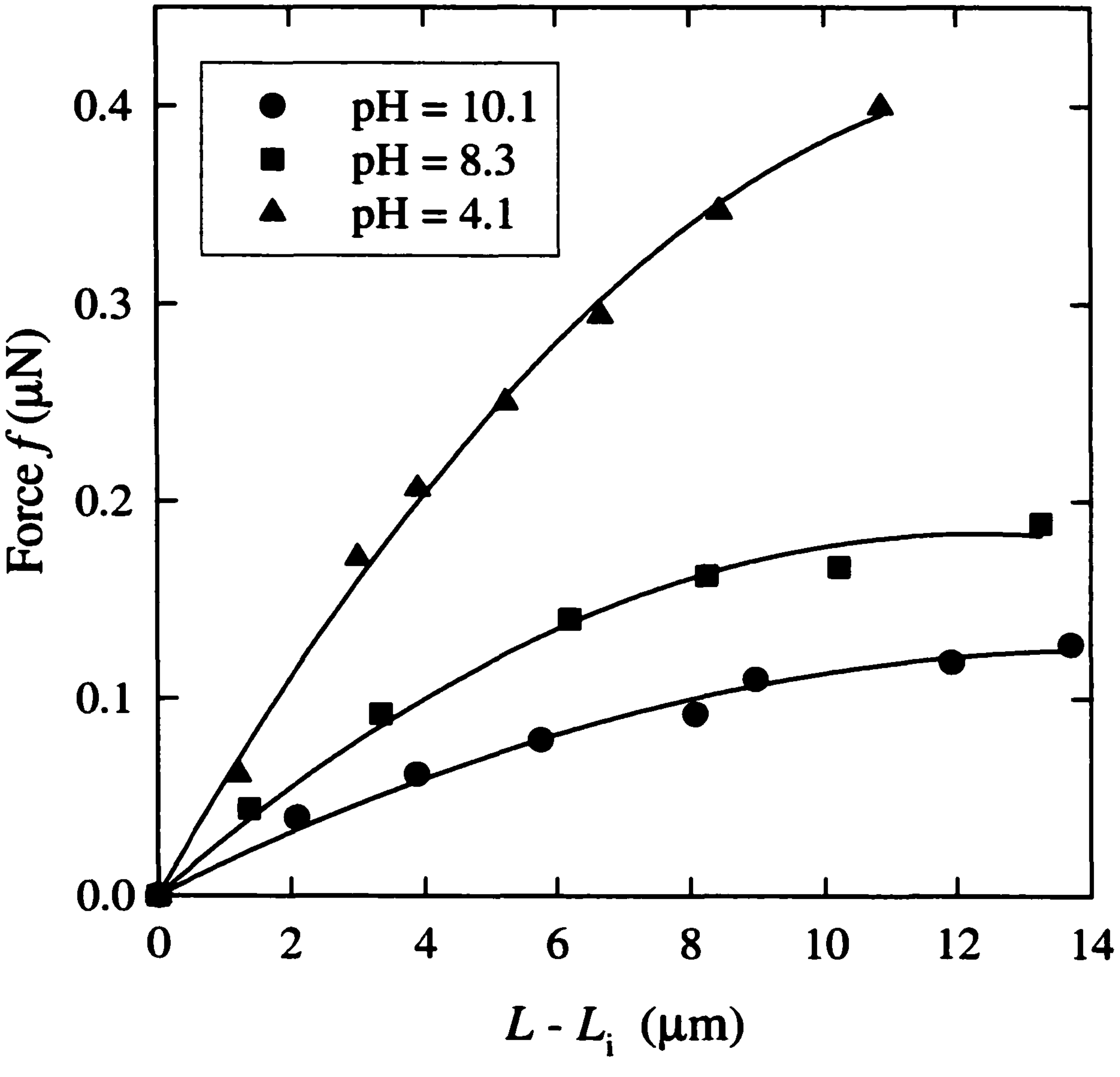

Figure 3.3. Measurements of the applied force f and the drop deflection $L - L_i$ at different pH's. The drop radii are approximately 12μm in all cases. Quadratic regressions have been fitted through the data points for clarity of presentation. Note that a μN is approximately the weight of 0.1 milligram.

Here, the microcantilever technique clearly reveals the influence of pH on the mechanical properties of the drop surface. This dependence may be effectively monitored by the interfacial tension.

The IFT's of micron-sized bitumen drops are determined by fitting experimental $f - L$ data to a theoretical model based on the Young-Laplace equation. Figure 3.4 gives an example of such a fit (cf. equation 2.9) for the experimental system shown in figure 3.1a. The theoretical analysis, discussed in chapter 2, also provides for a detailed solution of the drop shape at a given axial load. Excellent agreement is obtained between the experimentally observed and the theoretically predicted drop shapes (figure 3.1b).

It was shown in figure 3.3 that the pH of the aqueous phase strongly influences the $f - L$ relation of bitumen-in-water emulsion drops. It follows that the bitumen-water IFT will also be highly dependent on the pH. Figure 3.5 is a summary of such IFT measurements in simulated process water (SPW) and SPW doped with divalent cations (DSPW) over a pH range of 2 to 11. The IFT exhibits a maximum in the region of pH = 4, and is reduced as the pH increases to a value of 11. The IFT of the bitumen drops shows little variation at low pH values (between 2 and 6). For each pH value, a minimum of 10 individual drops are studied, with a minimum of six (f, L) data points for each drop. The error bars are standard deviations based on the number of drops examined. Above a pH value of 11, the IFT of the bitumen-water system is below the detection limit based on the present technique[10].

In the alkaline regime (pH >8), trends similar to figure 3.5 have been reported for Athabasca (Isaacs and Smolek, 1983; Takamura and Isaacs, 1989; Basu et al., 1996) and Utah (Drelich et al., 1995; Drelich and Miller, 1994) bitumens, as well as other crude oils worldwide (Cairns et al., 1976). The significant reduction in bitumen-water IFT at high pH has been attributed to the presence of species containing carboxylate functional groups (Drelich and Miller, 1994; Schramm et al., 1984). As the pH increases, these groups are liberated from precursors in the bitumen such that they act as surfactants and account for the observed reduction in IFT (Shaw et al., 1996; Schramm et al., 1984; Schramm and Smith, 1985; Schramm and Smith, 1989).

---

[10] The sensitivity of the microcantilever technique is, at present, on the order of 1 mN/m. Thus, the IFT of the bitumen drops at pH above 11 is less than 1 mN/m.

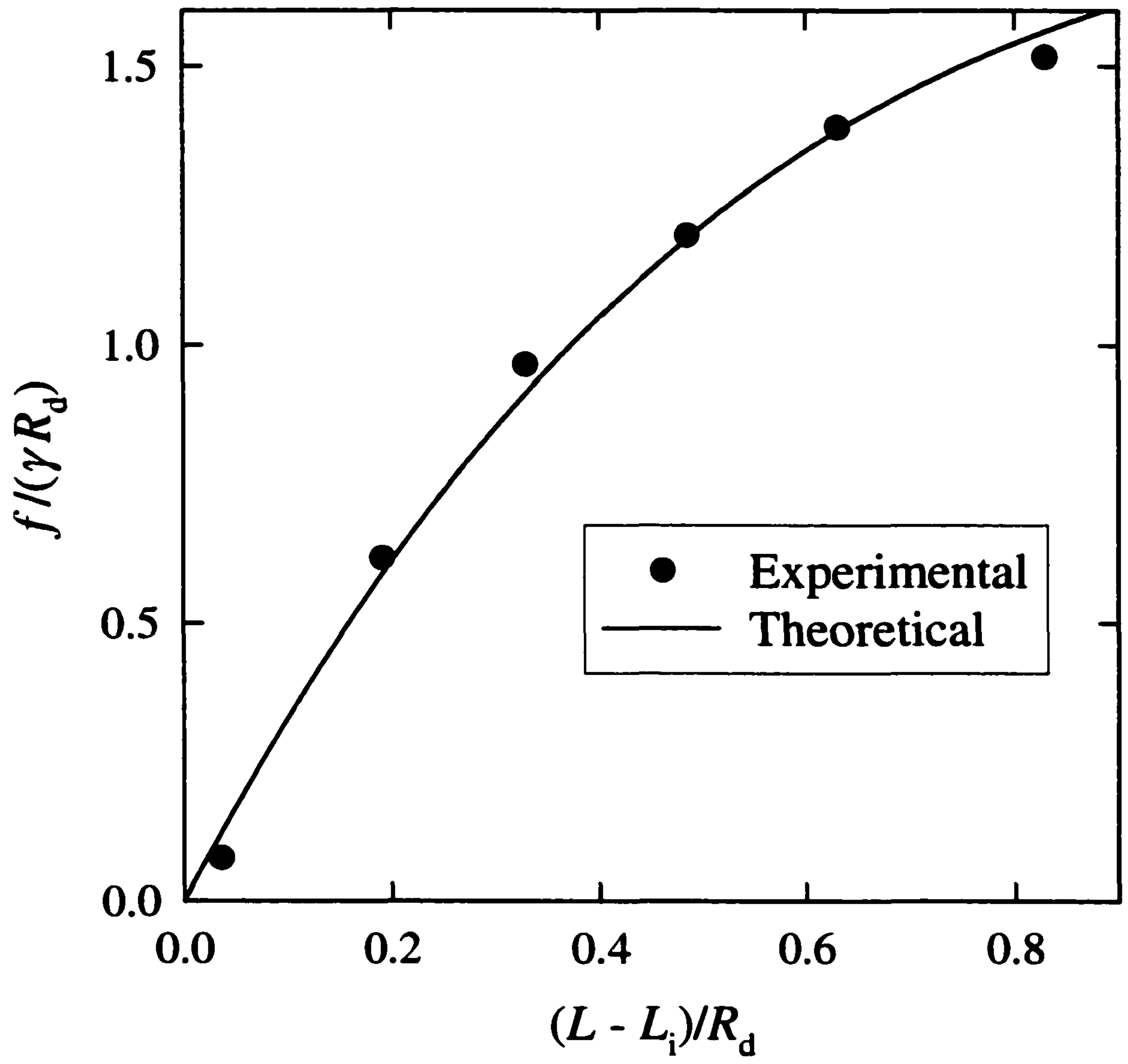

Figure 3.4. Determination of the interfacial tension γ by fitting the experimental $f - L$ data to a theoretical model based on the Young-Laplace relation. The measurements are taken from the case pH = 9.1 in figure 3.1a.

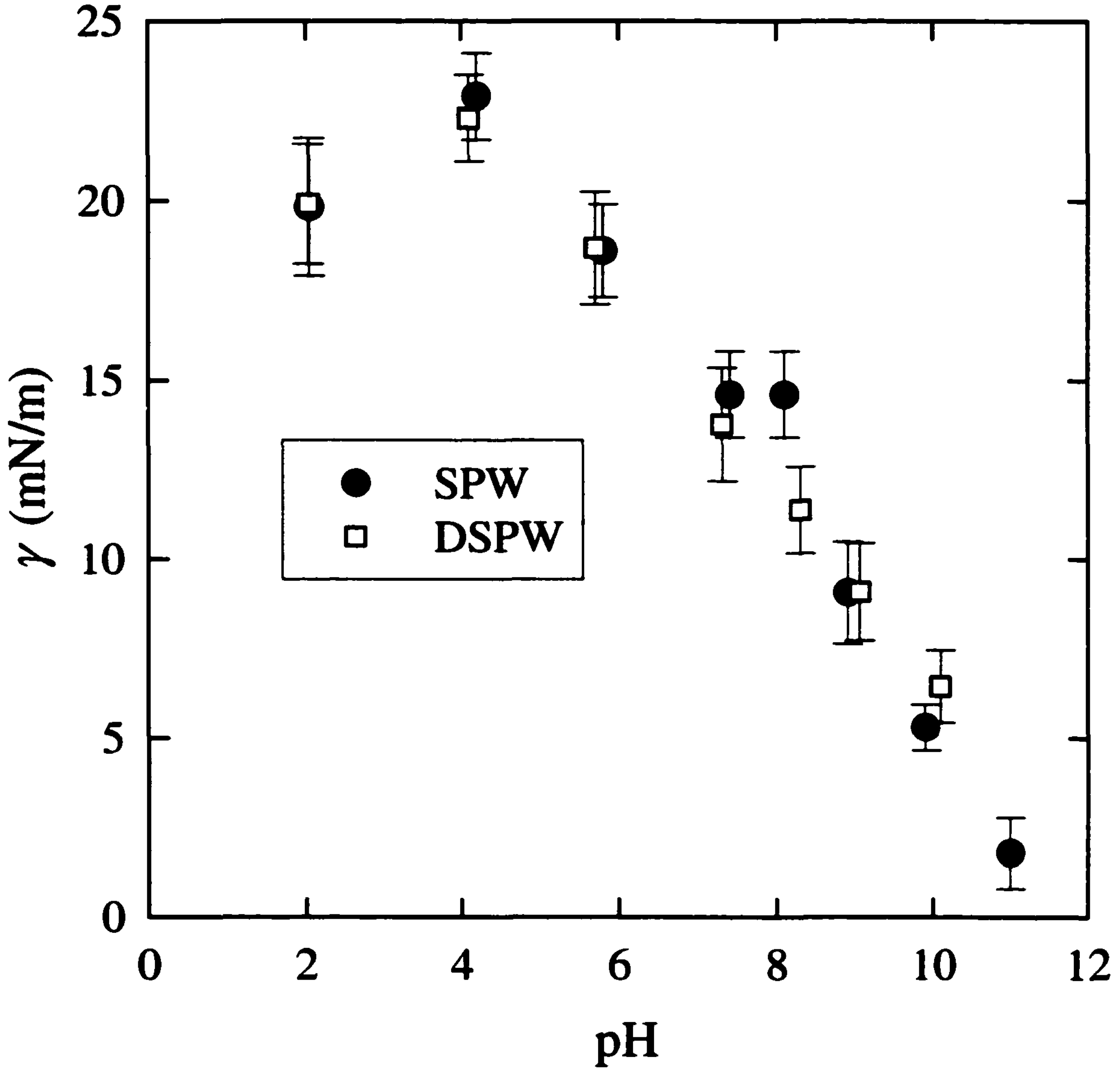

Figure 3.5. Interfacial tension γ of bitumen-in-water systems as a function of pH. Interfacial tensions are obtained, for bitumen drops in SPW (solid circles) and DSPW (open squares), by the method depicted in figure 3.4. For each data point, a minimum of 10 drops are analyzed, with the error bars showing the corresponding standard deviations. At pH > 11, the tension is below the detection limit of the microcantilever technique (<1mN/m).

At low pH values (pH < 4), the oil-water IFT for some North American bitumens (Drelich and Miller, 1994) and many crude oils (Cairns et al., 1976) experience sharp reductions (to less than 50% of the peak IFT value). Although the mechanism for this phenomenon is unclear, it has been speculated that the presence of sulphates (Takamura, 1985) and/or nitrogen bases, such as amines and amides (Cairns et al., 1976; Drelich and Miller, 1994), at the interface is responsible. As such a trend is not observed in the present study (figure 3.5) or for other Athabasca bitumens (Takamura and Isaacs, 1989; Basu et al., 1996), it appears that Athabasca bitumen may contain relatively low concentrations of sulphates, amines and/or amides. Although this is by no means conclusive, chemical analyses of Athabasca bitumen indeed reveal only low levels of sulphates (Schramm and Smith, 1985).

Over a wide range of pH, the interfacial tension of bitumen drops in simulated process water doped with divalents (DSPW) is nearly identical to that measured in SPW (figure 3.5). As the interfacial tension is unaffected, it is suggested that divalent cations, such as Ca^{++} and Mg^{++}, do not play a significant role in the equilibrium mechanical behaviour of Athabasca bitumen emulsion drops. This result may be due to the relatively low concentrations of divalents added in this study. Previous work on the effects of divalent ions on crude oil-water interfacial tension provide conflicting results, possibly due to the different crude oils used. Cairns and coworkers (1976), studying Zakum, Murban and Tia Juana (Mexico) crudes, indicated that aqueous solutions of calcium chloride caused a slight decrease in interfacial tension. However, other studies of North American crude oils suggest dramatic increases in crude oil-water interfacial tension in the presence of low concentrations of divalent ions (Trujillo, 1983; Sharma et al., 1989). In these studies, the interfacial tension behaviour is attributed to the ionization reaction kinetics and the surface affinity of ionized species.

To evaluate the effect of salts on bitumen-water interfacial tension, microcantilever measurements are conducted over a wide range of sodium chloride concentrations (figure 3.6). At low concentrations ([NaCl] < 0.2 M), the bitumen-water interfacial tension decreases dramatically upon addition of sodium chloride. At higher salt concentrations, the reduction in interfacial tension is less sharp and appears to reach an asymptotic value at about $\gamma \approx 12$ mN/m. In these solutions, the pH is not controlled

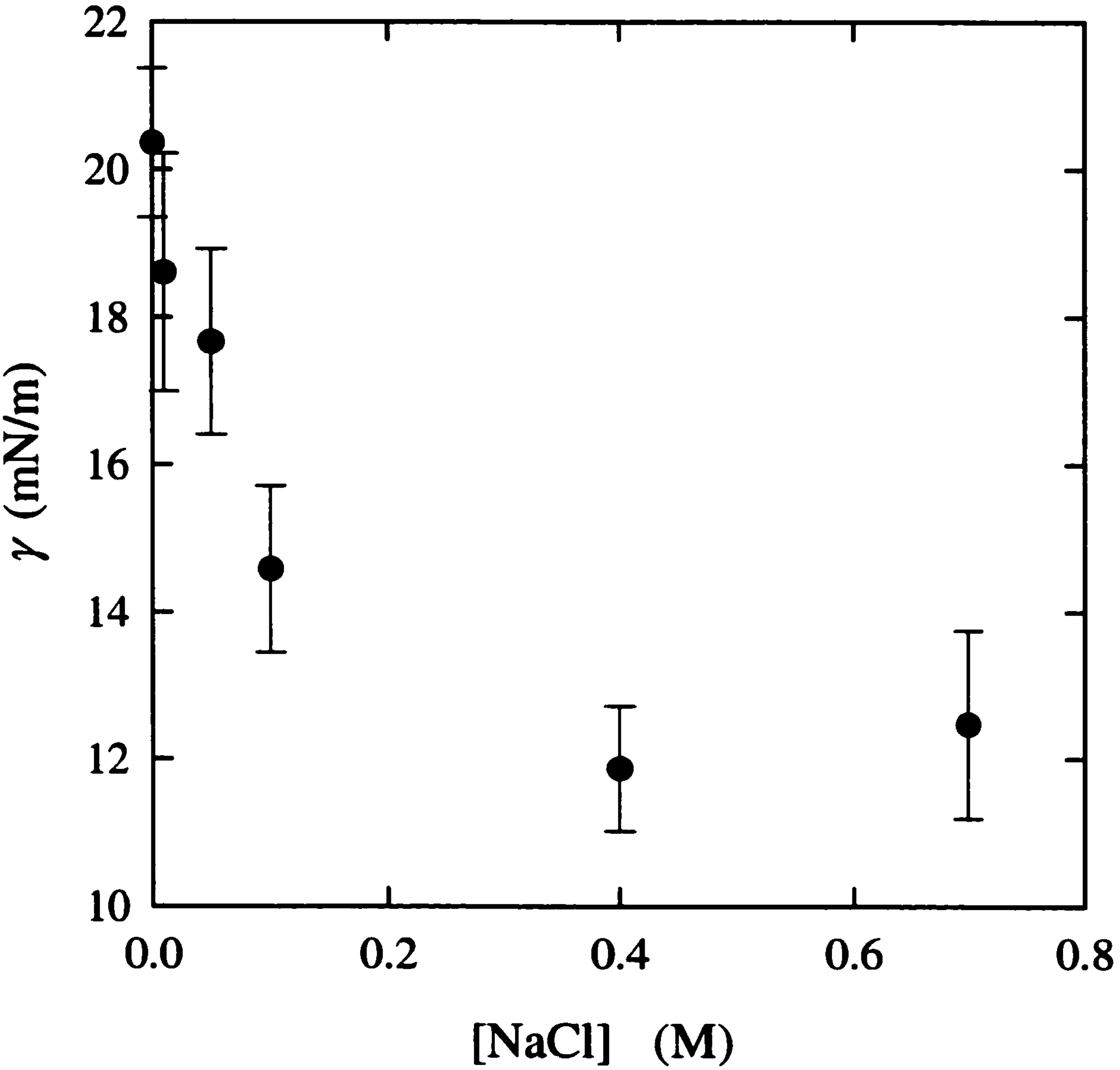

Figure 3.6. Interfacial tension γ of bitumen-in-water systems as a function of salt (NaCl) concentration. Interfacial tensions are obtained by the method depicted in figure 3.4. For each data point, a minimum of 10 drops are analyzed, with the error bars showing the corresponding standard deviations.

but appear to be fairly constant at pH ~ 6. In figure 3.6, each data point represents the average of a minimum of ten individual drop measurements, with the error bars giving the standard deviation. For each drop measurement, a minimum of six (*f*, *L*) data points are taken. This trend is consistent with that previously reported for Athabasca bitumen (Isaacs and Smolek, 1983; Takamura and Isaacs, 1989) and many crude oils (Cairns et al., 1976; Trujillo, 1983). Cairns and coworkers (1976) suggest that this behaviour is due to a reduction in repulsive interactions between charged surfactants as sodium ions accumulate at the interface. Alternatively, as noted in the previous paragraph, Trujillo (1983) and Sharma et al. (1989) account for this phenomenon through mass action relationships.

3.4 Conclusions

A novel micromechanical technique has been developed to quantify the interfacial tensions of density-matched and highly viscous emulsion drops. This microscopic method involves elongating individual, micron-sized drops using suction pipettes and measuring the applied stretching force through the use of a microcantilever. This study is the first to examine a primary interfacial property, the IFT, of bitumen-in-water emulsions at room temperature. Results suggest that increases in alkalinity and sodium ion concentration contribute to a reduction in bitumen-water interfacial tension. In addition, the presence of divalent ions in relatively low concentrations does not significantly affect bitumen-simulated process water interfacial tension. It is clear that further work on the mechanism of IFT reduction needs to be conducted.

Chapter 4

Dynamics of Emulsion Drop Shapes: Drop Shape Recovery Technique

4.1 Introduction

The shape dynamics of viscous drops in immiscible fluids, first studied in elegant experiments by Taylor (1932, 1934), is of longstanding fundamental interest. In addition, understanding the deformation of viscous drops is of importance for practical applications, such as dispersion technologies, polymer blending (Grace, 1982) and the pipeline transport of crude oil-water emulsions (Davis, 1988). Drop deformations resulting from shear flow fields have been well described and several excellent reviews are available (Acrivos, 1983; Rallison, 1984; Stone, 1994). Time-dependent recovery of an extended drop in a quiescent fluid has also been considered (c.f. Taylor, 1934; Stone et al., 1986). As discussed below, the insights from these experimental investigations were also seen in numerical computations of the drop dynamics (c.f. Stone and Leal, 1989a). Although these numerical simulations are wide ranging in their applications, they often encounter difficulties when one fluid is much more viscous than the other fluid.

In typical experimental studies of the dynamic behaviour of an extended drop in a quiescent medium, a drop is first elongated within a steady flow. The flow is then abruptly stopped and the transient drop shape is observed. The dynamics of this extended drop proceeds in one of two ways: the drop may relax back to its original spherical shape, or it may break up into a number of smaller droplets. This phenomenon was first observed by Taylor (1934), who developed a "four-roll mill" to elongate millimeter-sized hydrocarbon drops in aqueous simple shear or extensional flows. In a more recent study, it was confirmed that the drop shape dynamics was a function of the initial extension of the drop and the relative viscosities between the two fluids (Stone et al, 1986). In that study, an improved four-roll mill, capable of producing flow fields ranging from simple shear to extensional, was used to extend millimeter-sized silicon fluid drops in a variety of shearing flow fields of castor oil. Following abrupt cessation of the flow, it was noted that drops extended below a critical elongation ratio, where the elongation ratio is defined as the extended drop length L divided by its diameter $2R_d$ (R_d is the spherical drop radius), always relaxed back to spheres. Drops that were extended above this critical elongation ratio would break up into smaller droplets. The critical elongation ratio was shown to be a strong function of the viscosity ratio λ, defined as the drop viscosity μ divided by that of the continuous fluid $\bar{\mu}$. Interestingly, the critical elongation ratio exhibited a minimum at $\lambda = 1$, and increased as $\lambda \rightarrow 0$ and $\lambda \rightarrow \infty$. This suggests that an extended, highly viscous drop (i.e., $\lambda \rightarrow \infty$) will likely relax to a sphere, provided the initial elongation is not too large ($L/2R_d < 10$). The drop shape dynamics was attributed to localized flows developed by the curvature of the interface. The recovery and breakup of immiscible polymer melts have also been studied, with the aim of estimating the tension between the two phases (Carriere et al., 1989). The shape evolution was described using a one-dimensional lumped-parameter equation that balances the capillary forces with the viscous resistance of the fluids (Cohen and Carriere, 1989). However, in light of the simple nature of the model, tension estimates based on this method were approximate at best and the authors acknowledged the need for a better theoretical description of the relaxation process.

Although analytical analyses have been developed to describe drop shape dynamics, they are limited to either small deformations, as first described by Taylor (1932, 1934), or large deformations based on slender body theories (Taylor, 1964). Numerical solutions have proved useful in describing drop deformations ranging from nearly spherical to highly extended. The most common numerical method is the boundary integral technique (Youngren and Acrivos, 1975). This integral approach, first applied to free-boundary creeping flow problems by Youngren and Acrivos (1976), recasts the Stokes equation in such a form that only velocities and Stokeslets on the drop surface are evaluated. The boundary integral technique has been adapted to model steady shapes of axisymmetric drops in steady extensional flows over viscosity ratios ranging from $0.3 \leq \lambda \leq 100$ (Rallison and Acrivos, 1978). The procedure has also been used to examine drop deformations for non-axisymmetric drop geometries for $\lambda = 1$ (Rallison, 1981) and deformations of toroidal drop shapes formed in biaxial extensional flows at moderate viscosity ratios of $\lambda = 1$ and $\lambda = 10$ (Stone and Leal, 1989b). In general, numerical results for steady drop deformations in shear flows agree well with the small deformation and slender body theories pioneered by Taylor (1934, 1964).

Stone and Leal (1989a), after validation of the boundary integral method for drop deformations in steady flows, advanced this technique to describe the time evolution of uniaxially extended viscous drops ($0.05 \leq \lambda \leq 10$) in quiescent fluids. Their numerical results correspond with the experimental observations of Stone and coworkers (1986), suggesting that interfacial tension-driven dynamics of extended drops are due to local variations in surface curvature and the viscosity ratio λ of the immiscible fluids (Stone and Leal, 1989a). This observation was confirmed by experiments and by boundary integral calculations (Tjahjadi et al., 1992). The boundary integral method can be applied over a wide range of viscosity ratios λ and is greatly simplified when $\lambda = 1$ (Rallison, 1981). However, singular behaviours are encountered at limiting viscosity ratios of $\lambda = 0$ and $\lambda = \infty$, rendering the boundary-integral technique ineffective in these regimes (Rallison and Acrivos, 1978; Acrivos, 1983; Rallison, 1984). In addition, at low viscosity ratios ($\lambda < 0.1$), the boundary integral formulation leads to significant problems associated with volume conservation (Rallison and Acrivos, 1978; Stone and Leal, 1989a). This is due to singularities appearing at $\lambda = 0$ (Rallison and Acrivos, 1978). Such a difficulty was dealt with by rescaling the drop shape every few time steps[11].

In this chapter, a novel micropipette technique is introduced that allows for the extension and shape relaxation of individual emulsion drops in quiescent media, avoiding the need for complex flow generating devices employed in traditional drop deformation experiments. To complement the micropipette *drop shape recovery* experiments, a procedure for calculating the low Reynolds number dynamic behaviour of an extended drop in a quiescent fluid is developed. First discussed by Tran-Son-Tay and coworkers (1991) for the relaxation of white blood cells in a plasma medium, this variational approach is extended to incorporate a viscous exterior fluid for arbitrary λ, including $\lambda = 0$ and $\lambda = \infty$. This Stokesian model assumes that the shape dynamics is driven by a constant interfacial tension and rate-limited by the fluid viscosities. The validity of this

---

[11] Although geometric scaling appears to have little effect on the basic shape of the drop and critical conditions for breakup (*i.e.*, critical elongation ratio), the time scale of the deformation is affected (Stone and Leal, 1989a).

analysis is demonstrated by comparing drop shape recovery data at moderate viscosity ratios with that obtained with the well-established boundary-integral method. The present approach is unique for its ability to handle systems of limiting viscosity ratios λ, where one fluid is much more viscous than the other ($\lambda = 0$ and $\lambda = \infty$). It also has no problem with volume conservation. Its application to systems exhibiting $\lambda \approx \infty$ is demonstrated experimentally.

4.2 Theoretical Background

As discussed above, previous numerical procedures describing drop shape dynamics are ineffective at limiting viscosity ratios of $\lambda = 0$ and $\lambda = \infty$. In this section, a boundary least squares technique is presented which addresses moving boundary creeping flow (Stokesian) problems where $0 \leq \lambda \leq \infty$ for the recovery of an extended drop in an immiscible quiescent fluid.

4.2.1 Description of the Stokesian model

In this description of the behaviour of an axisymmetrically extended drop in a quiescent fluid, it is assumed that the shape dynamics is driven by a uniform interfacial tension and rate-limited by the fluid viscosities. In this analysis, both the drop and the surrounding fluid are Newtonian, with viscosities μ and $\bar{\mu}$, respectively. A uniform tension γ is assumed to exist at the interface. Moreover, it is noted that external body forces, such as buoyancy forces, are negligible due to the small drop size and/or the fact that the densities of the two phases are matched[12]. Inertial effects are also negligible due to the small drop size and the relatively large viscous forces encountered (i.e., low Reynolds number flow). As such, the governing equations for the drop phase and the surrounding liquid (denoted by the overbar) are the quasi-steady Stokes flow relations:

$$\mu \nabla^2 \boldsymbol{u} = \nabla p , \quad \nabla \cdot \boldsymbol{u} = 0$$
$$\bar{\mu} \nabla^2 \bar{\boldsymbol{u}} = \nabla \bar{p} , \quad \nabla \cdot \bar{\boldsymbol{u}} = 0 ,$$

---

[12] This may be shown in the Bond number $B_o = \Delta\rho g R_d^2/\gamma$, which compares buoyancy forces to the tension forces of these drops. With $\Delta\rho \sim 100$ kg/m^3, $R_d \sim 10^{-5}$m and $\gamma \sim 0.01$ N/m, one has $B_o \sim 10^{-5}$ indicating that gravity plays a negligible role in deforming these drops.

where $\boldsymbol{u}$ and p are the velocity vector and pressure field, respectively. Definitions of the geometric parameters observed in this analysis are shown in figure 4.1.

The Stokes equations must be solved subject to appropriate boundary conditions. First, the fluid velocities must be continuous across the interface (the no-slip condition). This is represented in spherical coordinates (R, θ) by

$$u_R = \bar{u}_R$$
$$u_\theta = \bar{u}_\theta. \tag{4.1}$$

It is implicit that the velocity approaches zero as $R \rightarrow \infty$. The conditions of mechanical equilibrium must also be satisfied at the interface. Thus, a second constraint to the solution requires that stress-type boundary conditions at the interface are specified by

$$\sigma_R - \bar{\sigma}_R + T_R = 0$$
$$\sigma_\theta - \bar{\sigma}_\theta + T_\theta = 0, \tag{4.2}$$

where $\{\sigma_R, \sigma_\theta\}$ and $\{\bar{\sigma}_R, \bar{\sigma}_\theta\}$ are components of the hydrodynamic stress tensor at the interface due to the drop fluid and the continuous phase, respectively. In addition, the stresses originating from the interface are represented by $\{T_R, T_\theta\}$. The subscripts R and θ refer to stresses in the R- and θ-directions, respectively (figure 4.1).

It is now necessary to define appropriate constitutive relations for the stresses at the interface (equations 4.2). The stresses at the interface due to the drop curvature act only normal to the interface and are represented by the Young-Laplace equation. In spherical coordinates, these are given by

$$T_R = \gamma J \cos\psi$$
$$T_\theta = \gamma J \sin\psi. \tag{4.3}$$

Due to the assumption of uniform tension, the net tangential stress at the drop surface must vanish. In equations 4.3, γ is the equilibrium interfacial tension, J is the local curvature and ψ is the angle between the R coordinate and the unit normal to the drop interface (figure 4.1). Explicit representations of J and ψ, in terms of curvilinear coordinates, are required in the numerical solution to this Stokesian problem (Appendix D). Constitutive relations for the hydrodynamic stresses at any arbitrary interface are obtained from standard stress equations for Newtonian fluids.

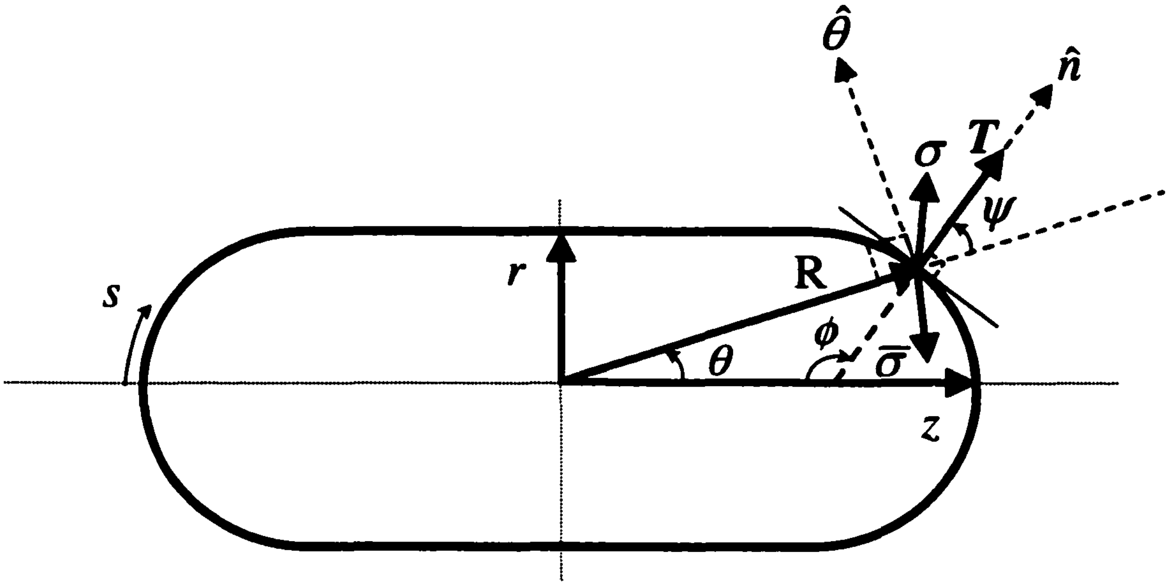

$$\psi = \Pi - (\phi + \theta)$$

Figure 4.1. Description of an axisymmetric drop shape. The spherical coordinates are defined by (R, θ), while (s, ϕ) define the curvilinear coordinates, with s giving the curvilinear distance along the interface. The cylindrical coordinates are given by (r, z), with z being the axis of symmetry. The angle ϕ is that between the z axis and a vector normal to the interface at s. The angle ψ is that between a vector along the R axis and a vector normal to the interface at s. Also shown is the tension T that acts normally to the interface and the hydrodynamic stress tensors $\sigma, \bar{\sigma}$.

For the drop fluid, these stresses (Bird et al., 1960) are given by

$$\begin{aligned}
\sigma_{RR} &= -p + 2\mu\frac{\partial u_R}{\partial R} \\
\sigma_{R\theta} &= \mu\left[R\frac{\partial}{\partial R}\left(\frac{u_\theta}{R}\right) + \frac{1}{R}\left(\frac{\partial u_R}{\partial \theta}\right)\right] \\
\sigma_{\theta\theta} &= -p + 2\mu\left[\frac{1}{R}\left(\frac{\partial u_\theta}{\partial \theta}\right) + \frac{u_R}{R}\right].
\end{aligned} \tag{4.4}$$

Identical relations may be given for the continuous phase simply by substituting the appropriate variables (i.e., $\bar{u}_R$ for u_R, $\bar{\mu}$ for μ, etc.). For the drop liquid, the hydrodynamic stress components exerted at an arbitrary interface are obtained through the following projections:

$$\begin{aligned}
\sigma_R &= \sigma_{RR}\cos\psi + \sigma_{R\theta}\sin\psi \\
\sigma_\theta &= \sigma_{R\theta}\cos\psi + \sigma_{\theta\theta}\sin\psi.
\end{aligned} \tag{4.5a}$$

For the continuous phase, an identical transformation yields the appropriate hydrodynamics stress components,

$$\begin{aligned}
\bar{\sigma}_R &= \bar{\sigma}_{RR}\cos\psi + \bar{\sigma}_{R\theta}\sin\psi \\
\bar{\sigma}_\theta &= \bar{\sigma}_{R\theta}\cos\psi + \bar{\sigma}_{\theta\theta}\sin\psi.
\end{aligned} \tag{4.5b}$$

Now that the boundary conditions have been established, expressions for the velocity and pressure fields for use in equations 4.4 are required. Fortunately, exact series solutions to axisymmetric Stokes flow are available in general spherical coordinates (Happel and Brenner, 1973). For the drop phase, the velocity and pressure fields are given by

$$\begin{aligned}
u_R &= -\sum_{n=2}^{\infty}(A_n R^{n-2} + C_n R^n)P_{n-1}(\cos\theta) \\
u_\theta &= \sum_{n=2}^{\infty}\left(nA_n R^{n-2} + (n+2)C_n R^n\right)\frac{I_n(\cos\theta)}{\sin\vartheta} \\
p &= \Pi - 2\mu\sum_{n=2}^{\infty}\left(\frac{2n+1}{n-1}\right)C_n R^{n-1}P_{n-1}(\cos\theta).
\end{aligned} \tag{4.6}$$

The velocity field and pressure field expressions for the external fluid are given by

$$\begin{aligned} \bar{u}_{\mathrm{R}} &= -\sum_{n=2}^{\infty}(B_n R^{-n-1} + D_n R^{-n+1})P_{n-1}(\cos\theta) \\ \bar{u}_{\theta} &= \sum_{n=2}^{\infty}\left(-(n-1)B_n R^{-n-1} - (n-3)D_n R^{-n-1}\right)\frac{I_n(\cos\theta)}{\sin\theta} \\ \bar{p} &= -2\bar{\mu}\sum_{n=2}^{\infty}\left(\frac{2n-3}{n}D_n R^{-n}\right)P_{n-1}(\cos\theta). \end{aligned} \qquad (4.7)$$

In equations 4.6 and 4.7, $P_n(\cos\theta)$ and $I_n(\cos\theta)$ are the Legendre polynomials and Gegenbauer polynomials of order n, respectively. The Gegenbauer polynomials may be further expressed in terms of the Legendre polynomials (Appendix E).

4.2.2 Variational (boundary least squares) solution to Stokesian model

Although the velocity and pressure fields given in equations 4.6 and 4.7 are exact solutions, they are not uniquely defined as they contain the undetermined coefficients Π, A_n, B_n, C_n and D_n. In order to obtain an optimal set of coefficients, a variational scheme is implemented on the boundary conditions (equations 4.1 and 4.2) such that the following functional ε is minimized

$$\varepsilon = \int\left[(\sigma_{\mathrm{R}} - \bar{\sigma}_{\mathrm{R}} + T_{\mathrm{R}})^2 + (\sigma_{\theta} - \bar{\sigma}_{\theta} + T_{\theta})^2 + (u_{\mathrm{R}} - \bar{u}_{\mathrm{R}})^2 + (u_{\theta} - \bar{u}_{\theta})^2\right] r\,\mathrm{d}s. \qquad (4.8)$$

Equation 4.8 provides an estimate of the errors summed over the entire drop surface for any given set of undetermined coefficients. A linear system of equations may be obtained through differentiation of equation 4.8 with respect to the unknown coefficients such that

$$\frac{\partial\varepsilon}{\partial a_n} = 2\int\begin{bmatrix} (\sigma_{\mathrm{R}} - \bar{\sigma}_{\mathrm{R}} + T_{\mathrm{R}})\dfrac{\partial(\sigma_{\mathrm{R}} - \bar{\sigma}_{\mathrm{R}})}{\partial a_n} + (\sigma_{\theta} - \bar{\sigma}_{\theta} + T_{\theta})\dfrac{\partial(\sigma_{\theta} - \bar{\sigma}_{\theta})}{\partial a_n} + \\ (u_{\mathrm{R}} - \bar{u}_{\mathrm{R}})\dfrac{\partial(u_{\mathrm{R}} - \bar{u}_{\mathrm{R}})}{\partial a_n} + (u_{\theta} - \bar{u}_{\theta})\dfrac{\partial(u_{\theta} - \bar{u}_{\theta})}{\partial a_n} \end{bmatrix} r\,\mathrm{d}s = 0. \qquad (4.9)$$

In equations 4.9, the variables a_n represent the unknown coefficients $\{\Pi, A_n, B_n, C_n, D_n\}$ that are to be optimized. This linear system of equations is now easily solved through matrix inversion techniques. Further details of this solution are discussed in Appendix E.

Solutions to equations 4.9 provide optimized values of the coefficients $\{\Pi, A_n, B_n, C_n, D_n\}$. Once these are known, the velocity and pressure profiles at any point may be determined. To follow the dynamic shape recovery, the drop shape is incremented, based on the velocity field, in small time steps Δt. The initial shape must be known *a priori*. The initial velocity field $\{u_R, u_\theta\}$ is calculated from the drop shape at time $t = 0$. The shape is then incremented by the following kinematic condition at time $t + \Delta t$

$$\begin{aligned} r_{t+\Delta t} &= r_t + (u_R \sin\theta + u_\theta \cos\theta)\Delta t \\ z_{t+\Delta t} &= z_t + (u_R \cos\theta + u_\theta \sin\theta)\Delta t, \end{aligned} \tag{4.10}$$

where r and z represent the axisymmetric drop shape profile in cylindrical coordinates (figure 4.1). In equations 4.10, the terms in brackets are the drop velocities in the r and z directions, respectively. Once the updated drop shape is known, the new velocity field is calculated through the optimized solution to equations 4.6 and 4.7, and the shape is once again incremented (equation 4.10). This procedure is repeated until an equilibrium shape is observed. In the analysis of such a process, the dimension of primary interest is the axial drop length L at time t. This parameter is found to adequately describe the dynamics of the shape recovery through an extension ratio, defined as $L/2R_d$.

To facilitate analysis, all lengths are scaled by L_0, the maximum axial drop length, while velocities are scaled by a characteristic velocity γ/μ. By doing so, the scaling parameters for stresses are uniquely determined; the hydrodynamic stresses and interfacial stresses $\boldsymbol{T}$ are scaled by γ / L_0. In addition, this dimensional analysis provides a dimensionless recovery time $\gamma t/\mu L_0$. (Thus, all velocities are measured in units of characteristic velocity, time in units of $\mu L_0/\gamma$, and stresses in units of γ / L_0.) In such an analysis, the viscosity ratio λ is the dimensionless group that describes the shape recovery of an extended drop, given its initial shape.

The variational solution describes the recovery of an extended drop to a spherical shape. In general, due to the axisymmetric nature of the problem about the z-axis, only the contour of half of the shape ($r \geq 0$) is required. In this computation, the half contour of the shape is discretized into 181 equally spaced nodal points. To demonstrate the robustness of the technique, the time step Δt (in equations 4.10) and the number of terms

N in the series solutions for the velocity and pressure fields (equations 4.6 and 4.7) are varied over a range of viscosity ratios λ. Nearly identical results for a given initial drop shape and λ are noted as $0.025 \leq \Delta t \leq 0.05$ and $46 \leq N \leq 78$. All subsequent calculations are performed with a time step $\Delta t = 0.05$ and $N = 78$. The boundary least squares numerical code solving this Stokesian model is given in Appendix F.

4.2.3 Comparison to boundary integral method

The boundary integral method has been previously used to study the relaxation of initially extended drops in quiescent fluids (Stone and Leal, 1989a). Such analyses have been limited to moderate λ due to numerical difficulties at limiting viscosity ratios. Comparisons between the boundary integral method, as applied by Tjahjadi and coworkers (1994), and the present boundary least squares numerical scheme are made at moderate λ (λ = 0.01, 1, and 10). The initial shape used for these calculations is a cylindrical tube with hemispherical endcaps. The profile of the initial shape, with dimensions of $L_o/b = 2.5$ (where b is the diameter of the cylindrical midsection of the shape), is shown in figure 4.2. The time-dependent recovery of such extended drops, monitored via the extension ratio $L/2R_d$, show excellent agreement as calculated by both techniques at moderate λ (figure 4.2). Although the boundary integral analyses provided by Tjahjadi et al. (1994) were continuous in time, for clarity only specific points from their simulation are plotted (shown as symbols). Note that time is scaled with the exterior fluid viscosity $\bar{\mu}$ so that all three curves could be presented in the same figure (if μ was chosen instead, then the time scale for the $\lambda = 0.01$ curve would be 100 times greater). In all cases, the drops recover to a final extension ratio of $L/2R_d = 1$ (i.e., the final axial length L of the shape is equal to the radius of a sphere of equal volume), indicating that volume is preserved.

Since the present variational solution incorporates the Young-Laplace relation (equation 1.1), the transient shape profile of a recovering drop should be well described. The profile of a typical shape recovery for an extended drop at $\lambda = 1$ is given in figure 4.3. Note that the initial shape ($L_o/b = 2.5$) is identical to that in figure 4.2. As time (scaled here by $\bar{\mu}L_o/\gamma$) proceeds, the axially extended ends of the drop retract towards the center

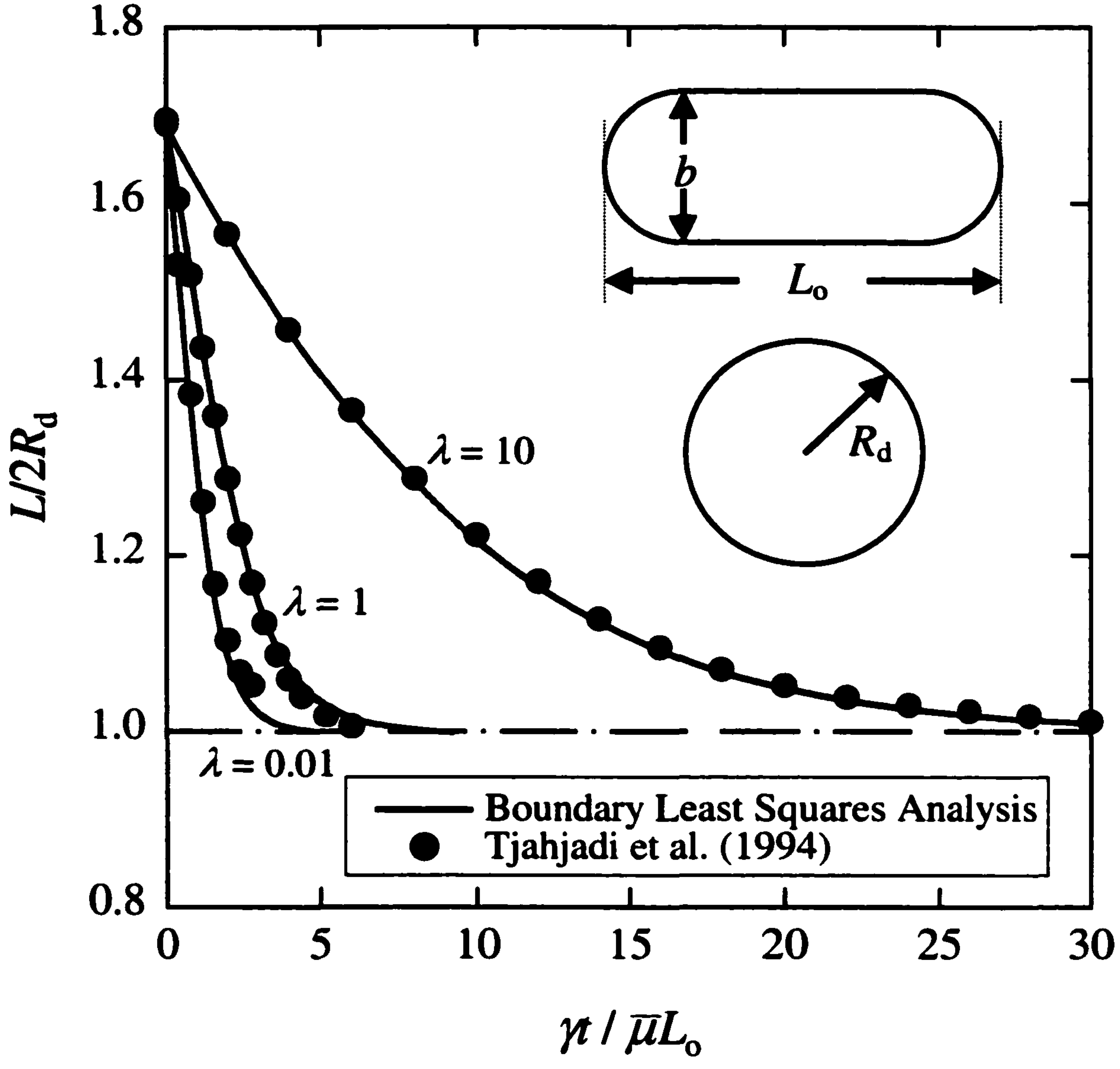

Figure 4.2. Comparison of the current boundary least squares (lines) and boundary integral (symbols) solutions at moderate λ (λ = 0.01, λ = 1 and λ = 10). The extension ratio $L/2R_d$ is plotted as a function of the dimensionless time $\gamma t/\bar{\mu}L_o$, where L_o is the initial (maximum) axial drop length and R_d is the radius of a sphere of equal volume to the initial shape. The initial shape, with a dimension of $L_o/b = 2.5$, and boundary integral calculations are obtained from Tjahjadi et al. (1994). The broken line at $L/2R_d = 1$ indicates a natural, spherical shape.

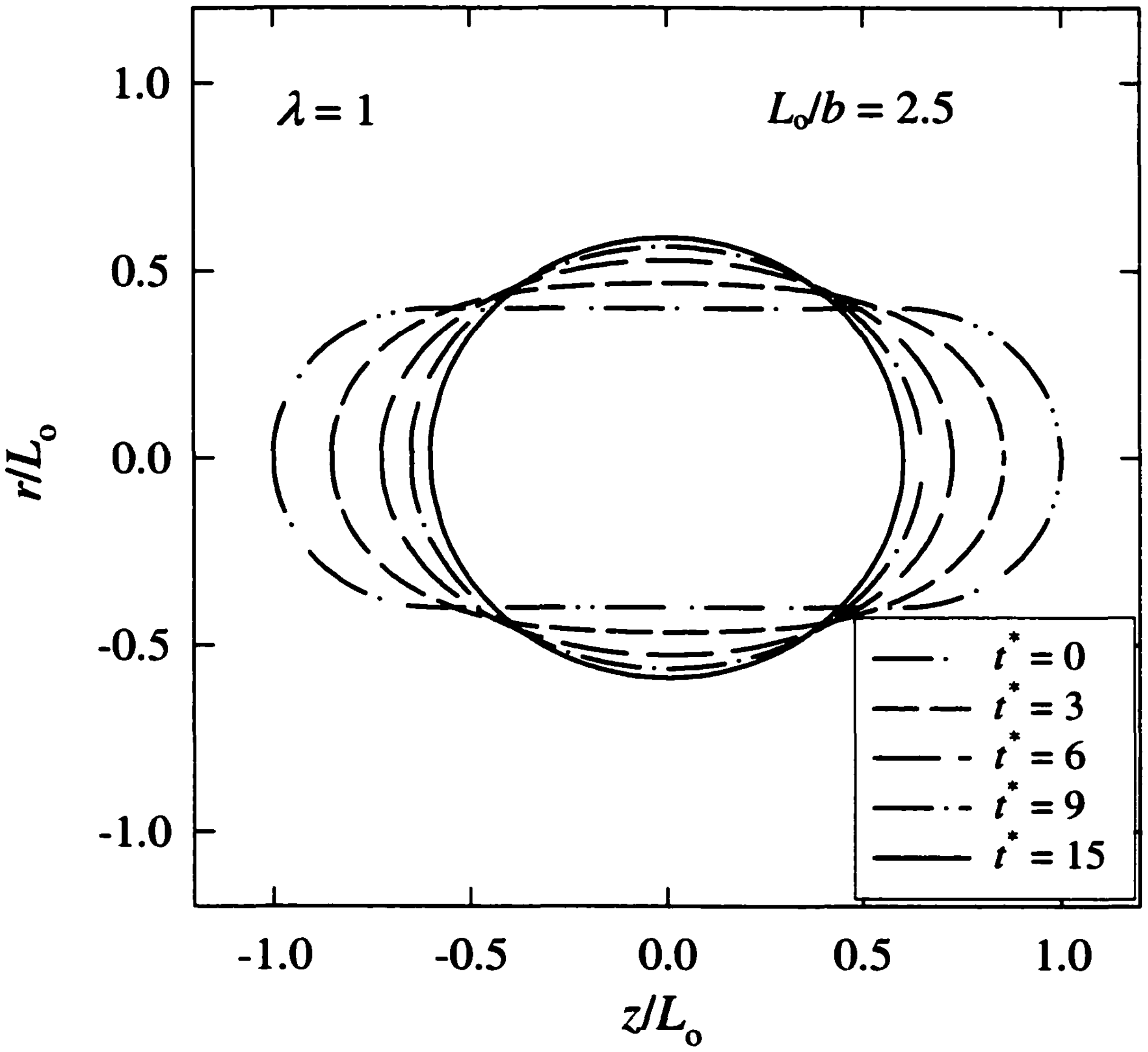

Figure 4.3. Boundary least squares simulation of the shape profile recovery of an extended drop for $\lambda = 1$. The initial shape is the same as that of figure 4.2 ($L_0/b = 2.5$) and the dimensionless recovery time is defined as $t^* = \gamma t/\mu L_0$.

with fore-aft symmetry ($z = 0$), while the cylindrical central section moves away from the drop center, until the drop attains a spherical configuration[13]. Throughout the entire recovery, the drop profile remains smooth and continuous. From figures 4.2 and 4.3, it is clear that the variational analysis provides adequate descriptions of drop shape dynamics at moderate λ.

4.2.4 Implementation of the variational approach at $\lambda = 0$ and $\lambda = \infty$

At limiting viscosity ratios, the boundary least squares technique may be applied to describe the shape recovery of extended drops. Figure 4.4 depicts such a recovery process for the same initial shape profile shown in figure 4.2 ($L_0/b = 2.5$) for both $\lambda = 0$ (*i.e.*, an inviscid drop) and $\lambda = \infty$ (*i.e.*, an inviscid continuous phase). Recall that numerical simulation of drop dynamics is not possible with the boundary integral technique at these limiting regimes (Acrivos, 1983; Rallison, 1984). In figure 4.4, recovery time is scaled by the drop viscosity $\mu L_0 / \gamma$ for the $\lambda = \infty$ curve, while for the $\lambda = 0$ curve, it is scaled by $\bar{\mu} L_0 / \gamma$. It was noted above that the boundary integral method experienced difficulties in maintaining volume conservation as $\lambda \rightarrow 0$. As the final extension ratio $L/2R_d$ approaches unity for both curves in figure 4.4, it is evident that the present variational technique adequately satisfies volume conservation at both limiting regimes. In the present analysis, geometric rescaling is never required. In fact, for all cases examined, the maximum volume loss is less than 1% (and often less than 0.01 %).

As observed at moderate λ, the drop shape profiles remain smooth and continuous during the recovery process (shown for $\lambda = \infty$ in figure 4.5). It was noted above that the boundary integral method is most efficient at $\lambda = 1$ (Rallison, 1981). It is interesting to point out that the present variational analysis operates most efficiently at the limiting viscosity ratios ($\lambda = 0, \infty$) due to its formulation. In the limiting regimes, one fluid is inviscid, which allows for the relaxation of velocity continuity across the interface (equation 4.1) and greatly simplifies the stress boundary conditions (equation 4.2).

---

[13] This result is to be expected, as the initial shape was below the critical elongation ratio at $\lambda = 1$. For drop breakup to proceed, $L/2R_d$ must be greater than 3.5 (Stone et al., 1986). As shown in figure 4.2, the maximum elongation ratio in this analysis is $L/2R_d = 1.69$, occurring at $\gamma t / \bar{\mu} L_0 = 0$.

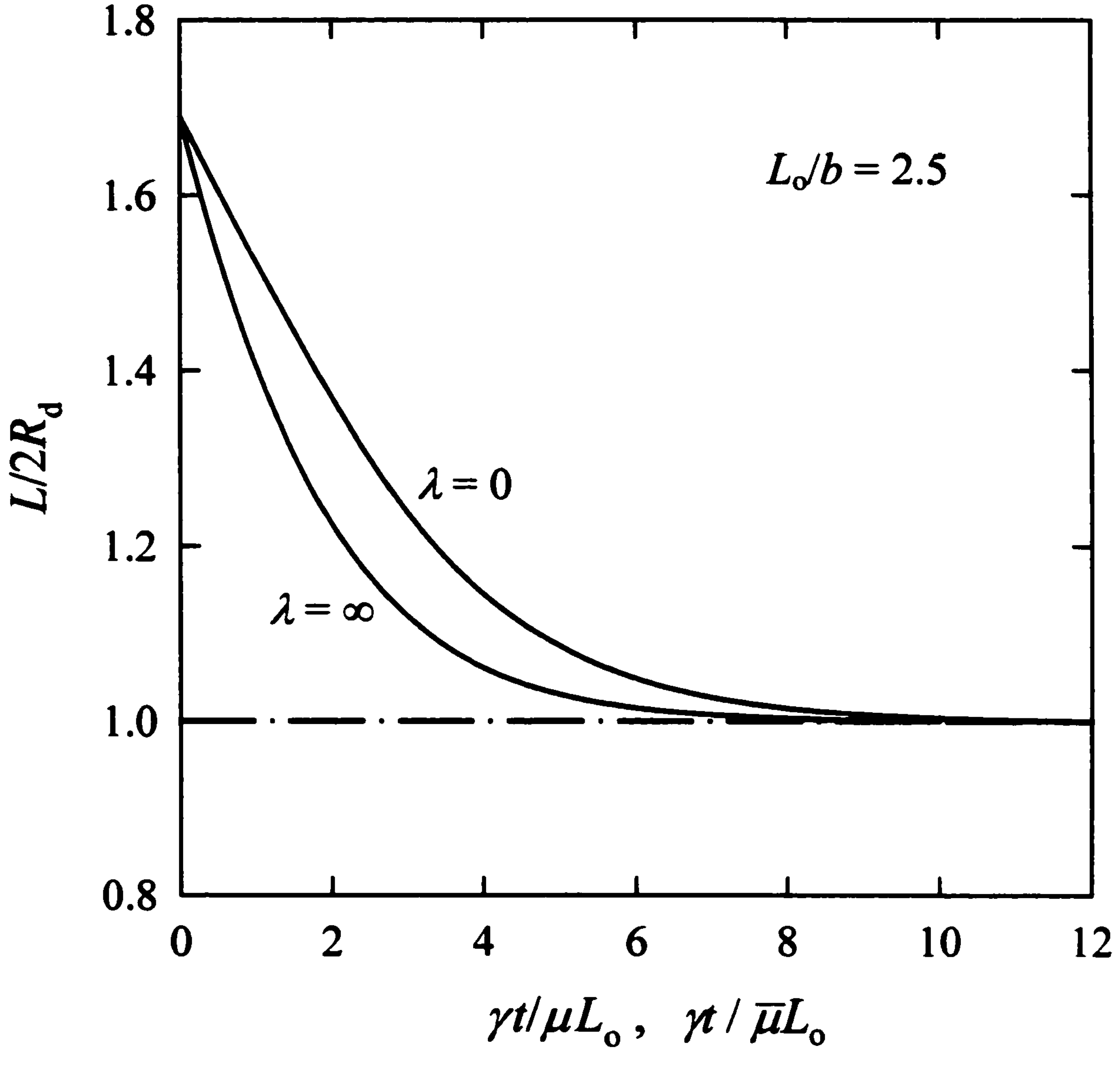

Figure 4.4. Boundary least squares simulation of drop recoveries at limiting viscosity ratios $\lambda = 0$ and $\lambda = \infty$. The drop extension ratio $L/2R_d$ is plotted as a function of the appropriate dimensionless time. For $\lambda = \infty$, time is scaled by the drop viscosity μ such that the recovery time is $\gamma t/\mu L_0$. For $\lambda = 0$, time is scaled by the continuous phase viscosity $\bar{\mu}$ such that the recovery time is $\gamma t/\bar{\mu} L_0$. As in figure 4.2, the broken line at $L/2R_d = 1$ is representative of a spherical drop. The initial drop shapes are the same as that shown in figure 4.2 ($L_0/b = 2.5$).

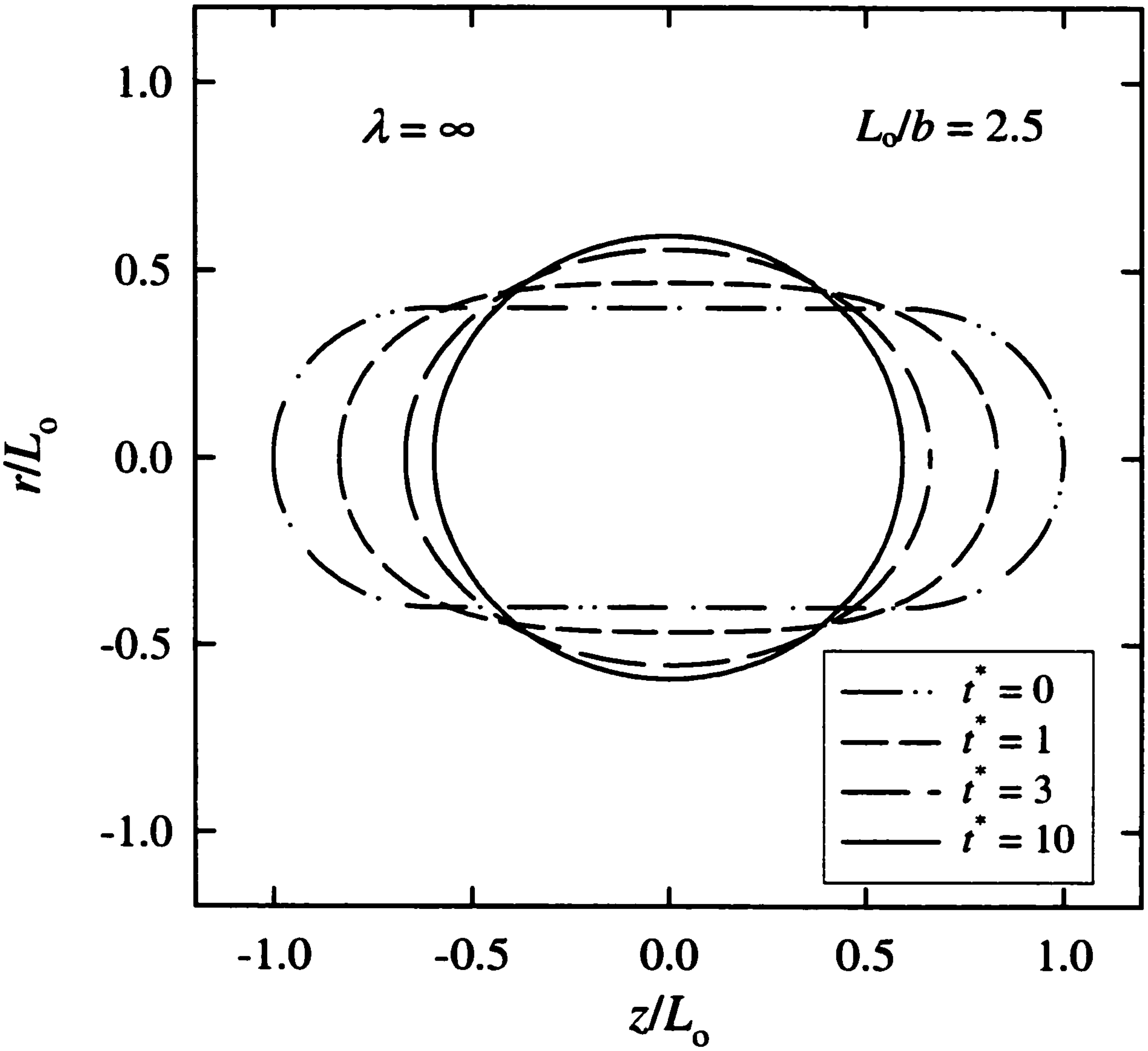

Figure 4.5. Boundary least squares simulation of the shape profile recovery of an initially extended drop for $\lambda = \infty$. The initial shape and the dimensionless recovery time are the same as for figure 4.2.

4.3 Experimental Verification of the Boundary Least Squares Technique at $\lambda = \infty$

Previously developed numerical methods describing the shape evolution of extended drops break down at limiting viscosity ratios ($\lambda = 0$ and $\lambda = \infty$), leaving no technique with which to compare the present variational calculations at these λ's. In this section, the applicability of the boundary least squares algorithm with $\lambda = \infty$ for solving moving boundary creeping flow problems is demonstrated for highly viscous drops in a relatively low viscosity medium (i.e., $\lambda \approx \infty$). Experimental drop deformations are achieved via a novel micropipette technique, eliminating the need for a flow generating apparatus. To describe the evolution of extended viscous drops, *a priori* knowledge of the fluid viscosities and the interfacial tension between the fluids is required.

4.3.1 Fluid systems and emulsion drop formation

To demonstrate the applicability of the variational (boundary least squares) analysis at $\lambda = \infty$ to a drop recovery process where $\lambda \approx \infty$, fluid drops of extremely high viscosity relative to the continuous fluid (water) are required. In this study, Cannon Standard Oils N190000 and N450000 (Cannon Instrument Co., PA), which have viscosities of approximately 700,000 and 1.9×10^6 times that of water at 22.5°C, respectively (Table 4.1), are chosen as the disperse phase (drop) fluids. The viscosities of these polybutene oils were determined over a wide temperature range by the Cannon Instrument Company using a Cannon-Ubbelohde Master viscometer following ASTM D2162. The viscosity data were reported with ± 0.17% accuracy (at 20°C) according to ISO 3666. In these viscosity measurements, temperatures were traceable to the National Institute for Standards and Technology Test No. 260470. Cannon noted that these viscosity standard oils are Newtonian over a wide range of shear rates.

Table 4.1. Properties of Cannon viscosity standard oils at 22.5°C. The viscosity and specific gravity data are provided by Cannon Instruments Ltd. The interfacial tensions are measured using the microcantilever technique.

Viscosity Standard (Cannon Ltd.)	*Viscosity (Pa·s)*	*Specific Gravity (-)*	*Interfacial Tension (mN/m)*
N190000	699	0.85 - 0.91	41.7 ± 1.3
N450000	1895	0.85 - 0.91	43.3 ± 1.5

The interfacial tensions of fluid systems in which at least one fluid is highly viscous are difficult to quantify with conventional tensiometers. This is a result of long equilibration times required to allow for viscous relaxation (see chapter 3). As such, the recently developed microcantilever technique (chapter 2), ideally suited to such an application, is employed to evaluate the tension at the drop surface. For each interfacial tension measurement, a minimum of 20 drops are analyzed with the microcantilever technique. The arithmetic average of such measurements for the two standard oils are reported in Table 4.1, where the errors shown are the standard deviations. The present analysis assumes that gravitational forces are negligible. Although the specific gravity of these oils is significantly less than unity (Table 4.1), this assumption holds true due to the small size of the drops involved in this study (recall that $B_o \sim 10^{-5}$ for 10 μm drops).

Oil-in-water emulsions are formed through a high-energy sonification technique. Approximately two milliliters of oil (N190000 or N450000, Cannon Instrument Co.) is placed in a vial with 20 mL of filtered, deionized water. The vial is then agitated in a water bath sonicator (Fischer Scientific, model no. FS6) at ~80°C (in order to reduce the viscosity of the oil phase) for about 1 minute, creating an emulsion of oil drops that are about 5-50 μm in diameter.

4.3.2 Drop shape recovery technique

To perform drop shape recovery experiments, the basic micropipette apparatus is employed and the setup is nearly identical to that of the microcantilever technique (figure 2.2). The only difference being that in drop shape recovery experiments the microcantilever is replaced with a straight micropipette. Temperatures in the apparatus and the laboratory are monitored with a Dual JTEK thermocouple thermometer (Alltemp Sensors) and found to be reasonably constant at 22.5 ± 0.5°C. As the ambient temperature during experiments is noted to be sufficiently stable, no attempt is made to control it in the micropipette experiments. Further details on the basic micropipette setup are found in chapter 2.

In a drop deformation experiment, an individual emulsion drop is captured between two micropipettes, via suction pressure applied at their tips. Then, by retracting one micropipette away from the other using micromanipulators, the drop is axially elongated. Once the drop is sufficiently extended to a maximum axial length L_o, it is released from one of the micropipettes and allowed to dynamically recover to a natural, spherical shape. The axial drop length L is monitored as a function of the recovery time t (which is noted beginning immediately upon release of the drop).

The transient recovery of the extended drop is video-recorded to allow for subsequent analysis. In the analysis of the drop recovery, digitized images are obtained from the videotape using video editing software (Premiere 5.1, Adobe) and a digital video capture card (DC 1000, Pinnacle Systems). Measurements are obtained directly from these images using image analysis software (Sigmascan 5.0, Jandel Scientific). Note that linear dimensions are calibrated through digitized images of a stage micrometer video-recorded under the same magnification. The spatial resolution is estimated to be 0.2 μm. As the frame rate of the video recording equipment is 30 s^{-1}, the temporal resolution is 0.0333 s.

The initial shape profile is obtained from the digitized video image corresponding to $t = 0$. In doing so, the drop contour is documented in less than 50 discrete coordinates. However, as the curvature is derived from second derivatives of spatial coordinates (Appendix D), it is necessary to provide a continuous representation of the drop contour. From this representation, the 181 nodal points that are required as input to the boundary least squares numerical solution can be obtained (Appendix G).

It should be noted that a small volume of the drop fluid exists within the micropipette (this is a consequence of the experimental procedure, as the drop must be mechanically grasped, via suction pressure, in order to deform it). In regards to this, two important points must be discussed concerning the drop length L and the application of the variational approach in this region. First, a consistent reference point must be established before the length L may be defined. This point can be determined by scribing an arc of radius R_d in the rz plane into the orifice of micropipette tip. The reference point lies on this arc at the axis of symmetry ($r = 0$). In practice, this is accomplished by capturing the drop with minimal suction pressure, so that its shape remains spherical, and noting the location at which the captured portion of the drop contour intersects the axis of symmetry. By determining the reference point in this fashion, the final length of an extended drop will be $2R_d$ (i.e., $L/2R_d = 1$) as it returns to a spherical shape. Secondly, at the location where the drop is captured by a micropipette, a fixed boundary is observed (defined by the micropipette tip inner diameter and the fixed volume of drop fluid aspirated in the pipette). In this region, the present variational analysis represents a poor approximation to the experimentally observed rigid geometry. However, since the drop volume contained within the micropipette tip is relatively small compared to the actual drop volume (in all cases less than a few percent), any minor deviations in the numerical analysis may be considered negligible.

4.3.3 Experimental results and discussion

A typical drop recovery process is illustrated in figure 4.6 for a N190000 drop in water. The recovery of such a drop is easily observed through the reduction in the axial length L of the drop as the recovery time t proceeds. Note that the duration of such a shape recovery experiment for a highly viscous fluid is on the order of seconds - much shorter than previous drop evolution experiments (cf. Cohen and Carriere, 1989). The dashed line that extends through all the images represents the reference point (discussed above) for $L(t)$ measurements.

The variational analysis ($\lambda = \infty$) of the drop dynamics for the two viscous oils (N190000 and N450000) tested are compared with the experimental observations. In the numerical simulations, the physical data from Table 4.1 is used. Note that since both the interfacial tension and drop viscosity are defined, the theoretical model is *not* fit to the experimental data. A typical result is shown in figure 4.7 for a N190000 drop in water. This figure clearly shows that the elongation ratio $L/2R_d$ predicted by the present boundary least squares numerical scheme agrees well with the experimental data. It is apparent that the variational model at $\lambda = \infty$ is an excellent approximation for experimental systems in which $\lambda \approx \infty$.

The present variational analysis allows for a detailed solution of the drop shape. It is evident from figure 4.7 that the numerically calculated drop shapes (shown below each photograph) are in excellent agreement with the experimental shapes depicted in the photographs. It is interesting to note that in any deformation experiment, an extended drop always recovers to a sphere, and never breaks up into smaller droplets. This observation agrees with that reported by Stone and Leal (1989a), who demonstrated that

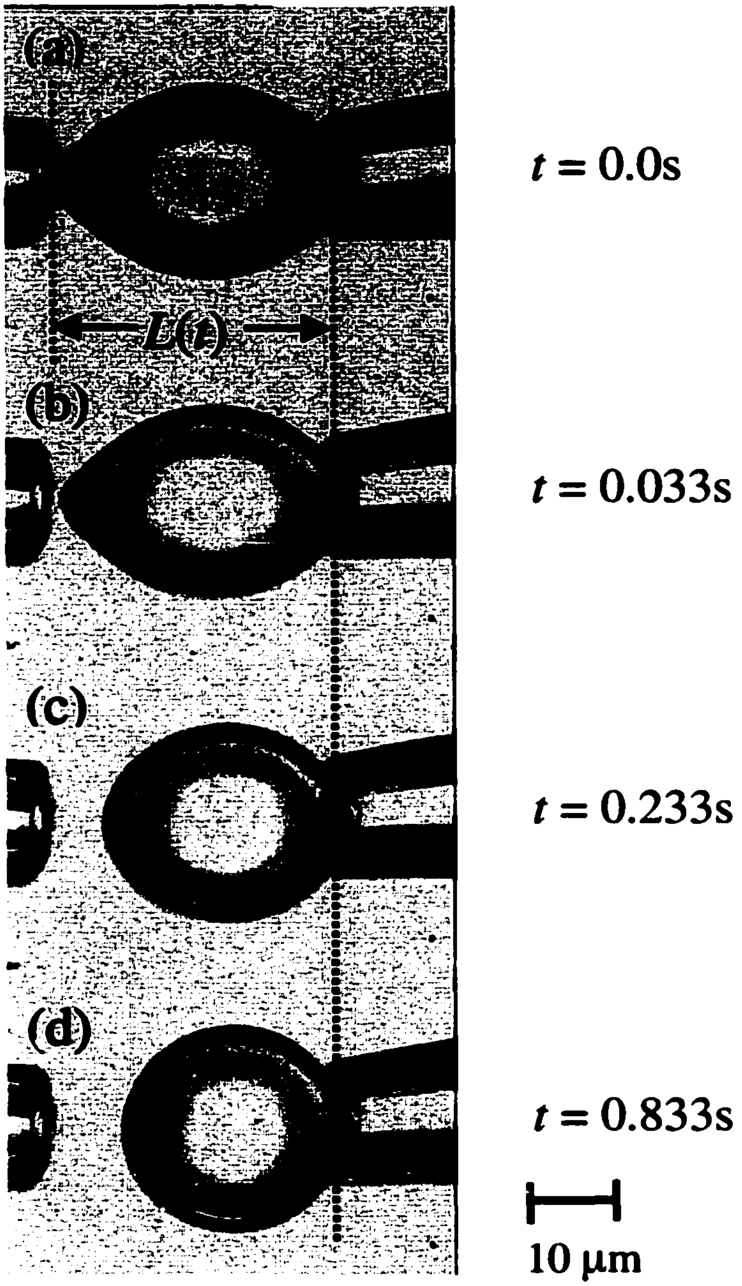

Figure 4.6. Sequential photographs depicting the recovery of an extended emulsion drop in water (22.5°C) following elongation between two micropipettes. In this case, the drop is N190000 Cannon viscosity standard oil. As the extended drop is released from a micropipette, the recovery time t is recorded. The initial drop shape (required for the boundary least squares analysis) is obtained from photograph (a), where $t = 0$s. The axial length of the drop L is measured relative to a reference point denoted by the dashed line extending through all photographs. The dynamic recovery process proceeds (photographs b and c) until the drop attains a final, spherical shape (photograph d).

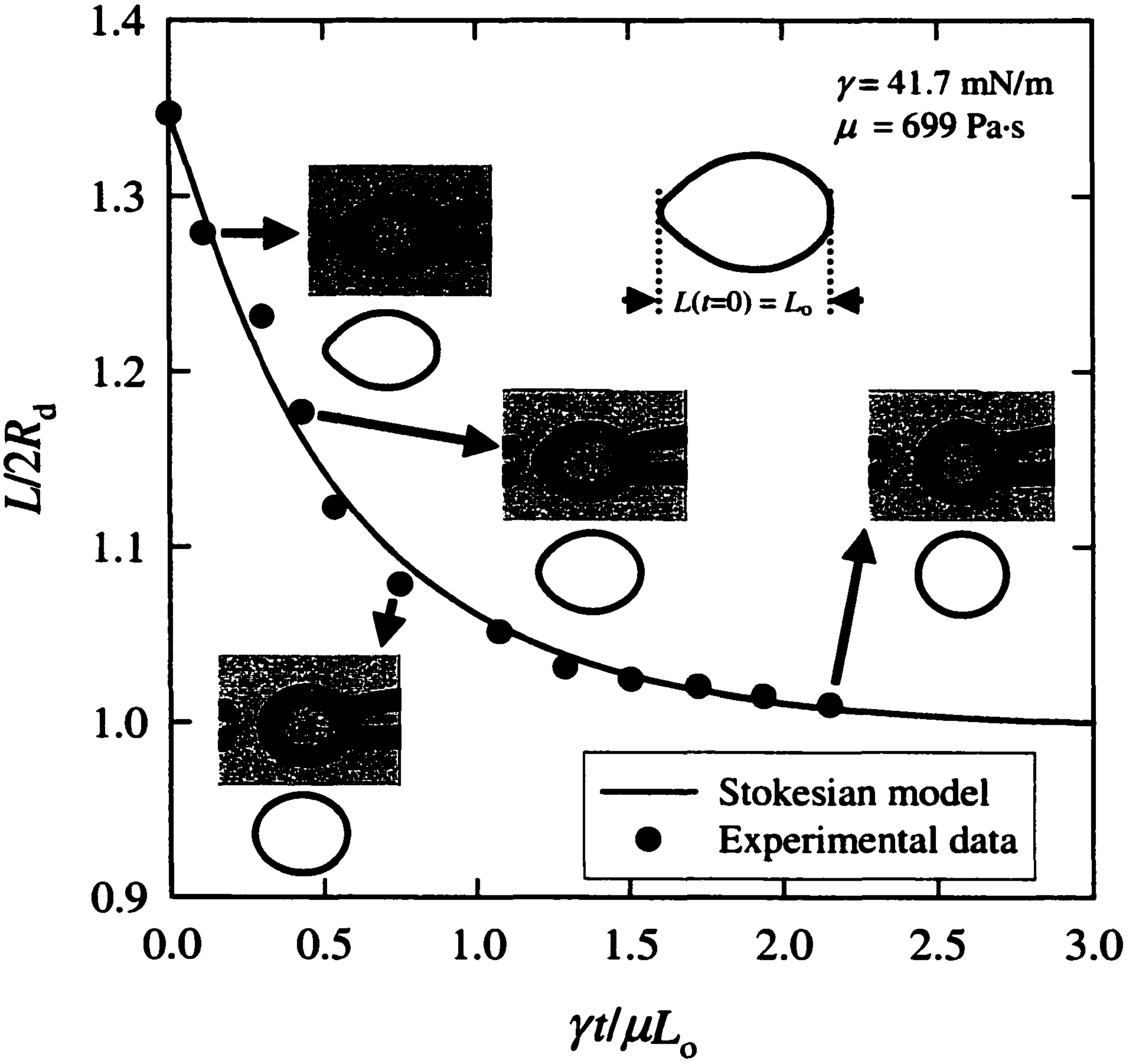

Figure 4.7. Drop dynamics of a highly viscous N190000 drop in water, $\lambda = 7\times10^5$, at 22.5°C. The physical property data is obtained from Table 4.1. The elongation ratio $L/2R_d$ is plotted as a function of dimensionless recovery time $\gamma t/\mu L_o$. The symbols represent experimental drop shape recovery experiment measurements, while the Stokesian model (curve) is solved using the boundary least squares analysis for $\lambda = \infty$. Numerical shape profiles are compared to experimental drop profiles, shown by photographs, at specified times.

as the viscosity ratio λ increases, the elongation ratio required to observe drop breakup becomes exceedingly large ($L/2R_d > 10$ at $\lambda = 10$). In the present experiments, the maximum extension ratio is typically $1.3 \leq L/2R_d \leq 1.5$ and never exceeds 1.6 for $\lambda \approx \infty$. Drop extensions are limited to $L/2R_d < 2$ due to the inner radii of the capillaries (as drop volume is maintained) and the high magnification of the microscope, since most drops are stretched almost across the entire field of view.

4.4 Conclusions

A variational (boundary least squares) technique solving the low Reynolds number shape dynamics of an extended drop in a quiescent fluid is developed. In this approach, it is assumed that the dynamics are driven by a uniform tension γ at the drop surface and rate-limited by the fluid viscosities $\mu, \bar{\mu}$. This technique is valid for all viscosity ratios λ and is most efficient at $\lambda = 0$ and $\lambda = \infty$, addressing limitations to boundary integral procedures that experience numerical difficulties in these regimes. The present variational analysis agrees well with boundary integral calculations at moderate λ's. In addition, the variational approach at $\lambda = \infty$ provides an excellent description for the dynamics of highly viscous ($\lambda \approx \infty$) extended drops that are observed experimentally in drop shape recovery experiments. This simple micromechanical experimentation allows for the elongation (via micropipettes) and recovery of individual emulsion drops. This novel technique offers advantages over traditional drop extension methods in that flow fields are not required to achieve drop deformations.

Chapter 5

Material Properties of Bitumen Drops: An Application of the Drop Shape Recovery Method

5.1 Use of Drop Shape Recovery Technique for Material Property Measurement

The variational analysis introduced in chapter 4 assumes that the shape recovery process of an extended drop is driven by the equilibrium tension at its surface and rate-limited by the Newtonian viscosities of the bulk liquids. In such an analysis, *a priori* knowledge of these material properties is required to describe the relaxation of a drop. However, in the event that one of these properties is unknown, it may be estimated by adjusting a *characteristic velocity* given by γ/μ, such that the experimentally observed relaxation matches the model-predicted shape recovery. Using the variational solution and micropipette techniques, the high viscosity of Athabasca bitumen at room temperature can be measured in regimes where its interfacial tension is well defined. This technique avoids viscous heating effects, which can make accurate measurements of viscosity particularly difficult. Alternatively, the interfacial tension γ of bitumen emulsion drops can be evaluated when the bitumen viscosity μ is known.

5.2 Material and Methods

5.2.1 Emulsion preparation

Emulsions are composed of approximately a few milliliters of coker-feed Athabasca bitumen (Syncrude Canada Ltd.) and 20 mL of an aqueous solution. The emulsification procedure is described in chapter 3. The resulting emulsion drops range from 5 – 30 µm in diameter. Two different aqueous phases are used to simulate the process water in commercial oil sands extraction operations. (These are the same as found in chapter 3 and are reviewed here for clarity.) One of these solutions (SPW) is composed of filtered, deionized water to which the following salts are added (all supplied by Fisher Scientific): NaCl (25 mM), $NaHCO_3$ (15 mM), and Na_2SO_4 (2 mM). The second aqueous phase (DSPW) used in the bitumen-in-water emulsions consists of SPW to which $CaCl_2$ (0.3 mM) and $MgCl_2$ (0.3 mM), also provided by Fischer Scientific, are added. The pH of the aqueous phases is adjusted, as required, with NaOH (Fisher

Scientific) and measured using digital pH probes (model 701A, Orion Research or Accumet AB 15, Fischer Scientific). As only small amounts of base are required to attain the desired pH, the ionic strength of the final solution remained essentially unchanged.

5.2.2 Drop shape recovery experiments

In the drop shape recovery experiments, an emulsion drop is axially stretched between two micropipettes to a maximum extension L_0. The deformed drop is then released from one micropipette and its dynamic behaviour is monitored as it recovers to a sphere. A typical result is shown in figure 5.1, depicting the recovery of an extended bitumen drop in SPW at pH = 9. Recovery times depend on the bitumen drop interfacial tension and vary from ~ one second ($\gamma > 10$ mN/m) to a couple of minutes ($\gamma < 0.1$ mN/m). In the analysis of these experiments, the aim is to measure the axial length of the drop L as a function of recovery time t. Note that the shear rate is not controlled in these experiments. Although the temperature is not controlled in the micropipette apparatus, it is monitored and found to be constant at 22.5 ± 0.5 °C. Further details of this technique and its resolution are provided in chapter 4.

5.2.3 Material property determination

The viscosity μ or interfacial tension γ of the drop is determined by fitting the experimental $L(t)$ data to the theoretical model (chapter 4) using an infinite viscosity ratio $\lambda = \mu / \overline{\mu} = \infty$. This approach is possible since bitumen viscosity is at least of order 10^5 greater than the aqueous phase (Seyer and Gyte, 1989). The fitting of the experimental data is simply made by scaling t/L_0 by a parameter that, when optimized, produces an acceptable fit to the theoretical $L/2R_d$ vs $\gamma t / \mu L_0$ curve. This optimized value is the characteristic velocity γ / μ. Consequently, if only γ / μ is needed, the analysis conducted thus far is sufficient. However, if one of the properties, either γ or μ is known, then the other unknown property can be evaluated from the characteristic velocity. Typical curve fits for bitumen drop recoveries (figure 5.2) give sums of squared errors less than 10^{-3}. It is clear that the *fitted* Stokesian model describes the observed dynamic drop behaviour quite well. In addition, the drop shape profiles predicted by the theoretical model show excellent agreement with the experimental shapes (photographs in figure 5.2).

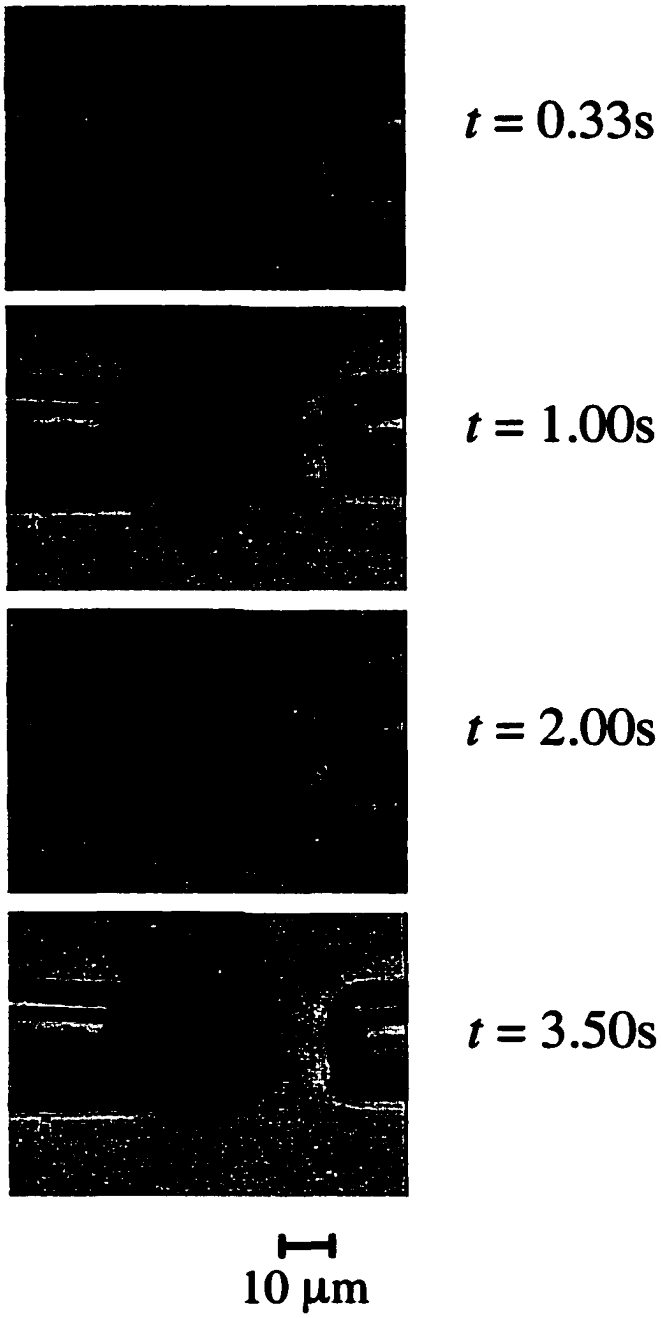

Figure 5.1. Recovery of an extended bitumen drop in SPW (pH = 9) at 22.5°C. The dynamic recovery of such a drop to a spherical shape is measured. The bottom photograph ($t = 3.5$ s) shows the final, time-independent, spherical drop.

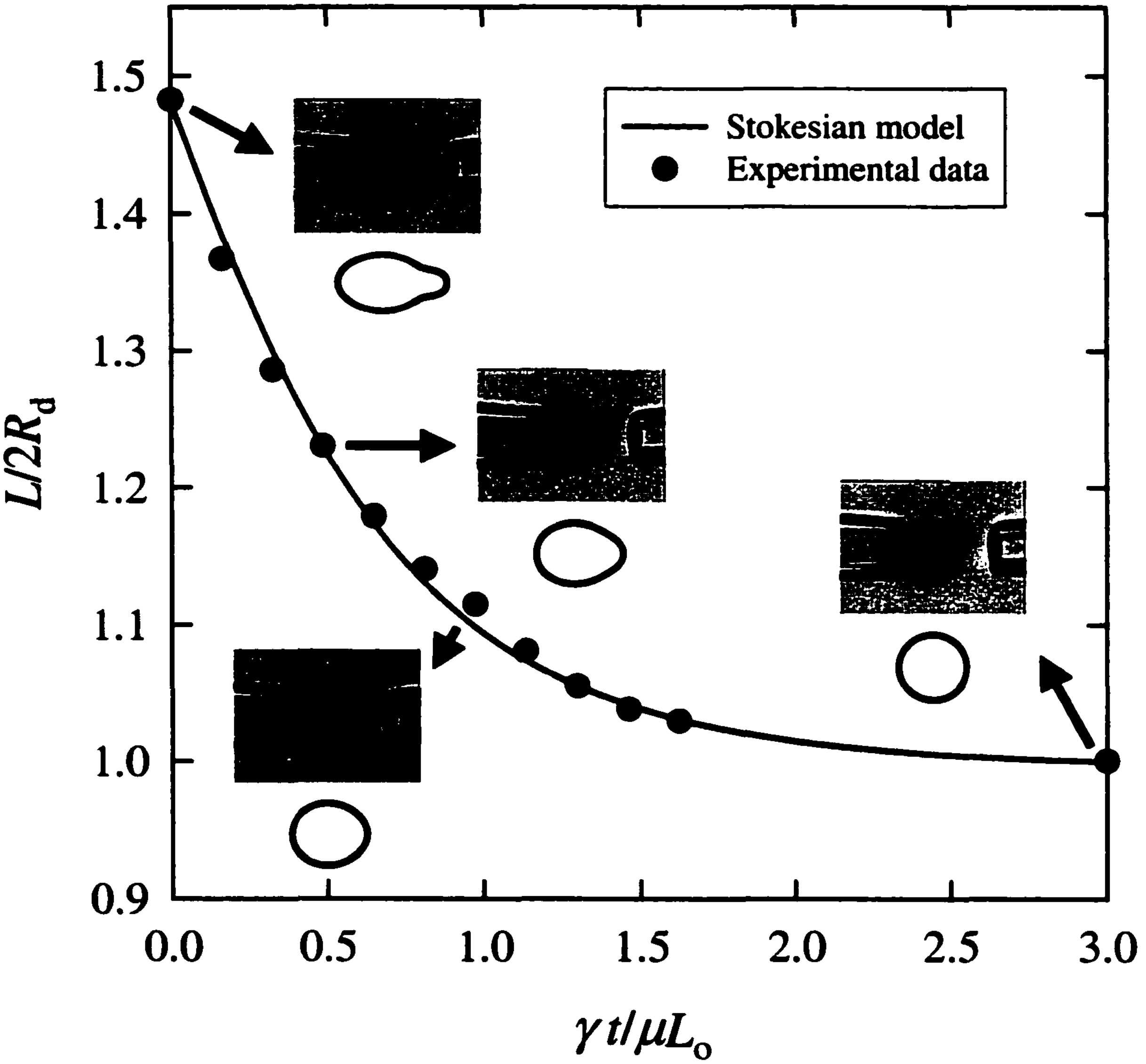

Figure 5.2. Typical fit between experimental bitumen drop recovery data (symbols) and the Stokesian model (solid curve). The extension ratio $L/2R_d$ of an extended bitumen drop recovering in a SPW solution (pH = 10) is monitored as a function of dimensionless time $\gamma t/\mu L_o$. The shape profiles predicted from the Stokesian model are compared to experimental drop profiles (photographs) at specified times. The optimized fitting parameter γ/μ is used to evaluate either the interfacial tension γ or the viscosity μ, assuming that one property is known *a priori*.

5.3 Application: Bitumen Viscosity

Understanding the rheological behaviour of emulsions is important to many applications, such as the transportation of highly viscous oils (Davis, 1988; Nunez et al., 2000). Theoretical models describing such behaviour often require knowledge of the disperse phase viscosity (Taylor, 1932) and surface viscosities at the emulsion interfaces (Oldroyd, 1955; Danov, 2001) in addition to that of the continuous phase. However, in many crude oil-in-water emulsions encountered in the petroleum industry, evaluating the viscosity of highly viscous crude oils may present significant challenges.

Many commercial instruments are available to measure the viscosity of liquids. By far, the most common are those that shear fluids in a tubular geometry (Poiseiulle flow), between a coaxially rotating cylinder and annulus, and in a cone-and-plate type apparatus (Whorlow, 1980). Many of these devices are reported to be able to accurately handle highly viscous liquids (typically up to a maximum of ~ 10^7 Pa·s, with some up to 10^{11} Pa·s!). However, significant errors may result due to viscous heating of a highly viscous fluid, especially at high shear rates (Sukanek and Laurence, 1974; Whorlow, 1980). More recently, viscometers have been introduced to specifically deal with high viscosity materials. A magnetoviscometer, based on Stokes' falling sphere principle, has been developed to measure viscosity up to 10^{10} Pa·s at shear rates ranging from 10^{-6} to 1 s^{-1} (Gahleitner and Sobczak, 1988). This technique, which involves forcing an iron sphere through a viscous fluid via a magnetic field, becomes more complex for opaque fluids in that it requires an induction detection unit. In addition, a viscometer in which an extremely viscous fluid is sheared between two plates has been introduced that measures Newtonian viscosity ranging from 10^8 to 10^{14} Pa·s (Kobayashi et al., 1995). This technique utilizes laser interferometry to detect transient deflections of a sample on the order of 10 nm. A disadvantage associated with these new viscometers is that they may be cumbersome to use, and measurements may take exceedingly long times at high viscosities. In addition, minimum sample volumes of at least milliliters are required. The extremely small samples (~ 10^{-9} mL) that are needed for the present micropipette measurements provide an obvious advantage in the event that only limited quantities of a liquid (i.e., the disperse phase of an emulsion) are available.

Measuring bitumen viscosity proves to be particularly difficult as traditional viscometers tend to become plugged, especially at high temperature and pressure operations (Seyer and Gyte, 1989). Although attempts have been made to modify commercial devices to allow for the determination of bitumen viscosity, viscous heating of several degrees centigrade is noted during typical operation of these modified viscometers (Seyer and Gyte, 1989). Bitumen, at room temperature, is considered to be Newtonian[14] (Ward and Clark, 1950; Dealy, 1979; Schramm and Kwak, 1988).

An alternative approach for determining the viscosity of a highly viscous fluid such as bitumen may be from the shape behaviour of an extended drop in an immiscible liquid. In one such experiment, an initially spherical drop is deformed in a flow field. The flow is then halted and, depending on the extent of deformation, the drop recovers to a sphere or breaks up into a number of smaller droplets (Stone et al., 1986; Stone and Leal, 1989a). In another type of experiment, a polymer fiber may be imbedded within a solid matrix of a second polymer. At elevated temperatures, the polymers melt and the imbedded polymer (now an extended fluid drop) dynamically evolves (Cohen and Carriere, 1989). In these dynamic processes, the interfacial tension drives a drop evolution that is rate-limited by the viscosities of the two fluid phases. In such studies, due to the scale and type of experiment, typical recovery times ranged from several hundred seconds to hours for highly viscous ($\sim 10^2 - 10^3$ Pa·s) systems of moderate interfacial tension ($\gamma > 1$ mN/m). The very short recovery times of several seconds observed in the micropipette shape recovery technique (cf. figure 4.6) provide a clear advantage that is exploited for high viscosity measurements.

5.3.1 Viscosity measurement

Using procedures described in section 5.2.3, the viscosity of bitumen drops is evaluated at pH values ranging from $8 < \text{pH} < 10.5$ (figure 5.3). Each data point represents the average of at least 10 individual viscosity measurements. Recall that, in this viscosity measurement, a characteristic velocity γ / μ is optimized by fitting the experimental data to the theoretical model. Since the bitumen-water interfacial tension is

---

[14] Some rheological experiments with Athabasca bitumen have suggested that it may be slightly non-Newtonian (Dealy, 1979). However, the deviations from Newtonian behaviour indicated a thixotropic or pseudoplastic behaviour and may be consistent with viscous heating of this fluid.

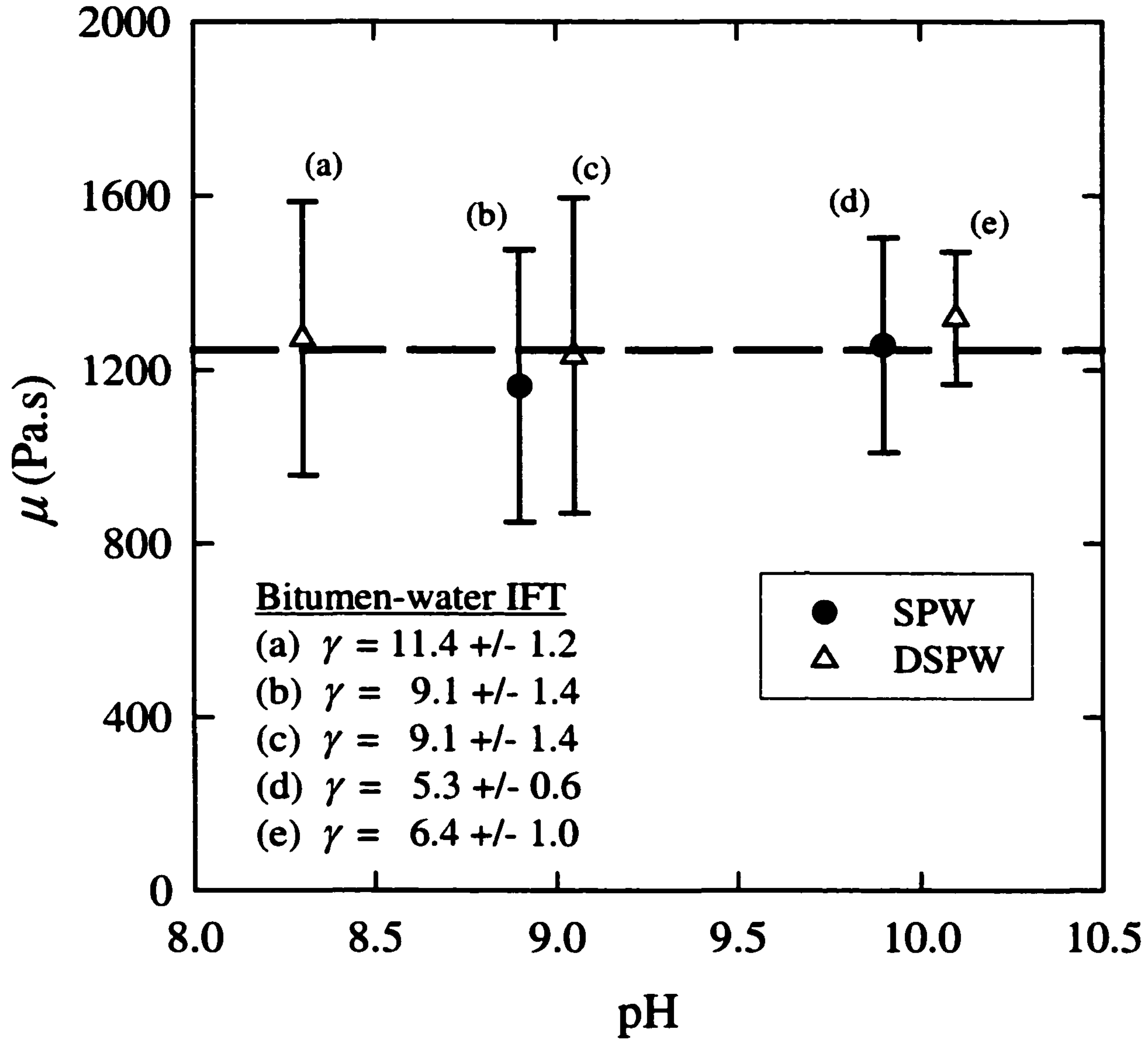

Figure 5.3. Viscosity μ of bitumen at 22.5°C via the drop shape recovery technique. Each data point represents the average of 10 individual measurements with bitumen drops in SPW (solid circles) and DSPW (open triangles) aqueous phases; the error bars give the standard deviation. The average and standard deviation of bitumen viscosity at this temperature is 1246 ± 332 Pa·s (broken line). The bitumen-water interfacial tension γ for each pH condition, as determined by the microcantilever technique (chapter 3; figure 3.5), is indicated in the figure and used to evaluate μ.

already known (via the microcantilever technique) for the pH range of interest (figure 3.5; Moran et al., 2000), the viscosity is easily calculated from the optimized characteristic velocity. In such a procedure, the initial drop shape must also be known *a priori* and is obtained from video images. As expected, the viscosity of bitumen does not depend on the pH of the surrounding aqueous phase. It is noted that the viscosity calculated by the drop shape recovery technique is unchanged even though the bitumen-water interfacial tension decreases by a factor of two as the alkalinity of the aqueous phase is increased from pH = 8 to pH = 10. The viscosity of bitumen is 1246 ± 332 Pa·s, with the error representing the standard deviation of all measurements.

The bitumen viscosity obtained with the drop shape recovery technique agrees in general with that of previous studies (Seyer and Gyte, 1989); however, it resides at the upper limit of the reported range. This may be due to the fact that viscous heating is completely negligible in the present technique, as discussed below. Recall that previous viscometric studies employed commercial devices (or adaptations thereof) to evaluate bitumen viscosity and viscous heating may have caused erroneous, lower viscosity measurements[15] (Seyer and Gyte, 1989). Even though the standard deviation reported in this study may seem large (~25%), the consistency of the measured viscosity throughout the range of conditions provides merits for the reliability of the measurements. Despite the heterogeneity in the composition of bitumen (Mitchell and Speight, 1979; Prowse et al., 1983), it is likely that these errors would be reduced somewhat if temperature control (say, to ± 0.1°C) was enabled in the micropipette apparatus.

5.3.2 Viscous heating

The occurrence of viscous heating within a viscometer can become significant at high shear rates for many fluids. This phenomenon is greatly pronounced for highly viscous fluids as the energy dissipated during shearing is a function of the fluid viscosity. As such, the viscosity of these fluids can only be accurately determined as a function of temperature in commercial viscometers that operate at very low shear rates and that are equipped with excellent temperature control devices (Whorlow, 1980). The novel technique introduced in this study exhibits no viscous heating despite the fact that the

---

[15] The viscosity of bitumen is known to be highly temperature sensitive (Seyer and Gyte, 1989).

shear rate is not controlled (but shown to be reasonably low) and the temperature is only monitored. This will be demonstrated for an extended bitumen drop recovering in a micropipette shape recovery experiment.

The energy per unit volume E dissipated during the shearing of a bitumen drop may be approximated by (Bird et al., 1960)

$$E = \mu\left(\frac{\mathrm{d}L}{\mathrm{d}t}\cdot\frac{1}{2R_\mathrm{d}}\right)^2\cdot t\,, \tag{5.1}$$

where the term in brackets is the shear rate and t is the time required for an extended drop to recover to a sphere. In the present study, the shear rate varies from a maximum when the drop is at its maximum elongation L_0 to zero as the drop reaches its equilibrium spherical shape. Analysis of typical recovery data suggests that the maximum shear rate (for a ~20 μm drop) ranges from about 0.1~1 s^{-1} (cf. figure 5.2). Assuming a viscosity of 10^3 Pa·s and a recovery time on the order of a second (cf. figure 5.1), a conservative estimate of the energy dissipated in a recovery experiment is $E \approx 1000\ \mathrm{J/m^3}$.

The temperature rise ΔT can be estimated from the energy dissipated by

$$\Delta T = \left(\frac{E}{\rho C_p}\right), \tag{5.2}$$

in which ρ is the density and C_p is the specific heat capacity of the drop liquid. For Athabasca bitumen, with $\rho \approx 1000\ \mathrm{kg/m^3}$ (Shaw et al., 1996) and $C_\mathrm{p} \approx 1800$ J/kgK (Smith-Magowan et al., 1982; Cassis et al., 1985) at room temperature, the temperature rise during a drop recovery experiment is $\Delta T \approx 5\times10^{-4}$ K. Clearly, viscous heating is negligible during such experiments[16].

5.4 Application: Bitumen-Water Interfacial Tension in Alkaline Environments

Determining the interfacial tension between density-matched systems is a considerable challenge. For such systems, the measurement of interfacial tension is rendered impossible with traditional tensiometers when at least one of the phases is

---

[16] To be sure, one may consider the Brinkman number $Br = (\mu\cdot[\mathrm{d}L/\mathrm{d}t]^2)/(k_\mathrm{T}\Delta T)$, that compares the rate of heat dissipation to that at which heat is conducted from the drop during its recovery. For bitumen, with a thermal conductivity $k_\mathrm{T} \approx 1.2$ W/mK (Karim and Hanafi, 1981), $Br \approx 10^{-4}$.

highly viscous (Moran et al., 2000). This is true for tensiometric techniques that are designed for measuring low interfacial tensions (Wilson and Bradner, 1977; Satherley et al., 1989; Lin and Hwang, 1994). Shape-based techniques, such as the spinning and sessile drop methods, rely on body forces to deform drops. In these methods, measures of drop shape deviations from spherical geometries are used to infer tensions. In the absence of such forces (i.e., in density-matched systems where gravity forces are negligible) drops will not deform, rendering these techniques ineffective. Light scattering techniques (Jon et al., 1986), which measure thermal perturbations at an interface to calculate tensions, may appear exempt from difficulties arising with density-matched systems. However, in the event of highly viscous fluids, these perturbations may become damped, limiting these methods to systems of lower viscosity.

Although common methods of tensiometry are limited from systems involving highly viscous and density-matched fluids, less recognized techniques appear better suited to such systems. Perhaps one of the first applications of Taylor's elegant small drop deformation theory was the estimation of interfacial tension (Taylor, 1932, 1934). This theory assumed that small drop deformations were linearly proportional to the shear rate as a drop was deformed in steady shearing flows. In this model, the constant of proportionality was defined by a uniform interfacial tension. In his work, Taylor (1934) estimated the interfacial tension of moderately viscous "tar pitch mixture" drops ($\mu = 200$ Pa·s) in "golden syrup". More recently, small deformation theory has been used to calculate interfacial tensions of several nearly density-matched systems (Bentley and Leal, 1986). However, this theory is limited to small deformations and its linear approximations may introduce errors into interfacial tension calculations.

Shape relaxation methods have been used to calculate interfacial tensions of viscous drops in immiscible quiescent fluids and appear to be ideally suited to density-matched liquids. In systems where the viscosities are known, interfacial tensions have been estimated from characteristic times for recovery or break up (Carriere et al., 1989; Elemans et al., 1990; Watkins and Hobbs; 1993; Tjahjadi et al, 1994; Cho et al., 1996; Luciani et al., 1996; Son, 2001). In particular, the shape dynamics of millimeter-sized drops in polymer melt systems (e.g., polystyrene in polymethyl methacrylate) was monitored and the interfacial tension measured, using a limited one-dimensional model, to be on the order of 1 mN/m (Carriere et al., 1989). This method experienced significant errors of ± 26% in the calculations and the measurements agreed with literature values to within ± 20%. The large magnitudes of these errors were attributed to the simple nature of the model used. Due to the size of the drops and the viscosities of the polymers ($\mu \sim 2 - 20$ Pa·s at 190°C), the relaxation times were on the order of hours! The length scale of these experiments appears to limit this procedure to lower viscosity fluids. (Very high viscosity fluids ($\mu \sim 10^6$ Pa·s) may be studied with the micropipette apparatus since relaxation times are on the order of seconds; figure 5.1). Improved boundary integral descriptions of the drop relaxation process have been applied to measure interfacial tensions of the polymer melt systems discussed above (Tjahjadi et al., 1994). However, even though the transient drop shape relaxation of an extended drop is *nonlinear* (cf. figure 5.2), interfacial tensions were estimated from *linear* measures of the drop dynamics.

Bitumen is a highly viscous ($\mu \approx 1250$ Pa·s at 22.5°C; see figure 5.3) heavy crude oil with a density nearly-matched to that of water. It has been established that, for optimal recovery of bitumen from oil sands, alkaline conditions are required in water-based extraction processes (Shaw et al., 1996). In such commercial processes, the interfacial tension between water and bitumen is extremely important (Sanford and Seyer, 1979). The interfacial tension of bitumen drops in aqueous solutions of pH = 2 - 11 was measured using the microcantilever technique (Moran et al., 2000). However, at pH > 11, the interfacial tension was below the detection limit of this apparatus ($\gamma \approx 1$ mN/m). In this study, the low interfacial tension of bitumen drops in alkaline SPW solutions is established using the drop shape recovery technique and the Stokesian model (chapter 4).

5.4.1 Bitumen-water IFT measurement in alkaline regimes

To evaluate low interfacial tensions, drop shape experiments are performed on bitumen drops over a pH range from 10 to 12.5 and the $L(t)$ data fit to the variational model (chapter 4). Within this pH range, such drop recovery processes have typical recovery times t of orders ranging from a second to a minute. Recall that, in the drop shape recovery technique, the interfacial tension γ can be calculated from an optimized characteristic velocity γ/μ, assuming that the viscosity μ is defined (see section 5.2.3).

The viscosity of bitumen is known (μ = 1246 Pa·s), as it was evaluated from shape recovery experiments at lower pH regimes (section 5.3.1; figure 5.3); in these regimes, the tension was measured with the microcantilever technique (figure 3.5). The initial drop shape is obtained from video images.

The interfacial tension of the bitumen drops is highly dependent on the pH of the simulated process water (SPW) that surrounds them (figure 5.4). As the pH is increased, the interfacial tension decreases and falls below γ = 1 mN/m at pH > 11. The inset in figure 5.4 shows the low tensions measured with the drop shape recovery technique at high pH in a logarithmic scale to clearly show such a trend. The microcantilever technique was used to evaluate interfacial tensions for the same system over a pH range $2 \leq \text{pH} \leq 11$ (Moran et al., 2000; chapter 3) and some of these measurements ($9 \leq \text{pH} \leq 11$) are also shown in figure 5.4 (open symbols) for comparison. Both the microcantilever and drop shape recovery techniques give similar results. It is evident that this novel shape recovery technique is useful in measuring low interfacial tensions (γ< 1 mN/m) of density-matched and highly viscous systems.

Similar trends for bitumen-water interfacial tension in alkaline environments have been noted by many researchers (Isaacs and Smolek, 1983; Drelich and Miller, 1994; Drelich et al., 1995; Basu et al., 1996; Moran et al., 2000). This phenomenon has been attributed to the pH-dependent release of naturally occurring surfactants found within the bitumen (Schramm et al., 1984; Drelich and Miller, 1994).

5.5 Conclusions

A novel micromechanical technique is developed to evaluate the material properties of emulsion drops. In this technique, the time-dependent recovery of deformed emulsion drops, axially elongated via micron-sized suction pipettes, is fitted to a simple model. This model assumes drop recovery is driven by the interfacial tension and rate limited by the viscosity of the drop. The technique offers advantages over traditional viscometers as viscous heating is negligible, only extremely small samples (~10^{-9} mL) are required and a short time-scale for experiments is therefore possible. At room temperature, the high viscosity of bitumen and its low interfacial tension with alkaline environments are evaluated.

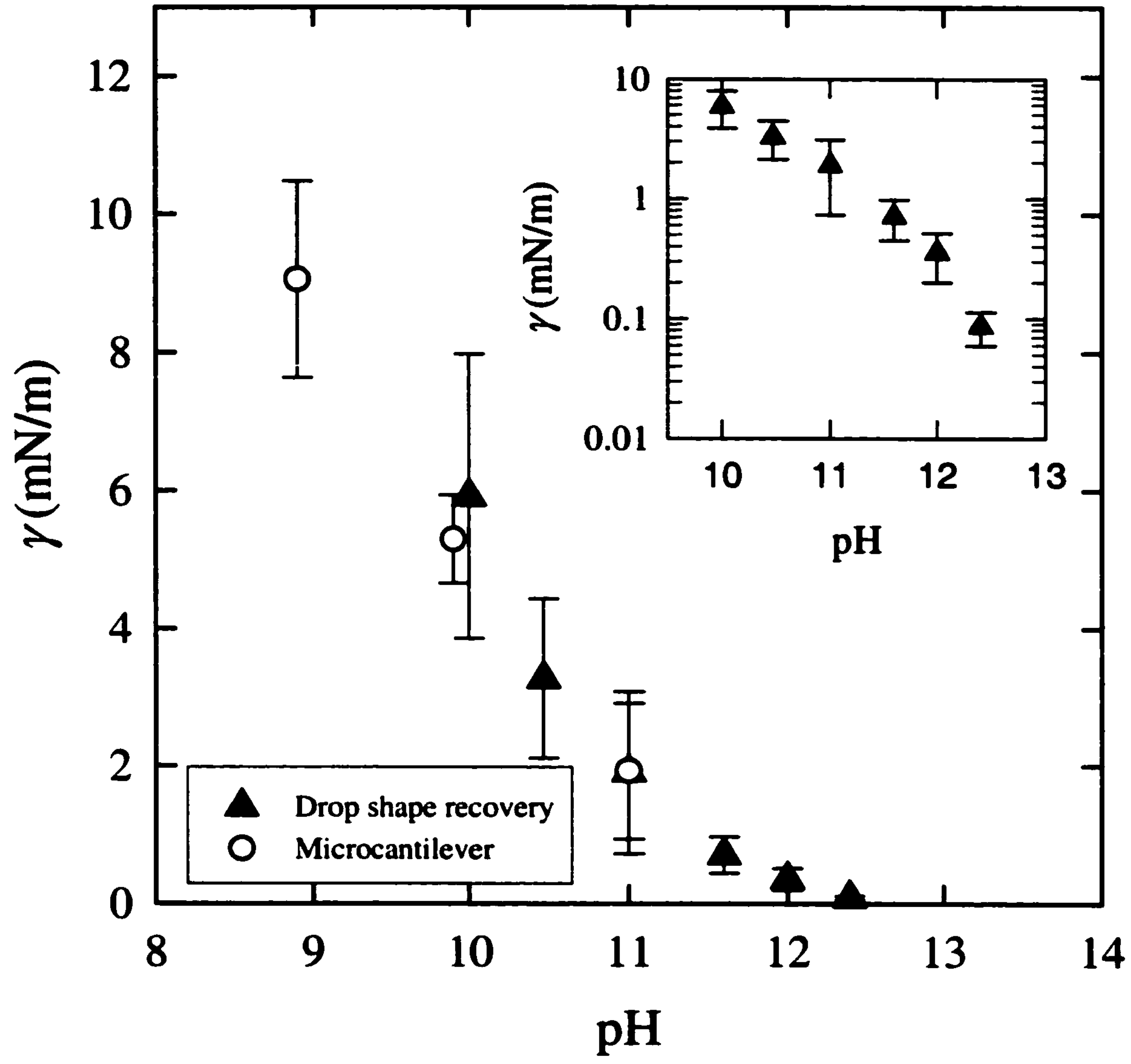

Figure 5.4. Interfacial tension γ of bitumen with water (SPW) in alkaline regimes (22.5°C). Tensions are determined using the drop shape recovery technique (solid triangles) and the microcantilever tensiometer (open circles; see chapter 3). For each data point, a minimum of 10 drops are analyzed, (a minimum of 10 $L(t)$ measurements are obtained for each drop), with the error bars giving the standard deviation. In the highly alkaline regimes (pH > 11), the tensions are below the detection limit of the microcantilever method. In these regimes, the drop shape recovery technique is sensitive enough to evaluate quite low interfacial tensions ($\gamma < 1$ mN/m). The inset recasts the drop shape recovery interfacial tension measurements on a log scale for better resolution at high pH values. For shape recovery experiments, bitumen viscosity is taken as 1246 Pa·s (from figure 5.3).

Chapter 6

Surface Plasticity of Bitumen Drops

6.1 Introduction

Novel micromechanical techniques have been developed to quantify the static and dynamic behaviours of emulsion drops (chapters 2 to 5). In these analyses, it is assumed that the equilibrium properties of the *simple* drops are dictated entirely by the interfacial tension, while any dissipative behaviour is provided by the Newtonian viscosities of the bulk phases. However, the emulsion drops in many systems, such as some found in the petroleum industry, may exhibit more complex behaviours. In this chapter, with application to bitumen (a heavy crude oil) emulsions, micromechanical techniques are extended to explore more complex rheological behaviours of emulsion drops, including some irreversible surface phenomena.

Crude oil-water emulsions present considerable challenges to the petroleum industry. To date, the primary research focus has been on the elimination of water-in-crude oil emulsions; these are emulsions naturally found in reservoirs or are the result of various extraction or cleaning processes (Graham, 1988)[17]. The remarkable stability of these emulsions has been attributed to the formation of a "skin" at the oil-water interface (Bartell and Niederhauser, 1949; Reisberg and Doscher, 1956).

There is still considerable debate as to the composition of the "skin" at crude oil-water interfaces, and numerous studies have attempted to characterize their rheological properties. Of these are studies concerned with the interfacial tension (Strassner, 1966; Pasquarelli and Wasan, 1981) and interfacial shear viscosity (Dodd, 1960; Cairns et al, 1976). Surface pressure data of some crude oil-water interfaces appears to suggest formation of a "rigid" structure exhibiting increased shear viscosities at high compressions (Kimbler et al., 1966; Neustadter et al., 1975; Brown et al., 1977). In addition, interfacial viscoelastic behaviours have also been demonstrated through creep

---

[17] The removal of water from these systems is desired for a number of reasons. For example, as the water contains dissolved salts, its removal will reduce corrosion of equipment.

compliance tests (Jones et al., 1978) and are described by Maxwell-Voight type models (Mohammed et al., 1993, 1994). The mechanical properties of crude oil-water interfaces show considerable variation depending on the crude source. It has been suggested that emulsion stability is most affected by interfacial dilational properties (Neustadter et al., 1981; Mukherjee and Kushnick, 1989; Kim et al., 1995) and the interfacial activity of demulsifiers (Krawczyk et al., 1991; Bhardwaj and Hartland, 1994).

Rheological studies of crude oil-water interfaces have typically been conducted on length scales of millimeters or larger, with devices such as the Du Noüy ring or biconical bob surface viscometer. Parameters observed at these length scales are then assumed to be equivalent to those of micron-scale emulsion systems. However, it was recently demonstrated that such an extrapolation may not be valid for interfacial tensions of emulsion systems (including water-in-crude oil emulsions) due to, among other factors, vastly differing surface area-to-volume ratios (Yeung et al., 1998). It is then reasonable to suggest that similar extrapolations of other surface mechanical properties may be questionable. To address this issue, a micron-scale technique has recently been introduced with which the surface mechanical properties of individual emulsion drops may be studied (using micropipettes). This novel technique has allowed for the measurement of interfacial tensions and surface viscosities of water drops in diluted bitumen[18] at the micron-scale (Yeung et al., 1999). The most notable finding from these studies is the strong dependence of surface rheological properties on the bitumen dilution ratio. At high bitumen dilutions, rigid surface skins were seen, while at low dilutions the interface appeared fluid and a novel emulsification mechanism was observed (see also Dabros et al., 1999).

Of present interest is the bitumen-in-water emulsions encountered in the oil sands industry. In this study, bitumen mined from the Athabasca oil sands (Northern Alberta, Canada) is considered. Athabasca bitumen is a highly viscous Newtonian fluid (Schramm and Kwak, 1988; see also chapter 5) that has a density almost equal to that of water (Liu, 1989; Basu et al., 1996; Shaw et al., 1996). In commercial water-based extraction processes, the oil sands (containing about 10 wt% bitumen) is mixed with

---

[18] Bitumen is a highly viscous fluid (Shaw et al., 1996; also see chapter 5). In order to achieve workable viscosities at room temperatures, bitumen must be mixed with an organic solvent.

water, air and a small amount of caustics in the digestion stage. Here, the bitumen is liberated from the sand particles to exist as aerated oil drops in an aqueous slurry containing dissolved salts, coarse sand particles and fine clays (such as montmorillonite and kaolinite; Shaw et al., 1996). The oil sand slurry contains a large number of bitumen drops that are less than 40μm in diameter, and they represent the difficult-to-recover portion of the total recoverable hydrocarbon.

In water-based bitumen extraction, it is advantageous to promote the coalescence of the small bitumen drops within the slurry (i.e., break the bitumen-in-water emulsion) in order to improve oil recovery. Clearly, this coalescence phenomenon is a function of the surface properties of the emulsion drops. In particular, coalescence may be dictated by the mechanical deformability of the drop surfaces (Walstra, 1993; Lam et al., 1995). Recent bench-scale studies have suggested that the recovery of bitumen in water-based extraction is severely reduced when the aqueous phase contains both montmorillonite clays and calcium ions (Kasongo et al., 2000). This is attributed to a suspected synergistic effect between these two species that promotes the coating of bitumen drops with the clay fines. An examination of bitumen drop surface properties in this environment may provide insights into the cause of the poor recovery noted above.

Some of the original micropipette techniques of Yeung and coworkers (1998, 1999) cannot be applied to bitumen-in-water emulsion systems due to the highly viscous nature of bitumen at room temperatures. (In fact, it is likely that all traditional surface rheological instruments are inapplicable to fluids that are as viscous as bitumen; Kim et al., 1995). Adaptation of the micropipette techniques to address such limitations has enabled evaluation of interfacial tensions through micron-scale stress-strain experiments (Moran et al., 1999; see chapter 2) and drop shape recoveries (see chapter 4). Using such techniques, the interfacial tensions of bitumen drops in aqueous media were obtained as a function of pH (Moran et al., 2000; see chapters 3 and 5). These *in situ* micro-mechanical techniques are unique in their applicability to emulsion systems that are density-matched and involve highly viscous fluids.

In this chapter, the mechanical behaviour of bitumen drops in different aqueous environments is studied by further adapting the micropipette techniques (chapters 2 and 4). In particular, the effect of montmorillonite clays and calcium ions on the surface behaviour of bitumen drops is examined. (As noted above, this environment is expected to severely reduce the recovery of bitumen from oil sands in water-based extraction processes; Kasongo et al., 2000.) The surface plasticity and other surface properties of bitumen drops in such an aqueous environment are discussed. A simple, lumped-parameter model is developed to describe the dynamics of bitumen drops as they recover from perturbed geometries.

6.2 Materials and Methods

6.2.1 Emulsion preparation

Bitumen-in-water emulsions are created, according to procedures described in chapter 3, in three different aqueous environments:

a) Filtered, deionized water (DIW).

b) DIW to which 0.1 wt% of montmorillonite clays (M) are added prior to emulsion formation. This aqueous suspension will be referred to as the DIW + M system. The montmorillonite clays (Ward's Natural Science Est.) originated from Panther Creek, Colorado and are used as supplied.

c) DIW to which 0.1 wt% of montmorillonite clays (M) and 50 ppm of calcium ions (Ca^{++}), provided as $CaCl_2$ (Fisher Scientific), are added prior to emulsification. This aqueous suspension will be referred to as the DIW + M + Ca^{++} system. The calcium ion concentration used in this study is chosen to reflect that required to drastically decrease bitumen recovery in bench-scale hot water extraction processes (Kasongo et al., 2000).

The aqueous phase pH is measured using a digital pH probe (Accumet Basic AB 15, Fisher Scientific). The suspensions are filtered with a 0.45 μm filter prior to pH evaluation.

Although the hydrophobicity of the montmorillonite clay is not evaluated, it is assumed that the clay particles are largely hydrophilic in nature (Yan and Masliyah, 1994). A particle size distribution analysis indicates that, while the modal particle size is 2-3 microns in equivalent diameter, a significant fraction (21.1%) of the montmorillonite particles are less than 1 micron in equivalent diameter. For such measurements, the montmorillonite particle suspension is created by sonification with a 600 watt ultrasonic probe (Sonics & Materials) for 3 minutes. The particle size analysis is conducted via a laser diffraction device (Coulter LS130). It is suggested that this technique may overestimate the size of clay platelets (Cowles, 2000).

6.2.2 The micropipette experimental set-up

The micropipette apparatus allows for the study of general mechanical behaviours of individual emulsion drops. Two techniques, the microcantilever and drop shape recovery, are implemented. Further details may be found in chapters 2 and 4. All experiments are conducted at room temperatures (22-23°C) within one hour of emulsion formation.

6.2.3 Stress-strain experiments (microcantilever technique)

Static stress-strain experiments are performed on individual emulsion drops in different aqueous environments. For simple (Newtonian) emulsion drops, any static resistance to deformation from a sphere is provided by the interfacial tension of the drop, which acts to minimize its surface area (i.e., to obtain a spherical configuration). As documented in chapter 2, a micromanipulator is used to stretch an individual drop, between a micropipette and a force-measuring cantilever, to a series of equilibrium shapes. Since a force is applied in increasing increments this is referred to as the *loading* stage of the experiment. Here, the microcantilever technique is extended to include an *unloading* stage (this phase of experimentation was not explored in previous chapters). Once the desired maximum drop elongation is achieved, the applied force is removed in incremental steps by moving the micropipette towards the microcantilever. This is the unloading stage, as the axial load is incrementally reduced. Drops are held in each new stretched position for 10 seconds to allow for diffusion[19] of species to the drop surface and for any viscous relaxation (see chapter 3) to occur.

---

[19] The time required for diffusion of a montmorillonite aggregate through an aqueous phase to a bitumen drop surface is estimated from the Einstein-Smoluchowski equation $t = x^2/2D$, where x is the diffusion path length and D is the diffusion coefficient. The diffusion coefficient is estimated by $D = kT/6\pi R_a\mu$, where k is the Boltzmann constant, T is temperature, and R_a is the aggregate size (Hunter, 1986). Assuming $R_a \sim 10$ nm (an aggregate of 10 montmorillonite particles), $x \sim 20$ μm (i.e., the bitumen drop "sees" this distance into the aqueous phase from its surface) and $\mu = 1250$ Pa·s (chapter 5) one arrives at $D \sim 10^{-11}$ m^2/s and $t =$ 10 s.

As noted in previous chapters, the loading stage of the microcantilever experiment can be applied to measure the interfacial tensions of emulsion drops (see chapter 2). The stiffness of the microcantilever is calculated from linear beam theory (Appendix C) and is calibrated by measuring the interfacial tension of known systems.

6.2.4 Drop shape recovery experiments

These experiments are designed to study the dynamic (time-dependent) recovery of a deformed emulsion drop. In this technique, a drop is axially stretched between two micropipettes, to a maximum length L_o, then released and allowed to recover to a final shape, defined by a length L_f that does not vary with time. The technique is described in detail in chapter 4. Prior to its release, the drop is maintained in its stretched configuration for 10 seconds (for the same reasons as mentioned above). The recovery is noted from the time at which the drop is released. The time-dependent axial length of the drop is measured from a fixed reference point (chapter 4). As such, an extended drop that recovers to a sphere will have a final length equal to the drop diameter, $L_f = 2R_d$, where R_d is the radius of the spherical drop.

Drop shape recovery experiments are used to calculate interfacial tensions of simple emulsion drops (see chapter 5) by fitting the experimental data to a theoretical model based on Stokes flow (chapter 4). For these simple emulsion drops, the recovery process is rate-limited by the bulk viscosity of the bitumen, while the interfacial tension tends to drive the drop to a minimum area configuration. This Stokesian model is not applicable to emulsion drops exhibiting complex behaviour; i.e., drops that do not recover to spherical final shapes. (Other forces may be involved and are discussed below.)

6.3 Results and Discussion

6.3.1 Emulsion and drop behaviour descriptions

Bitumen-in-water emulsions are prepared as described above and subsequently viewed under magnification. It is noted that bitumen drops emulsified in an aqueous phase of deionized water (DIW) or an aqueous suspension of montmorillonite clays (DIW + M) are always spherical in nature. This result is expected since the drops are nearly micron-sized. Assuming that these bitumen drops are simple (see above) and have non-zero interfacial tensions, they will be spherical as the capillary forces are significantly larger than the body forces. This is made apparent through the Bond number $B_o = \Delta\rho g R_d^2/\gamma$, where $\Delta\rho$ is the density difference between the two immiscible phases and g is the gravitational acceleration[20].

By contrast, bitumen drops emulsified in slurries containing montmorillonite clays and calcium ions (DIW + M + Ca^{++}) exhibit markedly different behaviour. Although the majority of drops are spherical, a significant number are observed to be highly non-spherical in appearance (figure 6.1), and may possess sharp "horns". If such bitumen drops are mechanically deformed (i.e., stretched between micropipettes) they typically show minimal recovery to their initial non-spherical shape. Considering that bitumen is a Newtonian fluid, it is clear that some unusual mechanical phenomena must be occurring at the surfaces of these drops. In this chapter, as a first attempt to examine the surface rheology of such systems, only *bitumen drops that are initially spherical are examined.*

It is helpful to classify the behaviours of bitumen drops in response to mechanical deformation. Note that since bitumen is a Newtonian liquid, these behaviours are attributed to the drop surface (proof of this is given in a following section). The following three types of behaviours are discussed:

(a) *Ideal behaviour*: bitumen emulsion drops recovering to natural spherical shapes upon removal of a deforming force (applied via micropipettes). This behaviour is expected for simple emulsion drops and is the only behaviour that has been noted thus far in this thesis (chapters 2-5)

(b) *Plastic behaviour*: mechanically deformed bitumen drops showing partial recovery from a state of maximum deformation, but do not fully recover to a natural spherical geometry

(c) *Perfectly plastic behaviour*: initially spherical bitumen drops remaining in a deformed state upon removal of applied forces with no evidence of recovery.

---

[20] For a typical bitumen-in-water emulsion of 10 μm drops $B_o \sim 10^{-6}$, indicating that surface tension forces (that drive drops to minimum area spherical configurations) dominate over gravitational forces (that act to deform drops to non-spherical geometries).

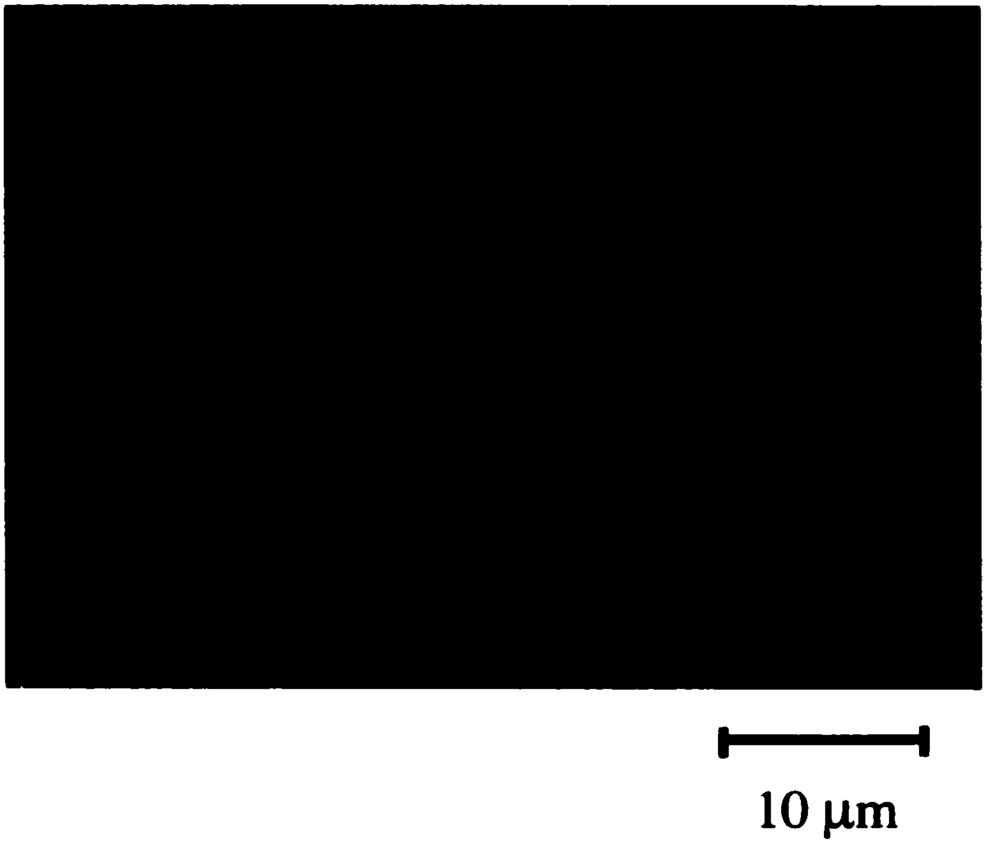

Figure 6.1. Photograph of a highly non-spherical bitumen emulsion drop in an aqueous environment of 0.1 % (by weight) montmorillonite clays and 50 ppm of calcium ions (DIW + M + Ca^{++}). In the DIW + M + Ca^{++} suspension, although the majority of drops are naturally spherical, a significant number are as depicted in this photograph. All experiments are conducted on initially spherical bitumen drops.

6.3.2 Interfacial tensions

The interfacial tensions γ of bitumen drops in the three aqueous environments are determined using the two different micropipette techniques (Table 6.1). The microcantilever technique is a static method where the equilibrium force required to achieve a specific drop deformation is evaluated (Moran et al., 1999, 2000; see also chapters 2 and 3). The drop shape recovery technique is a dynamic method that assumes that the recovery of an extended drop to a sphere is driven by a uniform interfacial tension γ and rate-limited by the viscosity μ of a Newtonian drop (chapters 4 and 5). As such, γ values obtained with this dynamic technique may be affected by additional surface dissipation.

Table 6.1. Interfacial tension γ of bitumen drops in different aqueous suspensions. Values shown represent the average of a minimum of ten individual measurements and the reported errors are standard deviations about the mean. The behaviour of bitumen drops, as defined in the text, and the pH of the aqueous phase are also provided.

Aqueous Suspension	*pH*	*Microcantilever* γ *(mN/m)*	*Drop Shape Recovery* γ *(mN/m)*	*Drop Behaviour*
DIW	6.0	20.3 ± 1.0	21.5 ± 1.2	Ideal
DIW + M	6.4	24.5 ± 1.4	23.9 ± 1.7	Ideal
DIW + M + Ca^{++}	6.2	24.4 ± 1.3	—	Plastic

The interfacial tensions measured by the two micropipette techniques compare well for Athabasca bitumen drops in both the DIW and the DIW + M systems. This indicates that viscous dissipation occurs primarily in the bulk bitumen phase and any surface viscosity is relatively negligible. In a previous micropipette study, it was observed that viscous dissipation at diluted bitumen-water interfaces was notably reduced as the bitumen phase became more concentrated (Yeung et al., 1999). Extrapolating this finding to pure bitumen (i.e., zero dilution) provides agreement with our current results. In addition, studies of planar crude oil-water interfaces (Neustadter et al., 1975; Cairns et al., 1976; Jones et al., 1978) showed that surface shear viscosity was not appreciable over a wide range of slightly acidic to alkaline ($pH > 4$) aqueous phases for some crude oils. However, it should be noted that surface dilational viscosity of some crude oil-water interfaces was shown to be somewhat significant at neutral pH (Neustadter et al., 1981).

As shown in Table 6.1, the aqueous phases in the present study are slightly more acidic than neutral at pH ~ 6.

The bitumen drop interfacial tensions measured for the DIW + M system are notably larger than those of the DIW system (Table 6.1). The two tensiometric techniques employed in this study assume that an equilibrium interfacial tension is the only material property at the interface. However, it is possible that these methods are measuring an interfacial stress involving both an equilibrium interfacial tension (invariant to area changes) and an area-dependent surface elastic parameter. Thus, it could be argued that the increase in measured tension in the DIW + M system is attributed to the development of elastic properties at the interface. However, any elastic contributions are likely negligible, as all emulsion drops are spherical in their stress-free state. (If elastic effects were significant, one would expect to observe non-spherical drops within the emulsion). An alternate explanation may be attributed to the presence of dispersed montmorillonite particles. Charged clay particles in suspension may attract surfactants away from fluid-fluid interfaces accounting for an increase in interfacial tension by up to ~ 4 mN/m for oil-water systems (Schramm and Hepler, 1994). In both the DIW and DIW + M systems, ideal behaviour is noted (Table 6.1), as the bitumen drops always returned to spherical shapes following applied deformations.

As reported from the microcantilever technique, the bitumen drop interfacial tension in the DIW + M + Ca^{++} system is nearly identical to that observed in the DIW + M system (Table 6.1), indicating that calcium ions have little effect on this material property (cf. figure 3.5). As bitumen drops in the DIW + M + Ca^{++} system exhibit plastic behaviour (partial recovery to non-spherical shapes), the drop shape recovery technique is ineffective in assessing the interfacial tension of the bitumen drops.

6.3.3 Stress-strain microcantilever experiments

Static stress-strain type studies are conducted on individual bitumen drops with the microcantilever apparatus where an axial force f is applied (loading) and relaxed (unloading) in a stepwise manner. (See figure 3.1 for a sequential series of photographs depicting the loading stage of a typical experiment.) In these experiments, an individual drop undergoes three consecutive loading-unloading cycles.

For bitumen drops in deionized water (DIW) and aqueous montmorillonite (DIW+M) suspensions, the stress-strain experiments indicate ideal behaviour (figure 6.2). Measures of the axial drop length L are relative to a reference state represented by axial length L_i. In practice, L_i is obtained by fitting the f vs. L experimental data to a polynomial and extrapolating the fit to a stress-free state (i.e., $f = 0$). Thus, as all drops examined in this study are initially spherical, a drop deformation of $L - L_i = 0$ indicates a spherical drop. The unloading curves map onto the loading curves for each drop stretch (denoted by 1, 2 or 3), indicating a lack of hysteresis for the loading-unloading loops. Furthermore, each loading-unloading loop lies on approximately the same path as the others. Following each unloading stage the drop appears to recover to an essentially spherical shape. (This may be seen by extrapolating the unloading curves to the abscissa at $L - L_i \approx 0$). These data suggest that bitumen drops in DIW and DIW + M behave in a reversible manner. At no point during experiments with DIW and DIW + M systems is there any evidence of a rigid skin formation. These findings are in agreement with Yeung and coworkers (1999), who observed that only fluid (i.e., non-rigid) interfaces were present at water drop surfaces in solvent-diluted Athabasca bitumen when the solvent-to-crude oil ratio was low (i.e., concentrated bitumen). Recall that in the present experiments, emulsion drops of pure Athabasca bitumen are studied.

The response of bitumen drops in aqueous environments of montmorillonite and calcium ions (DIW + M + Ca^{++}) to stress-strain microcantilever experiments is strikingly different from that observed in the DIW and DIW + M systems. A typical f versus $L - L_i$ plot is shown in figure 6.3. There is significant hysteresis between loading and unloading curves for individual loading-unloading cycles. In addition, consecutive loading-unloading loops (denoted by 1, 2 or 3) are offset by the magnitude of the hysteresis observed at an approximately stress-free state (i.e., in the absence of an applied axial force $f = 0$). This is clear evidence of plastic behaviour exhibited by bitumen drops suspended in an aqueous environment of montmorillonite clays and calcium ions. Again, as with the bitumen drop surfaces in DIW and DIW + M systems, obvious skin formation is not observed.

Plastic behaviour has been documented, although not specifically discussed, in previous studies of crude oil-water interfacial rheology. Dodd (1960) reported the

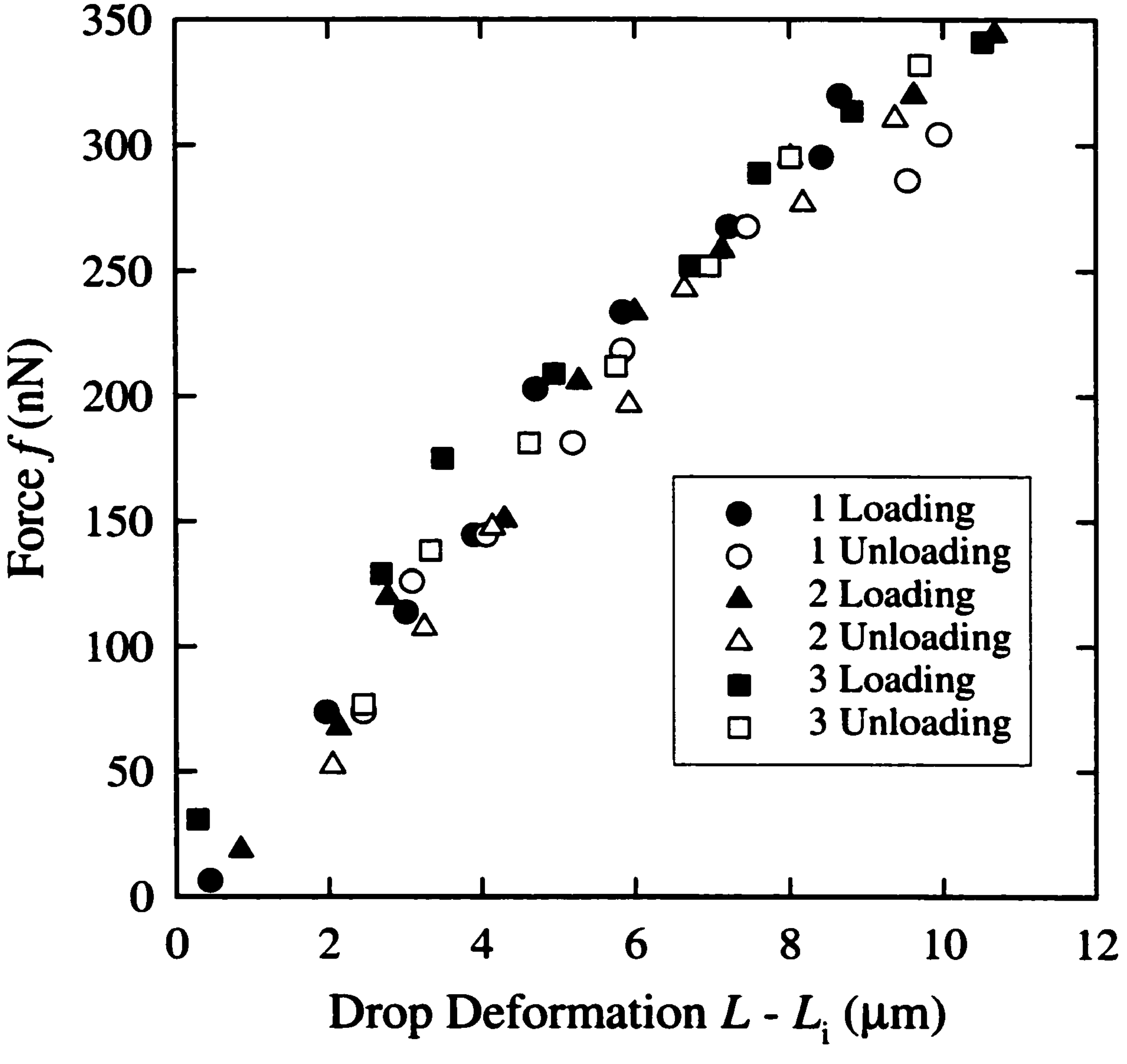

Figure 6.2. Typical loading-unloading curves, obtained with the microcantilever technique, for bitumen drops exhibiting ideal behaviour (i.e., those in DIW and DIW + M aqueous systems). The drop is subjected to three consecutive loading-unloading cycles, denoted by 1 (circles), 2 (triangles) and 3 (squares), respectively. The loading curves are shown in solid symbols and the unloading curves are shown in open symbols. The applied force f is determined from the microcantilever deflection, while the drop deformation $L-L_i$ is relative to an initial spherical state.

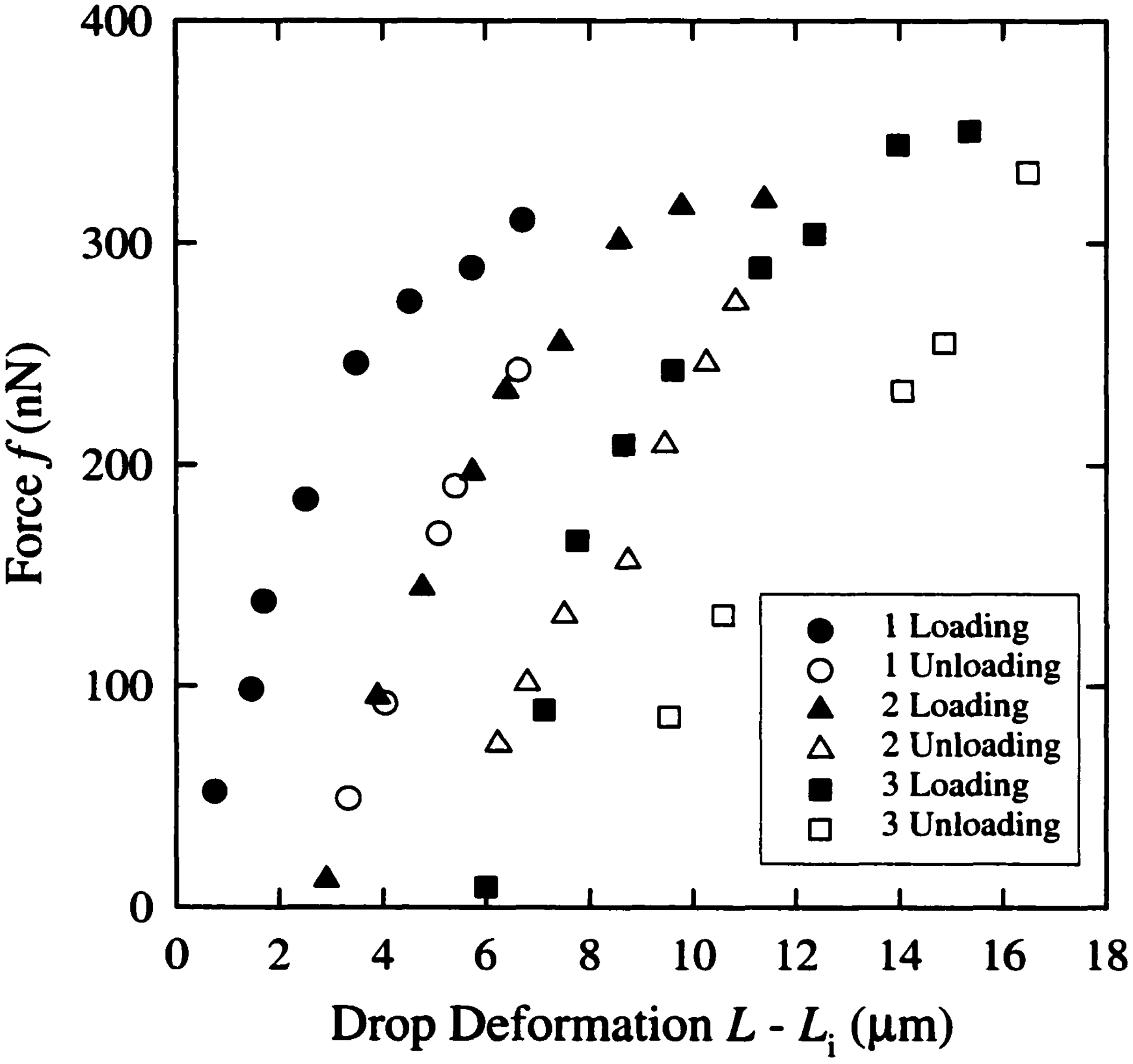

Figure 6.3. Loading-unloading curves, obtained with the microcantilever technique, for a bitumen drop exhibiting plastic behaviour (i.e., a drop in a DIW + M + Ca^{++} system). Refer to figure 6.2 for further description.

presence of thixotropic surface properties while Cairns and coworkers (1976) discussed surface shear viscosity of such interfaces in detail. However, their results clearly demonstrated plastic deformations at the interface as the torsional bobs of their surface viscometers did not return to their initial stress-free positions upon cessation of the viscometer rotation. Plastic behaviour of surfaces was apparently first noted by Wilson and Ries (1923), who developed elegant experiments to show the irreversible nature of some liquid-liquid interfaces.

The slopes of consecutive loading curves for a single bitumen drop in DIW + M + Ca^{++}, (solid symbols in figure 6.3) are approximately equal. This may indicate the absence of surface strain hardening - the development of additional elastic stresses at the interface due to deformation. (If strain hardening was observed, one would expect the slopes to increase upon consecutive loading-unloading cycles – cf. Inokuchi, 1955). Furthermore, the slopes of the loading curves in figure 6.3 (DIW + M + Ca^{++} systems) are approximately the same as those in figure 6.2 (DIW + M systems). This may indicate that the plastic behaviour is manifested only during the unloading of the drop. The initial slopes of these force-drop deformation plots may be related to an apparent spring constant that is a function of the drop geometry and the interfacial tension (Evans et al., 1991; Evans et al., 1995; see equation 2.10). Thus, given that all drops examined in this study are approximately the same size, it is not surprising that the tensions of these two systems (DIW + M and DIW + M + Ca^{++}) are the same (Table 6.1).

6.3.4 Creep compliance tests

Viscoelasticity has been documented in some crude oil-water interfacial studies by estimating the initial slope of a creep compliance curve generated with a rotational interfacial rheometer (Jones et al., 1978; Mohammed et al., 1993, 1994). In the present work, creep compliance tests are conducted with the microcantilever apparatus to assess the viscoelastic nature of the bitumen drop surfaces. In such tests, individual bitumen drops in each of the three aqueous systems are stretched at a constant force and the axial drop length monitored over times of up to two hours. A typical result is shown in figure 6.4 (solid circles) for a bitumen drop in DIW + M + Ca^{++}. In this experiment, the drop deformation $L - L_i$ is monitored as a constant force of ~ 372 nN is applied.

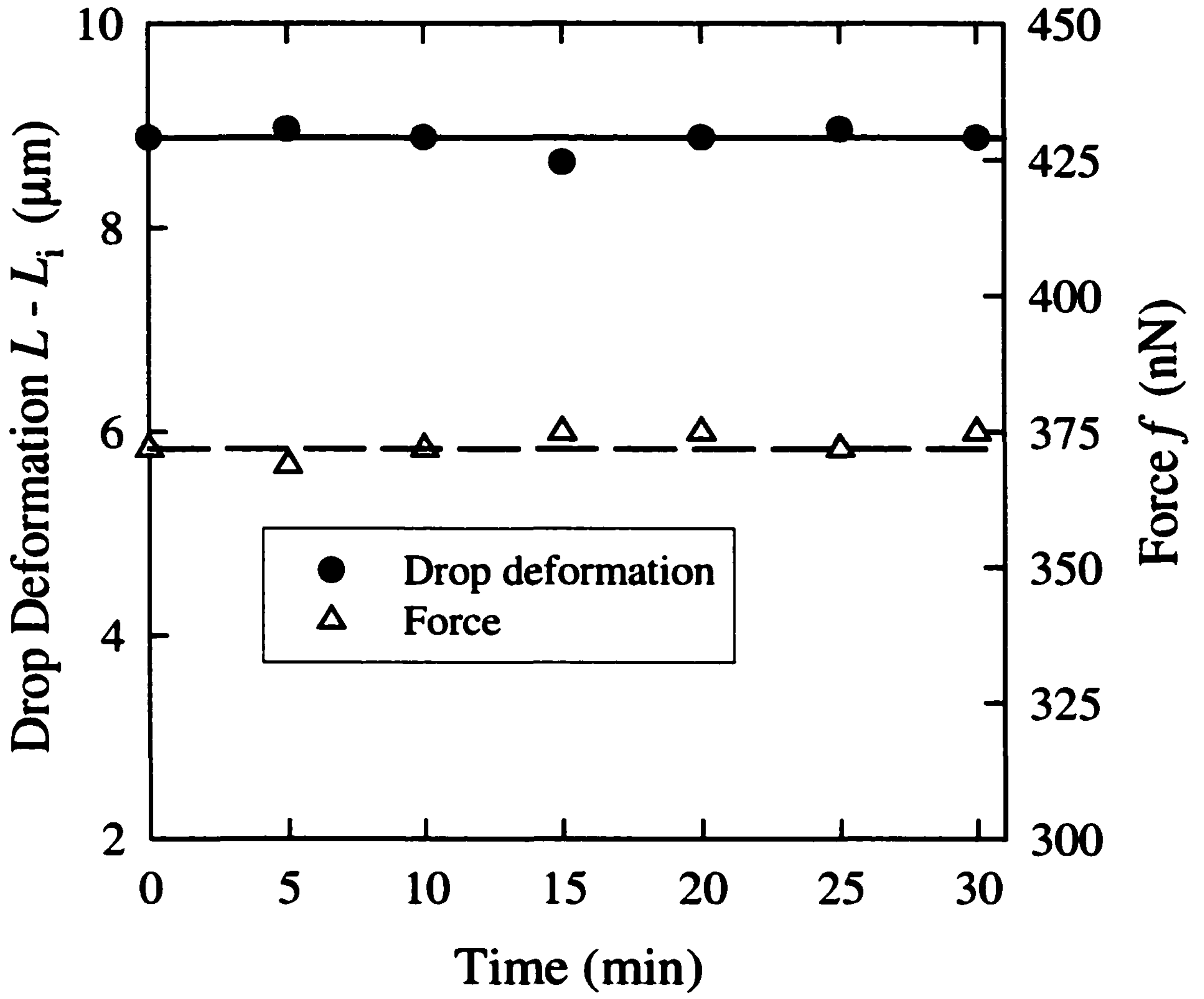

Figure 6.4. A typical creep compliance test for a bitumen drop exhibiting plastic behaviour in DIW + M + Ca^{++}. A bitumen drop is deformed with the microcantilever technique at a constant force f (open triangles). The drop deformation L–L_i (solid circles) is measured as a function of time. The lines represent the mean values of the measured drop deformation (solid) and applied force (dashed).

The force is measured through the microcantilever deflection and noted to be constant throughout the test (open triangles in figure 6.4). It is evident that the drop length remains constant over the entire test, indicating that the bitumen drop surface in an aqueous solution of montmorillonite clays and calcium ions is not viscoelastic. Similar results are obtained for bitumen drops in DIW and DIW + M (not shown). Typical analysis of the creep compliance test results would suggest that Athabasca bitumen drop surfaces in any of the aqueous environments are purely elastic in nature (Joly, 1972). However, as noted above, it is likely that elastic contributions are negligible for the DIW and DIW + M systems. Since the interfacial tension measured for the DIW + M + Ca^{++} system is comparable to that of the DIW + M system (Table 6.1), it is reasonable to assume that surface elastic contributions are also negligible for bitumen drop surfaces in aqueous environments of montmorillonite clays and calcium ions. Then, for a bitumen drop in any of the three aqueous systems, the "elastic" nature of the surface is provided primarily by the interfacial tension.

6.3.5 Static analysis of drop shape recovery experiments

To further explore the surface rheology of bitumen drops, shape recovery experiments are conducted. In this section, the dynamics of the recovery process is not considered; only the maximum extended length L_o and the final length L_f of the drop following recovery are measured. Shape recovery experiments of bitumen drops in deionized water (DIW) and an aqueous montmorillonite suspension (DIW + M) indicate ideal behaviour in that axially stretched drops always recover to static spherical shapes. This is in agreement with the stress–strain results obtained in the microcantilever experiments (figure 6.2).

The maximum and final lengths, L_o and L_f, of bitumen drops in the DIW + M + Ca^{++} system are observed during shape recovery experiments (figure 6.5). In this figure, axial lengths are scaled by the drop diameter $2R_d$. (Thus, an extended drop that recovers to a sphere will have a final scaled length $L_f/2R_d$ of unity.) The limiting behaviours, ideal and perfectly plastic, are plotted as solid and dashed lines, respectively. Many interesting observations can be made from the results of this experiment. Indeed, plastic behaviour is noted for moderately extended bitumen drops as their final axial lengths L_f fall between

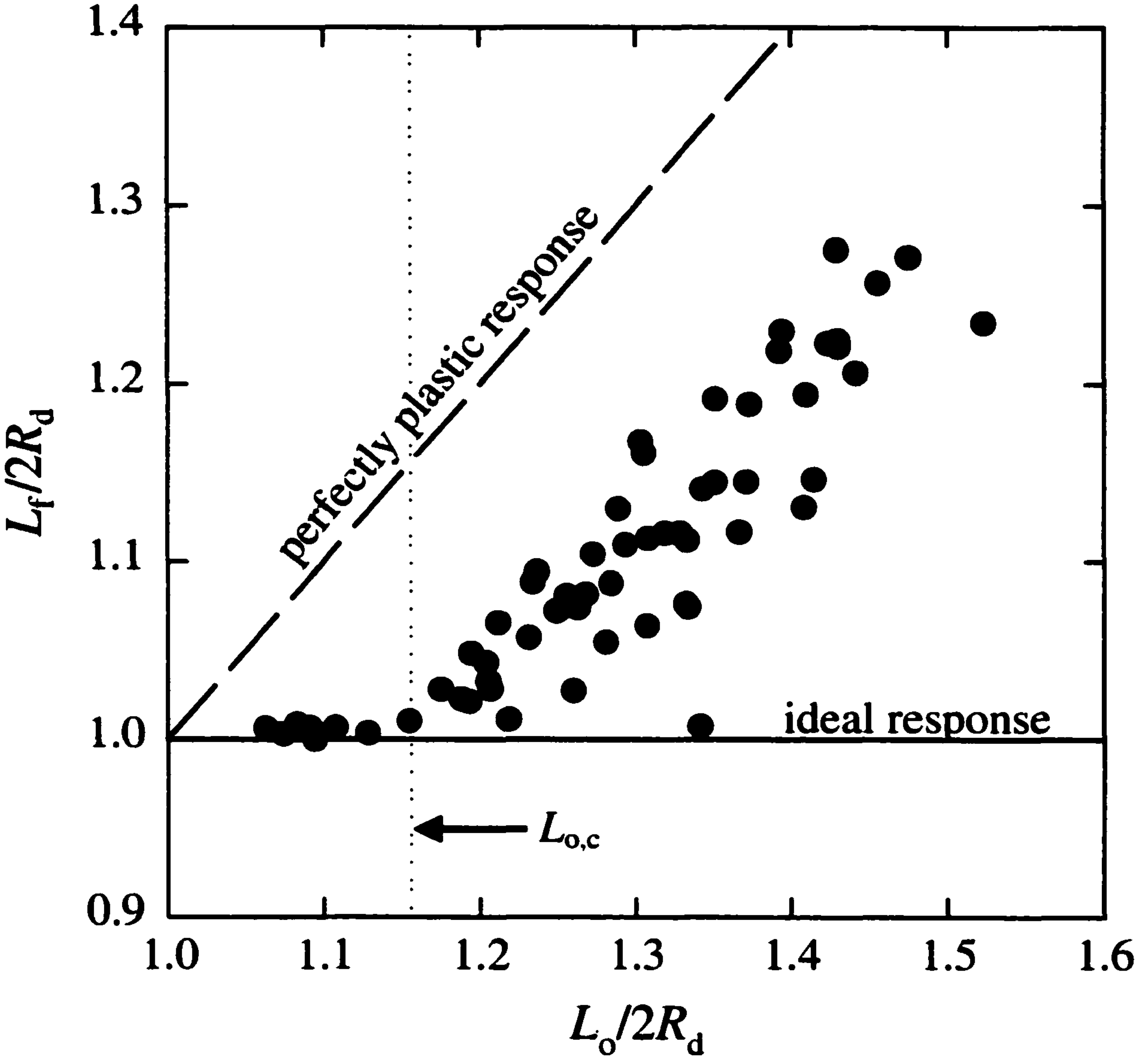

Figure 6.5. Static analysis of drop shape recovery experiments for bitumen drops exhibiting plastic behaviour in DIW + M + Ca^{++}. The final drop lengths following relaxation L_f are plotted as a function of the maximum drop extensions prior to release L_o. The drop lengths are scaled by the spherical drop diameters $2R_d$. Ideal and perfectly plastic behaviours are plotted as solid and dashed lines, respectively. A critical maximum elongation is noted at $L_{o,c}/2R_d \approx 1.17$ (vertical dotted line). A drop elongated to above $L_{o,c}/2R_d$ exhibits plastic behaviour, while a drop stretched to a state below $L_{o,c}/2$ R_d shows ideal behaviour.

the two limiting curves ($1 < L_f/2R_d < L_o/2R_d$). Moreover, a critical maximum stretch $L_{o,c}$ exists, above which plastic behaviour ($L_f/2R_d > 1$) is observed and below which ideal behaviour ($L_f/2R_d = 1$) is noted. For bitumen drops in DIW + M + Ca^{++}, this critical drop elongation is $L_{o,c}/2R_d \approx 1.17$ (vertical dotted line in figure 6.5). A typical applied force and surface stress corresponding to $L_{o,c}$ can be estimated from the stress-strain curves (figure 6.3) at a relative deformation of $(L - L_i)/2R_d \sim 0.17$ (approximately equivalent to $L_{o,c}/2R_d \approx 1.17$). At this critical deformation, the applied force is $f_c \sim 250$ nN, giving an approximate surface stress of $f_c/2\pi R_d \sim 4$ mN/m for a typical drop size of $R_d \approx 10$ μm. Furthermore, at extensions above the critical point ($L_o/2R_d > L_{o,c}/2R_d$) there appears to be a linear relationship, albeit with a great deal of experimental variation, between L_o and L_f such that $L_f \approx 0.85L_o$. This is the first characterization of the plastic surface properties of single bitumen emulsion drops. However, yield values of sodium soap Bingham plastic surfaces, believed to exhibit surface behaviours similar to some crude oil-water interfaces, have been estimated (Brown et al., 1953).

6.3.6 Is plastic behaviour a surface phenomenon?

It is evident that plastic behaviour is noted for bitumen emulsion drops in aqueous suspensions of montmorillonite clays and calcium ions. This plastic behaviour has thus far been attributed to the bitumen drop surface without validation other than noting that Athabasca bitumen is generally known to exhibit Newtonian behaviour (Schramm and Kwak, 1988). Could this plastic behaviour be due to a change in the bulk rheology of bitumen drop as opposed to a surface phenomenon? To consider this, the following experiment is conducted. The interior of a highly irregular, non-spherical bitumen drop in DIW + M + Ca^{++} (see figure 6.1) is carefully extracted via micropipette suction. The aspirated bitumen is immediately expelled from the micropipette and is seen to form a spherical drop. This drop is then mechanically deformed in drop shape recovery experiments. Ideal behaviour is noted, as this freshly-formed drop recovers to a sphere, if such experiments are conducted immediately after the drop is expelled. However, if the surface of the freshly formed drop is allowed to age for approximately one to 10 minutes in the aqueous suspension (DIW + M + Ca^{++}), drop shape recovery experiments reveal plastic behaviour as the drop shows some recovery but ultimately relaxes to a final, non-spherical shape. These experiments clearly demonstrate that the plastic behaviour observed with bitumen drops in DIW + M + Ca^{++}, in response to mechanical deformation, is attributed to the bitumen drop surface.

6.3.7 Dynamic analysis of drop shape recovery experiments

The microcantilever experiments and the static analysis of bitumen drop shape recovery reveal information concerning the time-independent nature of bitumen drop surfaces in aqueous suspensions. However, they do not provide insights into the dissipative nature of such interfaces. Drop shape recovery experiments are utilized to monitor the dynamic recovery and the viscous dissipative behaviour of axially deformed bitumen drops. Sequential series of photographs showing typical shape recovery experiments with bitumen drops indicate ideal behaviour in DIW + M systems (figure 6.6a) and plastic behaviour in DIW + M + Ca^{++} systems (figure 6.6b). The last photograph in each series represents the final, time-independent shape of the drop.

In drop shape recovery experiments, bitumen drops in DIW or DIW + M behave ideally, always recovering to spheres. In such a recovery, it is assumed that the drop recovery is driven by the interfacial tension. It is also assumed that any rate-limiting dissipation is due to the Newtonian viscosity of bitumen and that the surface is essentially inviscid. (In fact, the term "ideal" is in reference to this inviscid nature of the surface of a viscous drop.) The recovery of emulsion drops exhibiting ideal behaviour is well described by a Stokesian model (refer to chapter 4) that is based on these assumptions (figure 6.7). Since a well-defined characteristic velocity γ/μ is available, with γ from Table 6.1 and μ from figure 5.3, no fitting is involved. The agreement of the dynamic drop length $L(t)$ between the experimental data (solid circles) and the Stokesian model (dash-dot line) suggests that little surface viscosity exists in these systems.

Analysis of bitumen drop recoveries in DIW + M + Ca^{++} provides for interesting results. The plastic nature of the interface is observed as the bitumen drops do not recover to spheres ($L_f/2R_d > 1$) as time approaches infinity $t \rightarrow \infty$ (figure 6.8). In this case, note that the maximum drop deformation ($L_o/2R_d = 1.35$) is above the critical value ($L_{o,c}/2R_d \approx 1.17$) required for plastic behaviour and that $L_f/L_o \approx 0.85$. In many of the drops examined, dissipation above that provided by the bitumen viscosity μ is observed.

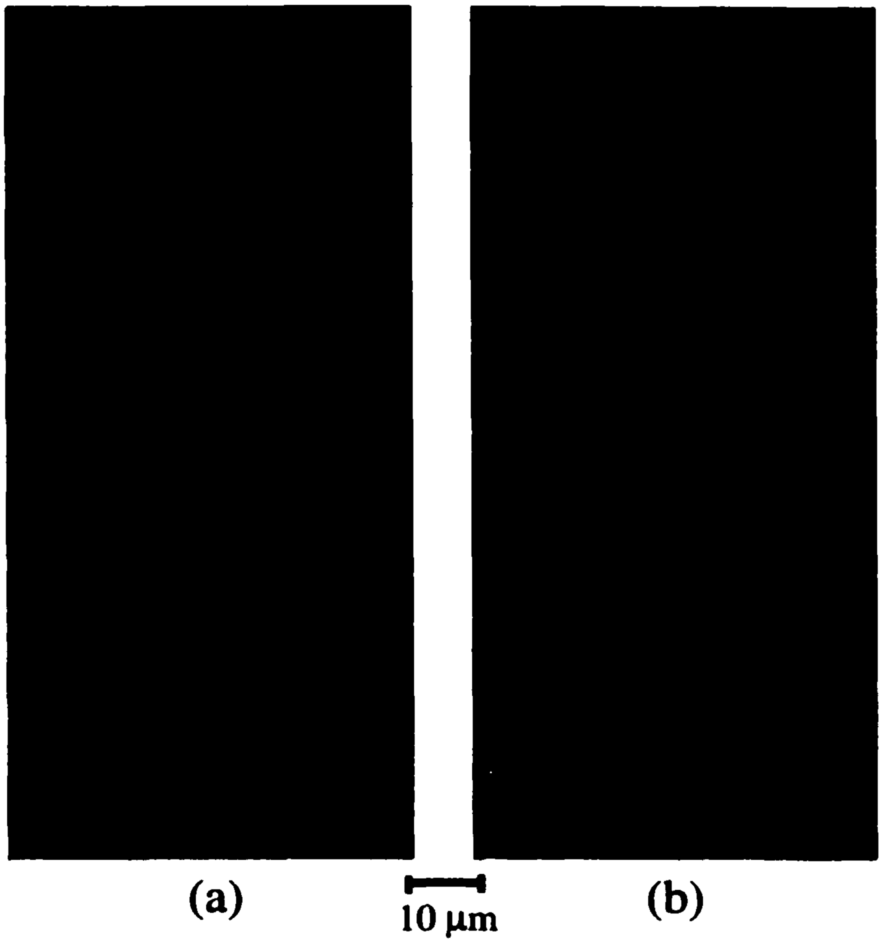

Figure 6.6. Sequential series of photographs (top to bottom) depicting a drop shape recovery experiment for a bitumen drop (a) in DIW + M exhibiting ideal behaviour and (b) in DIW + M + Ca^{++} exhibiting plastic behaviour. In drop shape recovery experiments, an initially spherical drop is axially stretched to a maximum deformation (L_0 at time $t = 0$) and released from one micropipette. The dynamic recovery $L(t)$ of such a drop to a final shape is measured. The final photographs (at $t = 3.73$ s (series a) and $t = 4.57$ s (series b)) show the final, time-independent drop shapes. Note that, in the aqueous phase of series (b), the montmorillonite fines appear swelled or aggregated relative to series (a).

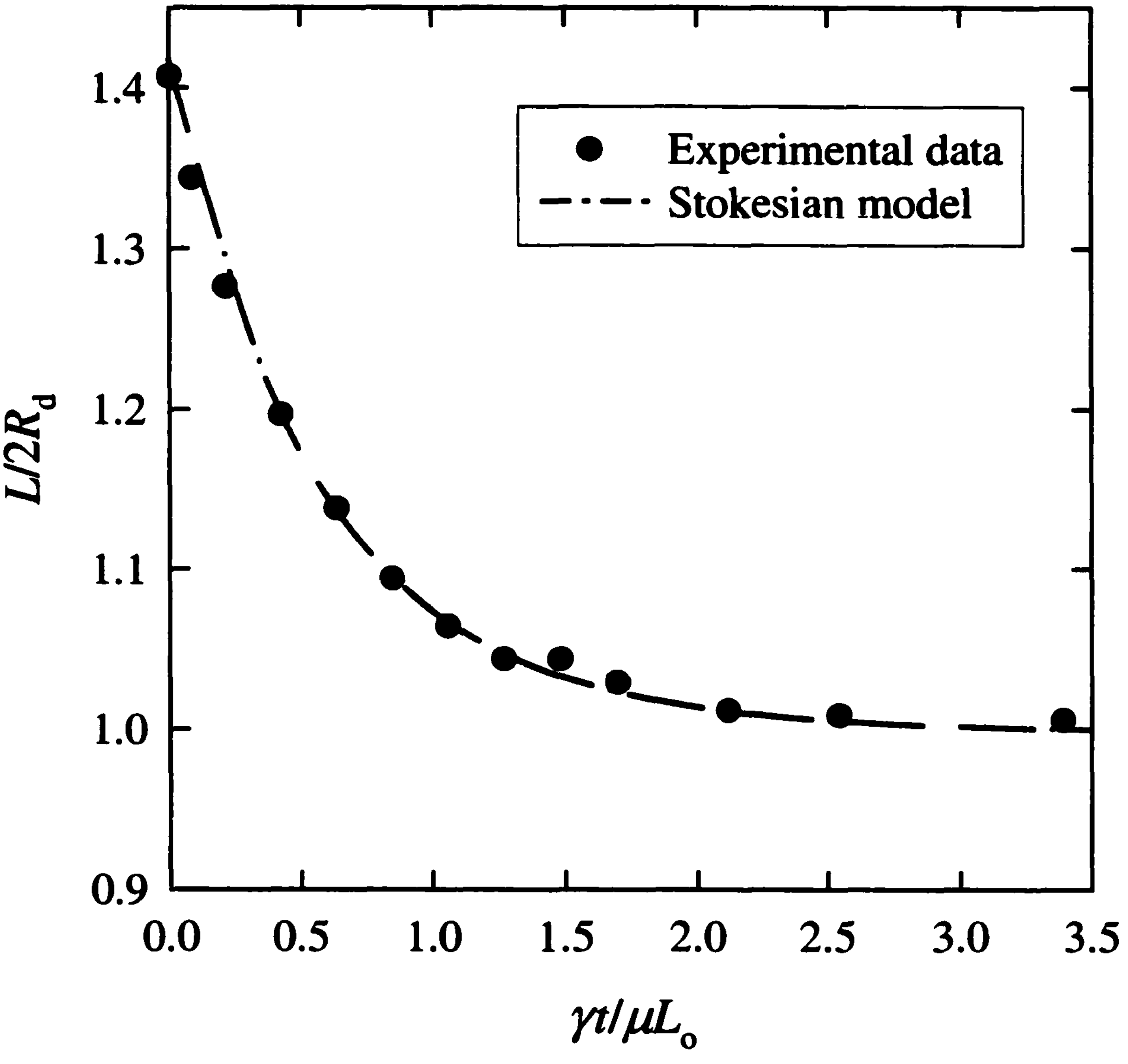

Figure 6.7. Typical dynamic drop shape recovery data for an extended bitumen drop exhibiting ideal behaviour (see figure 6.6a). In this case, the aqueous phase is DIW + M. Time is scaled by a characteristic recovery time $\mu L_o/\gamma$, while the dynamic drop length is scaled by the drop diameter $2R_d$. The experimental drop recovery (solid circles) is well described by the Stokesian model (dash-dot curve). The interfacial tension is obtained from Table 6.1 and the viscosity of bitumen is 1246 Pa·s. Note that the experimental data and the model indicate that drop recovers to a sphere as $L_f/2R_d = 1$.

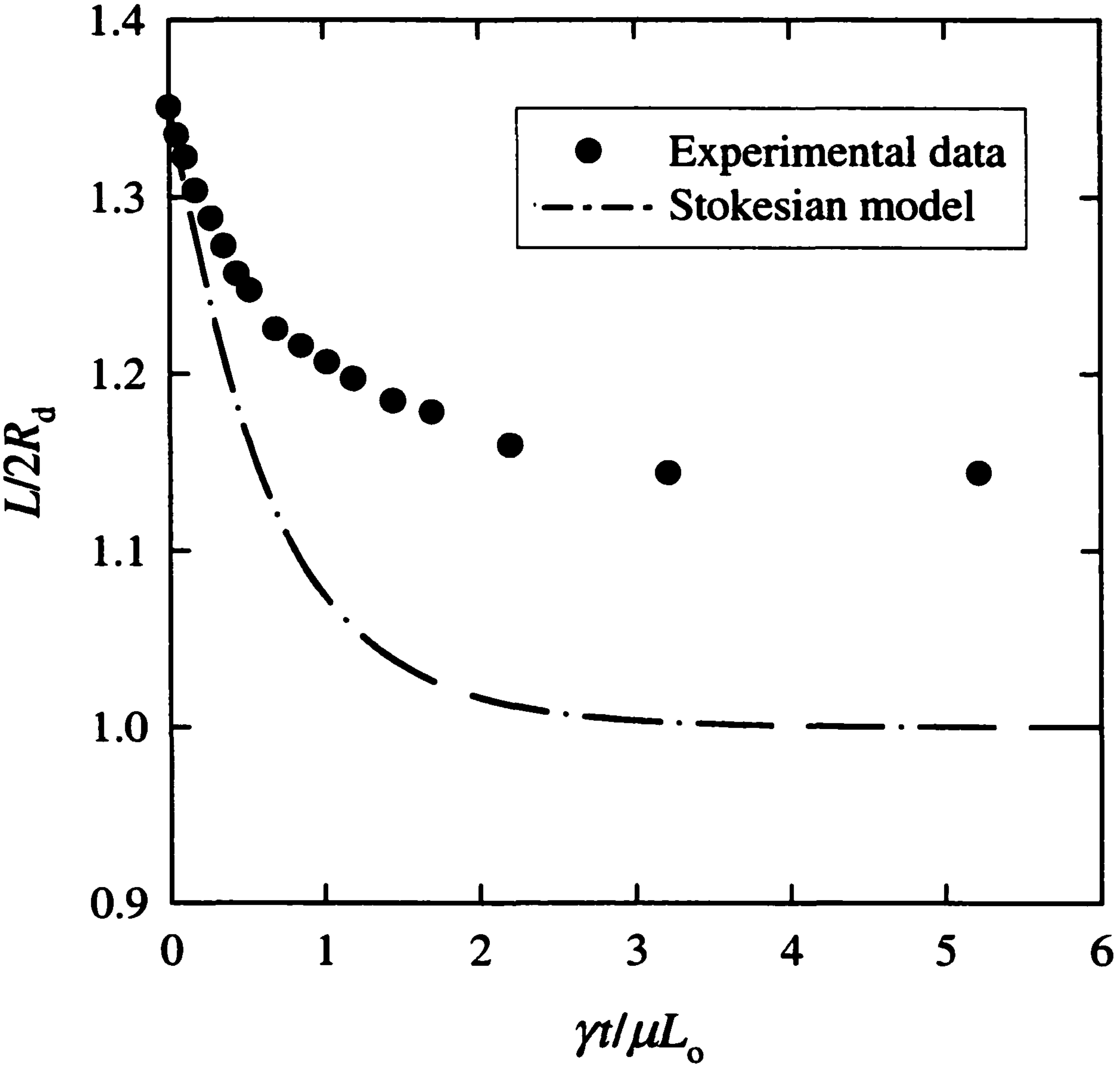

Figure 6.8. Typical dynamic drop shape recovery data for an extended bitumen drop (in DIW + M + Ca^{++}) exhibiting plastic behaviour (see figure 6.6b). Time is scaled by a characteristic recovery time $\mu L_o/\gamma$, while the dynamic drop length is scaled by the drop diameter $2R_d$. Note that the recovery described by the Stokesian model (dash-dot curve) deviates significantly from the experimental data (circles) as $t \rightarrow \infty$. As a well-defined characteristic velocity is available, no fitting is involved in this approach. (The interfacial tension is obtained from Table 6.1 and the viscosity of bitumen is 1246 Pa·s).

This is evident as the initial experimental drop recovery (solid circles) is retarded relative to that described by the Stokesian model (dash-dot line). The *additional* dissipation must be attributed to the surface and may be due to interactions of adsorbed calcium-montmorillonite aggregates. It is important to note that the observed surface dissipation shows a great deal of variation among drops. In fact, some plastically behaving drops initially exhibit ideal behaviour (i.e., followed the Stokesian recovery exactly), and then their dynamic recovery is almost immediately halted as they reach their final plastic length $L_f/2R_d > 1$. Since the Stokesian model assumes that drops recover to spheres, it shows significant deviation for drops exhibiting surface plasticity as $t \rightarrow \infty$.

Sears (1952) indicated that some crude oil-water interfaces exhibited pseudoplasticity (shear-thinning), where the apparent surface viscosity decreases with increasing shear rate. In the present study, the bitumen surface shear rates are greatest when the drop is at its maximum deformation L_0 and decrease as the drop recovers (examine the slopes in figure 6.8). Insofar as the discrepancy between some of the experimental data and the ideal Stokesian recovery increases as the shear rate decreases, it may suggest that the apparent viscosity at the bitumen surface increases. However, it is not clear whether the observed surface dissipation is of a pseudoplastic nature or whether it is due to a mechanism resulting in the permanent plastic deformation (independent of any surface viscosity). Surface pseudoplasticity of sodium soap solutions, believed to exhibit similar surface characteristics as crude oil-water interfaces (Sears, 1952), has been examined using an oscillating disc (torsional pendulum) method, first described by Wilson and Reis (1923). The effects of pH and soap concentration on the pseudoplastic transition temperature, a temperature above which the surface viscosity is independent of shear rate, of these soap films has also been investigated (Sears, 1952; Burcik et al., 1954; Burcik and Newman, 1957). It may be interesting to investigate the thermomechanical properties of bitumen drop-water interfaces in similar regimes.

6.7.8 Lumped parameter surface plasticity model

A rigorous model describing the plastic recovery of extended emulsion drops, with surface dissipation incorporated, is exceedingly difficult and beyond the scope of this thesis. As a first attempt to describe such a relaxation process, a simple force balance model is proposed. In this lumped parameter model, based on the axial length dimension L of the drop, it is assumed that a uniform interfacial tension γ is driving the recovery process and that all viscous dissipation is due to the bitumen viscosity μ (surface dissipation is ignored as a first approximation). The model, including the initial condition stating the maximum drop extension L_o, is of the following form

$$\gamma(L-2R_d) - F_y R_d = -2\mu R_d \cdot \frac{dL}{dt}; \qquad L(0) = L_o, \tag{6.1}$$

where $\gamma(L - 2R_d)$ is the force driving the recovery of an extended drop to a sphere $2R_d$. In the second term of equation 6.1, F_y is a constant surface stress opposing relaxation and represents the irreversible nature of the interface. For a drop exhibiting ideal behaviour $F_y = 0$. The viscous dissipation is provided on the right hand side of equation 6.1. An expression for F_y is readily available when a static situation $dL/dt = 0$ at the final drop length L_f is considered, giving

$$F_y = \gamma \frac{(L_f - 2R_d)}{R_d}. \tag{6.2}$$

Note that for drops that behave ideally ($F_y = 0$) $L_f = 2R_d$, indicating a final spherical shape. Equation 6.1 may be integrated in accordance with the initial condition to arrive at the following analytical solution,

$$\frac{L}{2R_d} = \left(\frac{L_o - L_f}{2R_d}\right) \cdot \exp\left(-\frac{\gamma t}{2R_d \mu}\right) + \frac{L_f}{2R_d}, \tag{6.3}$$

which has been scaled by $2R_d$. The exponential term in equation 6.3 describes the dynamic, dissipative recovery process between the initial L_o and final L_f drop lengths. A consistency check reveals that at $t = 0$, $L = L_o$, while as $t \rightarrow \infty$ the drop recovers to its final length L_f. In implementing this lumped parameter model, the equilibrium interfacial tension γ is obtained from Table 6.1, the bitumen viscosity μ is taken as 1246 Pa·s (see chapter 5), while L_o and L_f are measured from digitized photographs of drop recovery experiments (as discussed in chapters 4 and 5).

Considering its one-dimensional nature, the lumped parameter model with $F_y = 0$ (solid line in figure 6.9) follows the drop dynamics described by the Stokesian model (dash-dot line in figure 6.9) quite well for drops exhibiting ideal behaviour. As an approximate method, the lumped parameter model appears to capture the basic physics of extended drop recovery. In fact, this model (equation 6.3) provides an analytical alternative for estimating interfacial tensions via shape recovery experiments (assuming the viscosity is known *a priori*)!

The simple, lumped-parameter model appears to adequately describe the dynamic recovery of bitumen drops with plastic surfaces (i.e., those in DIW + M + Ca^{++} systems; solid line in figure 6.10). It is apparent that the surface stress term F_y accounts for the irreversible plasticity observed at the bitumen drop surface. Thus, despite some evidence of surface dissipation, the physics of such a drop recovery can be reasonably described by the interfacial tension γ, a constant surface stress F_y opposing recovery and the bulk viscosity μ. Note also that, if this drop were to behave ideally and recover to a sphere, the "ideal" lumped parameter model (where $F_y = 0$; dashed line in figure 6.10) follows the relaxation described by the Stokesian model (dotted line, figure 6.10) very well.

6.3.9 Possible mechanism to describe surface plastic behaviour

It is apparent that the presence of *both* calcium ions and montmorillonite clays plays a role in the surface plastic behaviour of bitumen drops. Indeed, the appearance of an aqueous montmorillonite slurry changes upon the addition of small amounts of calcium, as the clays appear to swell or aggregate (compare the aqueous environments in figure 6.6). A possible mechanism accounting for this surface plasticity will now be briefly postulated.

This mechanism is based on the assumption that sub-micron calcium-montmorillonite (CaM) aggregates can irreversibly[21] reside on a (negatively charged) bitumen drop surface. Even though montmorillonite is hydrophilic (and may exhibit only minimal wetting characteristics), this could be possible since a free cationic site is created as the monovalent sodium ions originally associated with the montmorillonite exchange

---

[21] This mechanism assumes that the characteristic shape recovery time is shorter than that involved in the CaM adsorption kinetics, thereby inferring that the adsorption of these complexes is somewhat irreversible.

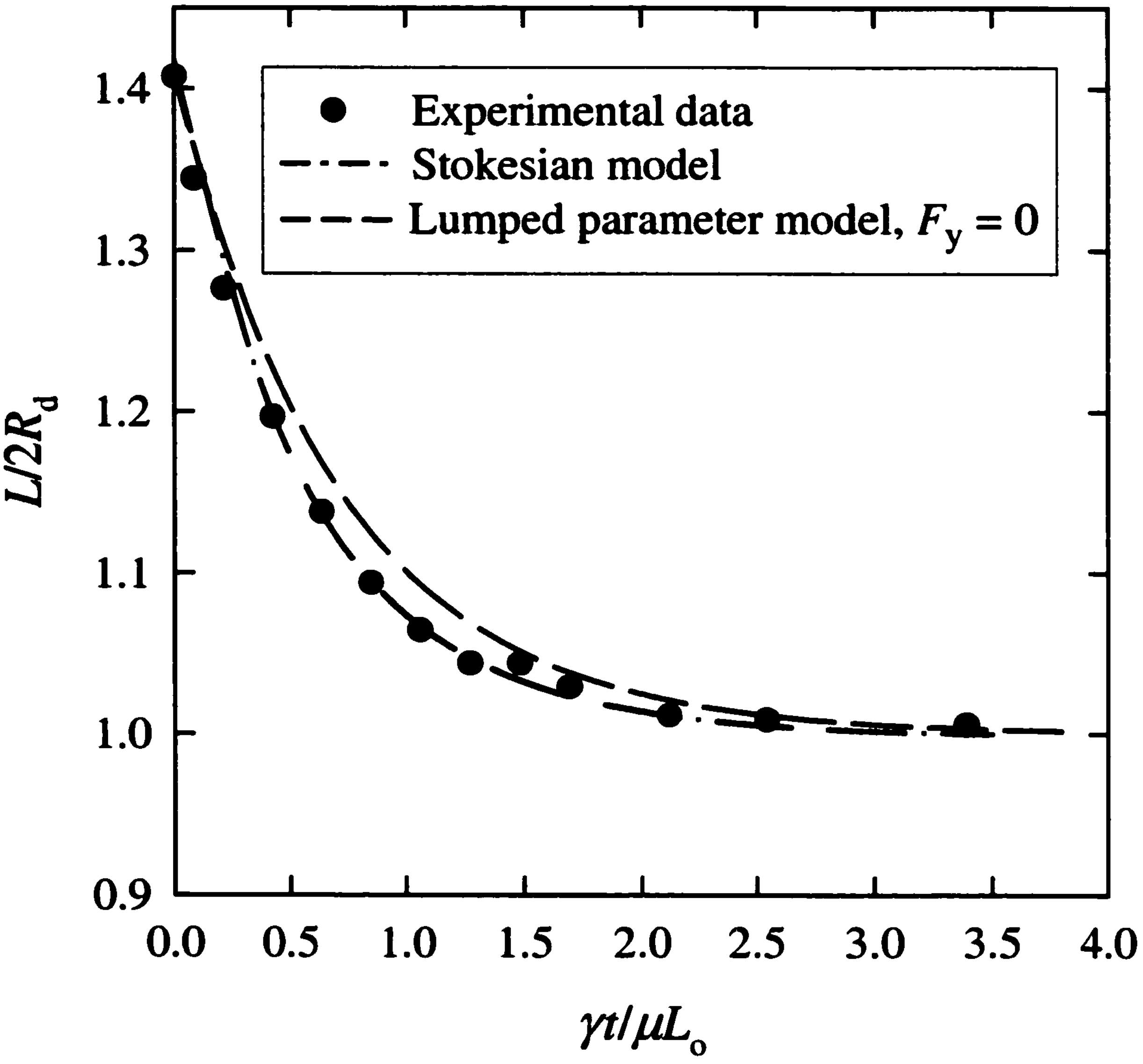

Figure 6.9. Comparison of lumped-parameter model to Stokesian approach and experimental data for an ideally behaving bitumen drop. In this case, the aqueous phase is DIW + M. Time is scaled by a characteristic recovery time $\mu L_o/\gamma$, while the dynamic drop length is scaled by the drop diameter $2R_d$. The experimental drop recovery (solid circles) is well described by the Stokesian model (dash-dot curve). As a well-defined characteristic velocity is available, no fitting is involved in this approach. (The interfacial tension is obtained from Table 6.1 and the viscosity of bitumen is 1246 Pa·s). Considering its simplicity, the ideal lumped-parameter model (equation 6.3), in which $F_y = 0$ (dashed curve), also appears to follow the experimental data quite well. Note that the experimental data and the models indicate that drop recovers to a sphere as $L_f/2R_d = 1$.

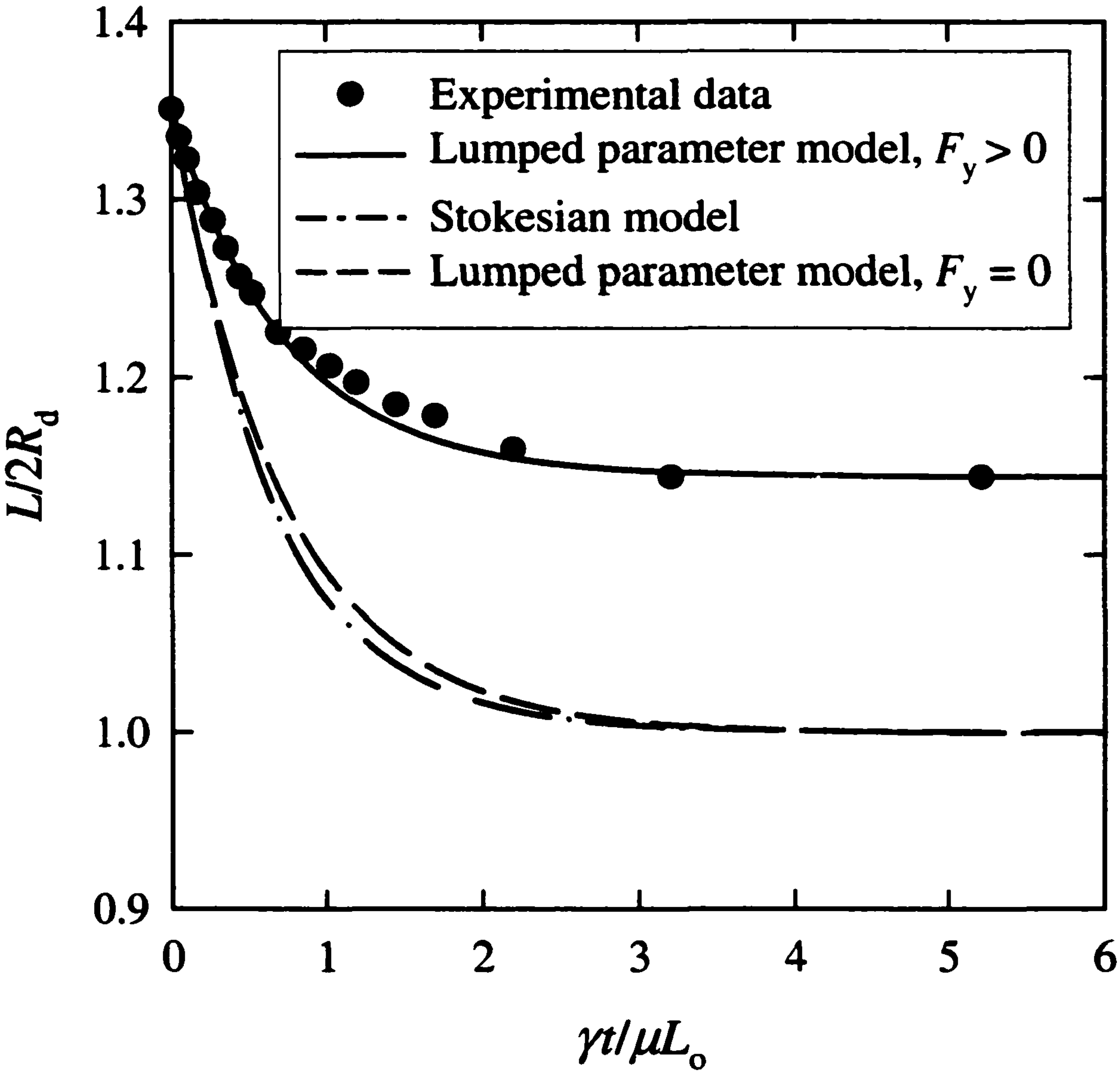

Figure 6.10. Comparison of lumped-parameter model to Stokesian approach and experimental data for a plastically behaving bitumen drop. Time is scaled by a characteristic recovery time $\mu L_0/\gamma$, while the dynamic drop length is scaled by the drop diameter $2R_d$. The experimental data (solid circles) is well described by the lumped parameter model (solid curve) as the drops recover to non-spherical shapes $L_f/2R_d > 1$. Note that the recovery described by the lumped parameter model with $F_y = 0$ (dashed curve) closely follows that of the ideal Stokesian model (dash-dot curve). In the models, the interfacial tension is obtained from Table 6.1 and the viscosity of bitumen is 1246 Pa·s, providing a well-defined characteristic velocity (i.e., no fitting involved).

with divalent calcium ions. However, the surface activity of these complexes is apparently low, since the drop interfacial tension remains unchanged upon addition of calcium ions to the DIW + M system. (The CaM complexes may not be numerous enough to alter the chemical potential and, hence, decrease the interfacial tension.)

As a bitumen drop is extended, CaM complexes adsorb to the freshly created interface. Upon release from a micropipette, the extended drop, whose surface is now saturated with CaM complexes, begins to recover. As the drop recovers, the surface area is compressed, allowing the adsorbed CaM complexes to approach one another. At some point, the CaM complexes come into direct contact. These CaM aggregates may be somewhat compressible or may shear against one another, accounting for the surface dissipation observed in many dynamic experiments. However, they are only compressible to a certain state, possibly when core parts of the aggregates hit each other and they reach a state of maximum compression. At this point, the drop stops recovering even though it is non-spherical, as if the apparent interfacial tension (driving force for recovery) is reduced to zero. Clearly, more work is required to provide further validation for this proposed mechanism. For example, there are some questions as to the formation, and the adsorption nature, of the CaM complexes.

6.4 Conclusions

Novel micropipette techniques have been developed to study the general rheological behaviours of emulsion drop surfaces. These experiments involve micron-scale stress-strain and shape recovery experiments. In the stress-strain (microcantilever) experiments, an individual emulsion drop is elongated and the applied force is measured through the deflection of a microcantilever. In the drop shape recovery experiments, the dynamic recovery of an extended drop is monitored. This is the first study to examine the rheological surface behaviours of bitumen emulsion drops in aqueous environments. Phenomenological evidence is provided to document the plastic surface behaviour and other surface properties of bitumen drops in aqueous environments containing montmorillonite clays and calcium ions. The plastic behaviour of these bitumen drops is described by a lumped parameter model that incorporates a surface stress opposing the action of the interfacial tension and attributes dissipation to the viscosity of bitumen.

Chapter 7

Summary and Recommendations

The material properties of emulsion drops can have significant relevance with regard to fundamental emulsion science. As outlined in the Introduction, the objectives of this research are to develop techniques to explore the mechanical behaviour of individual emulsion drops *in situ* and to quantify their material properties. In realizing these objectives, the main contributions of this study are outlined and recommendations for future study are discussed.

7.1 Summary of Contributions

Novel micro-mechanical techniques are developed to directly explore the *in situ* behaviour of single emulsion drops. As such, phenomena due to the "smallness" of the emulsion drops (e.g., appropriate surface area-to-volume ratio, etc.) are accurately reflected in these unique experiments. Individual emulsion drops are deformed by micron-scale suction pipettes (micropipettes), which are extruded from standard glass capillaries and constructed with a home-made forging apparatus. Using this forging device, micropipettes can be shaped into cantilevers (microcantilevers) that allow for force measurements during a drop deformation experiment.

The equilibrium mechanics of emulsion drops is observed in static stress-strain experiments in which a drop is deformed between a micropipette and a microcantilever. The equilibrium drop shape can be calculated, for a given applied force, using the Young-Laplace equation. In another technique, the shape dynamics of single emulsion drops is monitored (drop shape recovery). Here, an initially spherical drop is extended between two micropipettes, then released from one of the micropipettes, and the time-dependent recovery of the drop is recorded. It is assumed that this recovery process is driven by the tension at the drop surface and rate-limited by the viscosities of the bulk phases. A moving boundary Stokes flow model captures the physics of the recovery process very well. These static (equilibrium) and dynamic micropipette experiments can be used to quantify material properties of emulsion drops *in situ*.

With respect to material property measurements, these novel techniques address limitations of current tensiometers and viscometers. In particular, they are well-suited to evaluate the viscosity of highly dissipative liquids and the interfacial tension between density-matched phases. In these techniques, small drops are deformed via micropipettes and do not rely on gravity for drop deformation (which, in turn, requires density differences between the phases), as most traditional tensiometers do. Due to the length scale of the micropipettes, viscous heating is virtually non-existent in dynamic experiments since the rate of heat conduction is far greater than that for viscous heat generation. Thus, the drop shape recovery technique allows for accurate measurements of extremely high viscosities (~ 10^3 Pa·s)[22].

This is the first measurement of bitumen-water interfacial tension which does not rely on a density difference between the two liquids. The microcantilever technique is used to determine bitumen-water interfacial tension as functions of salt (NaCl) concentration and pH in the aqueous phase. At low salt concentrations, the bitumen drop interfacial tension decreases sharply; it appears to reach an asymptotic value at higher salt concentrations. Bitumen-water interfacial tension decreases with increasing alkalinity (high pH); this is likely due to the release of natural surfactants from the bitumen in such environments. Above pH = 11, the bitumen-water interfacial tension is reduced to a level (~ 1mN/m) that is below the sensitivity of the current microcantilever technique. In this high pH regime, the drop shape recovery technique is ideally-suited for measurement of low interfacial tensions; values as low as 0.08 mN/m are recorded.

Using drop shape recovery, bitumen is found to have a viscosity of ~ 1250 Pa·s at ~ 22°C; viscosity data are obtained in regimes where the interfacial tension is known *a priori* from the microcantilever (static) technique. The dynamic shape recovery technique is the first to provide measurements of bitumen viscosity in which viscous heating is completely negligible.

---

[22] With traditional viscometers, measurement of highly viscous fluids (such as bitumen and polymer melts) is a significant challenge due to viscous heating. These devices must be operated at very low shear rates to minimize such an effect. In fact, bitumen experiences viscous heating on the order of a few degrees centigrade with conventional viscometers (Seyer and Gyte, 1989).

In addition to the measurements of interfacial tension and bulk properties of Newtonian liquids, the micropipette techniques allow one to venture into the study of more complex rheological behaviours of interfaces. The microcantilever technique is extended to incorporate loading-unloading experiments, while drop shape recovery studies can provide additional information on the dynamic behaviour of emulsion drops.

This is the first report detailing the surface plasticity of bitumen drops in aqueous environments that are expected to be detrimental to water-based bitumen extraction operations. The degree of permanent plastic deformation at the bitumen-water interface appears to depend on the maximum deformation of the drop. It is interesting to note that moderately deformed drops show no signs of surface plastic behaviour. Shape recovery studies indicate that surface dissipation is sometimes observed. As an initial attempt to model the plastic behaviour of bitumen drops, a lumped-parameter model is introduced and reasonable agreement with experimental data is obtained. This model incorporates the interfacial tension, bitumen viscosity, and a constant surface stress which opposes the tension. It is suggested that surface plasticity may be attributed to calcium-montmorillonite complexes adsorbed at the drop surface.

7.2 Recommendations for Future Work

In this study, all experiments were conducted at room temperature which, for any given experiment, was observed to vary by as much as ± 0.5°C. Reasonable precision was obtained for interfacial tension measurements (± 1 mN/m). However, some material properties, such as the viscosity, can exhibit significant temperature dependency. Therefore, temperature control would improve the precision of these measurements and may reduce the ~ 7% standard deviation observed in experiments.

Many industrial processes involving emulsions operate at temperatures and pressures that differ from "standard" conditions (i.e., one atmosphere and room temperature). For example, secondary and tertiary oil recovery techniques may involve pressurized flooding of largely depleted oil reservoirs (see Bond, 1974), in which the occurrence of crude oil-water emulsions is very common. Also, although the oil sands industry is tending towards lower temperature extraction, some water-based processes, such as froth dewatering, must still operate at elevated temperatures of ~ 80°C

(Czarnecki, 2001). Therefore, it is important to adapt the micropipette apparatus to study the thermomechanical and pressure-dependent properties of emulsion drops.

Crude oil is extracted from Canadian oil sands by mixing oil sands ore with process water, air and various chemicals. The crude oil considered in the present study is "coker-feed" bitumen. It has been "cleaned" to remove solids etc. in preparation for downstream upgrading processes. As a result, the bitumen used in the present experiments is rather refined relative to the indigenous bitumen found in the oil sands ore. In addition, due to the variable nature of the oil sands ore and indigenous bitumen, a variety of water-soluble species may be released into the process water (which eventually gets recycled). Many of these species may not be reflected in the simulated process water used in this study. (Also, many industrial demulsifying agents are added in commercial oil sands extraction.) Thus, to better represent the emulsions found in water-based oil sands extraction processes, it is imperative that material properties of bitumen drops obtained from oil sands ore be examined in commercial process waters.

In this study, models were introduced to describe the equilibrium and dynamic mechanical behaviours of emulsion drops. These models assumed that the interface was completely characterized by a uniform interfacial tension and that the bulk fluids displayed Newtonian behaviour. However, in other emulsion systems, the fluid and interfacial properties may deviate significantly from these assumptions. For example, latex paints are essentially oil-in-water emulsions (Allyn, 1974). In these dispersions, the oil drops are polymeric liquids, such as poly(vinyl acetate), which will likely exhibit viscoelastic behaviours. In addition, some drop interfaces may be characterized by additional properties, such as surface viscosities. (Recall that surface plastic behaviour of some bitumen emulsion drops was observed in this study.) It is important to develop models that incorporate more complex rheology of the bulk phases and the interface as they play crucial roles in the mechanical behaviour of many emulsion systems. This is a significant theoretical challenge in that the viscoelastic properties of the bulk phases must be coupled to those associated with the drop surface.

Bibliography

Acrivos, A. 1983. The breakup of small drops and bubbles in shear flows. *Ann. N.Y. Acad. Sci.*, **404**, 1-11.

Adamson, A.W. 1976. Physical Chemistry of Surfaces. John Wiley & Sons, New York. pp. 1-6, 47-98.

Allyn, G. 1974. Emulsion paints. In: *Emulsions and Emulsion Technology, Part I* (K.J. Lissant, Ed.). Marcel Dekker, New York. pp. 351-385.

Aveyard, R., Binks, B.P., Cho, W.G., Fisher, L.R., Fletcher, P.D.I. & Klinkhammer, F. 1996. Investigation of the force-distance relationship for a small liquid drop approaching a liquid-liquid interface. *Langmuir*, **12**, 6561-6569.

Bartell, F.E. & Neiderhauser, D.O. 1949. Film-forming constituents of crude petroleum oils. In: *Fundamental Research on Occurrence and Recovery of Petroleum, 1946-1947.* American Institute of Petroleum, New York. pp. 57-80.

Basu, S., Nandakumar, K. & Masliyah, J.H. 1996. A study of oil displacement on model surfaces. *J. Colloid Interface Sci.*, **182**, 82-94.

Bentley, B.J. & Leal, L.G. 1986. An experimental investigation of drop deformation and breakup in steady two-dimensional linear flows. *J. Fluid Mech.*, **167**, 241-283.

Bhardwaj, A. & Hartland, S. 1994. Dynamics of emulsification and demulsification of water in crude oil emulsions. *Ind. Eng.Chem. Res.*, **33**, 1271-1279.

Bird, R.B., Stewart, W.E. & Lightfoot, E.N. 1960. Transport Phenomena. Wiley and Sons, New York. pp. 71-91, 338-342.

Bond, D.C. (Ed.). 1974. Secondary and Tertiary Oil Recovery Processes. Interstate Oil Compact Commission, Oklahoma City, Oklahoma.

Boussinesq, J. 1913. Sur l'existence d'une viscosite superficielle, dans la mince couche de transition separant un liquide d'un autre fluide contigu. *Annales de Chimie et de Physique, Huiteme Serie*, **24**, 349-357; Boussinesq, J. 1913. Application des formules de viscosite superficielle a la surface d'une goutte liquide spherique, tombant lentement, d'un mouvement devenu uniforme, au sein d'une masse fluide indefinie en repos, d'un poids specifique moindre. *Annales de Chimie et de Physique, Huiteme Serie*, **24**, 357-371.

Brown, C.E., Neustadter, E.L. & Whittingham, K.P. 1977. Crude-oil/water interfacial properties – emulsion stability and immiscible displacement, *Enhanced Oil Recovery by Displacement with Saline Solutions*, May 20, London, England. pp. 91-122.

Brown, A.G., Thurman, W.C. & McBain, J.W. 1953. The surface viscosity of detergent solutions as a factor in foam stability. *J. Colloid Sci.*, **8**, 491-507.

Burcik, E.J. & Newman, C. 1957. The surface plasticity of a homologous series of sodium soap solutions. *J. Colloid Sci.*, **12**, 10-18.

Burcik, E.J., Sears, J.R. & Tillotson, A. 1954. The surface plasticity of sodium myristate solutions. *J. Colloid Sci.*, **9**, 281-284.

Cairns, R.J.R., Grist, D.M. & Neustadter, E.L. 1976. The effect of crude oil-water interfacial properties on water-crude oil emulsion stability. In: *Theory and Practice of Emulsion Technology* (A.L. Smith, Ed.). Academic Press, New York, NY. pp. 135-151.

Carriere, C.J., Cohen, A. & Arends, C.B. 1989. Estimation of interfacial tension using shape evolution of short fibers. *J. Rheology*, **33**, 681-689.

Cassis, R., Fuller, N., Hepler, L.G., McLean, R.J.C., Skauge, A., Srinivasan, N.S. and Yan, H. 1985. Specific heat capacities of bitumens and heavy oils, reservoir minerals, clays, dehydrated clays, asphaltenes, and cokes. *AOSTRA J. Res.*, **1**, 163-173.

Cho, K., Jeon, H.K. & Park, C.E. 1996. The effect of end-sulfonated polystyrene on the interfacial tension of nylon-6/polystyrene blends. *Polymer*, **37**, 1117-1122.

Clark, K.A. & Pasternack, D.S. 1932. Hot water separation of bitumen from Alberta bituminous sand. *Ind. Eng. Chem.*, **24**, 1410-1416.

Cohen, A. & Carriere, C.J. 1989. Analysis of a retraction mechanism for imbedded polymeric fibers. *Rheol. Acta*, **28**, 223-232.

Cowles, R.J.H. 2000. Particle characterization for oil sand processing 2: particle size measurements by laser diffraction. *Petr. Sci. Tech.*, **18**, 203-220.

Crandall, S.H., Dahl, N.C. & Lardner, T.J. 1972. An Introduction to the Mechanics of Solids, 2nd Edition. McGraw-Hill, New York.

Czarnecki, J. 2001. Water-in-oil emulsions in recovery of hydrocarbons from oil sands. In: *Encyclopedic Handbook of Emulsion Technology* (J. Sjoblom, Ed.). Marcel Dekker, New York. pp. 497-514.

Dabros, T., Yeung, A., Masliyah, J. & Czarnecki, J. 1999. Emulsification through area contraction. *J. Colloid Interface Sci.*, **210**, 222-224.

Dalgleish, D.G. 1996. Proteins on the surfaces of food emulsions: Adsorption, structure, and emulsion stability. In: *Interfacial Phenomena and Bioproducts* (J.L. Brash and P.W. Wojciechowski, Eds.). Marcel Dekker, New York. pp. 447-483.

Dalgleish, D.G. 2001. Food emulsions. In: *Encyclopedic Handbook of Emulsion Technology* (J. Sjoblom, Ed.). Marcel Dekker, New York. pp. 207-232.

Danov, K.D. 2001. On the viscosity of dilute emulsions. *J. Colloid Interface Sci.*, **235**, 144-149.

Davis, B.W. 1988. Applications to the petroleum industry. In: *Encyclopedia of Emulsion Technology, Volume 3* (P. Becher, Ed.). Marcel Dekker, New York. pp. 307-396.

Dealy, J.M. 1979. Rheological properties of oil sand bitumens. *Can. J. Chem. Eng.*, **57**, 677-683.

Demaison, G.J. 1977. Tar sands and supergiant oil fields. In: *The Oil Sands of Canada-Venezuela 1977, CIM Special Volume 17* (D.A. Redford & A.G. Winestock, Eds.). Canadian Institute of Mining, Metallurgy and Petroleum, Calgary, Canada, pp. 9-16.

Dodd, C.G. 1960. The rheological properties of films at crude petroleum-water interfaces. *J. Phys. Chem.*, **64**, 544-550.

Donahue, D.J. & Bartell, F.E. 1952. The boundary tension at water-organic liquid interfaces. *J. Phys. Chem.*, **56**, 480-484.

Drelich, J., Lelinski, D., Hupka, J. & Miller, J.D. 1995. The role of gas bubbles in bitumen release during oil sand digestion. *Fuel*, **74**, 1150-1155.

Drelich, J. & Miller, J.D. 1994. Surface and interfacial tension of the Whiterocks bitumen and its relationship to bitumen release from tar sands during hot water processing. *Fuel*, **73**, 1504-1510.

Edwards D.A., Brenner H. & Wasan D.T. 1991. Interfacial Transport Processes and Rheology. Butterworth-Heinemann, Massachusetts.

Elemans, P.H.M., Janssen, J.M.H. & Meijer, H.E.H. 1990. The measurement of interfacial tension in polymer/polymer systems: the breaking thread method. *J. Rheology*, **34**, 1311-1325.

Evans, E., Berk, D., Leung, A. 1991. Detachment of agglutinin-bonded red blood cells. *Biophysical J.*, **59**, 838-848.

Evans, E. & Needham, D. 1987. Physical properties of surfactant bilayer membranes: Thermal transitions, elasticity, rigidity, cohesion, and colloidal interactions. *J. Phys. Chem.*, **91**, 4219-4228.

Evans, E., Ritchie, K. & Merkel, R. 1995. Sensitive force technique to probe molecular adhesion and structural linkages at biological interfaces. *Biophysical J.*, **68**, 2580-2587.

Evans, E. & Skalak, R. 1980. Mechanics and Thermodynamics of Biomembranes, CRC, Boca Raton, Fla.

Everett, D.H. 1988. Basic Principles of Colloid Science. Royal Society of Chemistry, London. pp. 30-53, 127-152.

Gahleitner, M. & Sobczak, R. 1988. A new apparatus for measuring high viscosities. *J. Phys. E: Sci. Instrum.*, **21**, 1074-1077.

Grace, H.P. 1982. Dispersion phenomena in high viscosity immiscible fluid systems and application of static mixers as dispersion devices in such systems. *Chem. Eng. Commun.*, **14**, 225-277.

Graham, D.E. 1988. Crude oil emulsions: their stability and resolution. In: *Chemicals in the Oil Industry* (P.H. Ogden, Ed.). Royal Society of Chemistry, London. pp. 155-175.

Green, A.E. & Zerna, W. 1968. Theoretical Elasticity. Dover, New York. pp. 1-50.

Happel, J. & Brenner, H. 1973. Mechanics of Fluids and Transport Processes. Low Reynolds Number Hydrodynamics. Noordhoff Inttemational Publishing, Leyden. pp. 133-138.

Hunter, R.J. 1986. Foundations of Colloid Science, Volume 1. Clarendon Press, Oxford. pp. 1-48, 55-61, 228-315.

Inokuchi, K. 1955. Rheology of surface films. IV. Viscoelastic properties of 6-nylon films at air/water interface. *Bull. Chem. Soc. Japan*, **28**, 453-465.

Isaacs, E.E. & Smolek, K.F. 1983. Interfacial tension behaviour of Athabasca bitumen/aqueous surfactant systems. *Can. J. Chem. Eng.*, **61**, 233-240.

Joly, M. 1972. Rheological properties of monomolecular films. Part I: Basic concepts and experimental methods. Part II. Experimental results. Theoretical interpretation. Applications. In: *Surface and Colloid Science, Volume 5* (E. Matijevic, Ed.). John Wiley & Sons, New York. pp. 1-194.

Jon, D.I., Rosano, H.L. & Cummins, H.Z. 1986. Touluene/water/1-propanol interfacial tension measurements by means of pendant drop, spinning drop, and laser light-scattering methods. *J. Colloid Interface Sci.*, **114**, 330-341.

Jones, T.J., Neustadter, E.L. & Whittingham, K.P. 1978. Water-in-crude oil emulsion stability and emulsion destabilization by chemical demulsifiers. *J. Can. Petr. Tech.*, **17**, 100-108.

Karimi, G.A. and Hanafi, A. 1981. The thermal conductivity of oil sands. *Can. J. Chem. Eng.*, **59**, 461-464.

Kasongo, T., Zhou, Z., Xu, Z. & Masliyah, J. 2000. Effects of clays and calcium ions on bitumen extraction from Athabasca oil sands using flotation. *Can. J. Chem. Eng.*, **78**, 674-681.

Kim, Y.H., Wasan, D.T. & Breen, P.J. 1995. A study of dynamic interfacial mechanisms for demulsification of water-in-oil emulsions. *Colloids Surfaces A*, **95**, 235-247.

Kimbler, O.K., Reed, R.L. & Silberberg, I.H. 1966. Physical characteristics of natural films formed at crude oil-water interfaces. *Soc. Petr. Eng. J.*, **6**, 153-165.

Kobayashi, H., Takahashi, H. & Hiki, Y. 1995. New apparatus for measuring high viscosity of solids. *Int. J. Thermophysics*, **16**, 577-584.

Krawczyk, M.A., Wasan, D.T. & Shetty, C.S. 1991. Chemical demulsification of petroleum emulsions using oil soluble demulsifiers. *Ind. Eng. Chem. Res.*, **30**, 367-375.

Krog, N.J., Riisom, T.H. & Larsson, K. 1985. Applications in the food industry: I. In: *Encyclopedia of Emulsion Technology, Volume 2* (P. Becher, Ed.). Marcel Dekker, New York. pp. 321-365.

Lam, W.W., Tyerman, W.J.R., Payette, C., Miluka, R.J. & Sanford, E.C. 1995. Physical structure of the primary froth from Athabasca oil sand extraction: cryogenic sampling and microscopic observation of pilot plant froths. *Fuel Sci. Tech. Int.*, **13**, 483-508.

LaPlace, P.S. 1805. Sur l'action capillaire. Supplément au Dixième Livre du Traité Mécanique Céleste, Tome quatriéme. Imprimeur-Libraire pour les Mathematiques, quai des Augustins, no. 71. pp. 1-65; LaPlace, P.S. 1966. On capillary attraction. Supplement to the Tenth Book of the Mécanique Céleste, Volume 4 (Translated by N. Bowditch). Chelsea Publishing Company, Bronx, New York. pp. 685-1018.

Lin, S. & Hwang, H. 1994. Measurement of low interfacial tension by pendant drop digitization. *Langmuir*, **10**, 4703-4709.

Liu, J.K. 1989. Analytical methods. In: *AOSTRA Technical Handbook on Oil Sands, Bitumens and Heavy Oils* (L.G. Hepler & C. Hsi, Eds.). AOSTRA, Edmonton, AB. p. 25.

Luciani, A., Champagne, M.F. & Utracki, L.A. 1996. Interfacial tension in polymer blends. Part2: measurements. *Polymer Networks Blends*, **6**, 51-62.

Mankowski, P., Ng, S., Siy, R., Spence, J. & Stapleton, P. 1999. Syncrude's low energy extraction process: commercial implementation. *31st Annual Meeting of the Canadian Mineral Processors*, January 20, Ottawa, Canada. pp. 153-181.

Matsumoto, T. 1974. Emulsion polymerization. In: *Emulsions and Emulsion Technology, Part II* (K.J. Lissant, Ed.). Marcel Dekker, New York. pp. 441-516.

Miller, R., Wustneck, R., Kragel, J. & Kretzschmar, G. 1996. Dilational and shear rheology of adsorption layers at liquid interfaces. *Colloids Surfaces A*, **111**, 75-118.

Mitchell, D.L. and Speight, J.G. 1979. The solubility of asphaltenes in hydrocarbon solvents. *Fuel*, **52**, 149-152.

Mohammed, R.A., Bailey, A.I., Luckham, P.F. & Taylor, S.E. 1993. Dewatering of crude oil emulsions 1. Rheological behaviour of the crude oil-water interface. *Colloids Surfaces A*, **80**, 223-235.

Mohammed, R.A., Bailey, A.I., Luckham, P.F. & Taylor, S.E. 1994. The effect of demulsifiers on the interfacial rheology and emulsion stability of water-in-crude oil emulsions. *Colloids Surfaces A*, **91**, 129-139.

Moran, K., Yeung, A., Czarnecki, J. & Masliyah, J. 2000. Micron-scale tensiometry for studying density-matched and highly viscous fluids – with application to bitumen-in-water emulsions. *Colloids Surfaces A*, **174**, 147-157.

Moran, K., Yeung, A. & Masliyah, J. 1999. Measuring interfacial tensions of micrometer-sized droplets: A novel micromechanical approach. *Langmuir*, **15**, 8497-8504.

Mukherjee, S. & Kushnick, A.P. 1989. Effect of demulsifiers on interfacial properties governing crude oil demulsification. In: *Oil-Field Chemistry Enhanced Recovery and Production Stimulation* (J.K. Borchardt & T.F. Yen, Eds.). American Chemical Society, Washington, D.C. pp. 364-374.

Mulley, B.A. 1974. Medicinal emulsions. In: *Emulsions and Emulsion Technology, Part I* (K.J. Lissant, Ed.). Marcel Dekker, New York. pp. 291-349.

Neustadter, E.L., Whittingham, K.P. & Graham, D.E. 1981. Interfacial rheological properties of crude oil/water systems. In: *Surface Phenomena in Enhanced Oil Recovery* (D.O. Shah, Ed.). Plenum Press, New York. pp. 307-326.

Neustadter, E.L., Whittingham, K.P. & Grist, D.M. 1975. The role of demulsifiers in water/crude oil emulsions, *Proceedings of the International Conference on Colloid and Surface Science*, September 15-20, Budapest, Hungary. pp. 331-337.

Nunez, G.A., Sanchez, G., Gutierrez, X., Silva, F., Dalas, C. & Rivas, H. 2000. Rheological behaviour of concentrated bitumen in water emulsions. *Langmuir*, **16**, 6497-6502.

Oldroyd, J.G. 1955. The effect of interfacial stabilizing films on the elastic and viscous properties of emulsions. *Proc. Royal Soc. London A*, **232**, 567-577.

Overbeek, J.Th.G., Verhoeckx, G.J., De Bruyn, P.L. & Lekkerkerker, H.N.W. 1987. On understanding microemulsions II. Thermodynamics of droplet-type microemulsions. *J. Colloid Interface Sci.*, **119**, 422-441.

Pandit, A., Miller, C.A. & Quintero, L. 1995. Interfacial tensions between bitumen and aqueous surfactant solutions by maximum bubble pressure technique. *Colloids Surfaces A*, **98**, 35-41.

Pasquarelli, C.H. & Wasan, D.T. 1981. The effect of film forming materials on the dynamic interfacial properties in crude oil-aqueous systems. In: *Surface Phenomena in Enhanced Oil Recovery* (D.O. Shah, Ed.). Plenum Press, New York. pp. 237-248.

Pieper, G., Rehage, H. & Barthès-Biesel, D. 1998. Deformation of a capsule in a spinning drop apparatus. *J. Colloid Interface Sci*, **202**, 293-300.

Plateau, J. 1869. Recherches experimentales et theoriques sur les figures d'equilibre d'une masse liquide sans pesanteur, 8^{e} serie. *Annales de Chimie et de Physique, Quatrieme Serie*, **17**, 260-276; Plateau, J. 1869. Experimental and theoretical researches into the figures of equilibrium of a liquid mass without weight, eighth series. *Phil. Mag., Fourth Series*, **38**, 445-455.

Press, W.H., Teukolsky, S.A., Vetterling, W.T. & Flannery, B.P. 1992. Numerical Recipes in Fortran, 2nd Edition. Cambridge University Press, New York. pp. 22-32.

Princen, H.M. 2001. The structure, mechanics, and rheology of concentrated emulsions and fluid foams. In: *Encyclopedic Handbook of Emulsion Technology* (J. Sjoblom, Ed.). Marcel Dekker, New York. pp. 243-278.

Prowse, D.R., Wallace, E.D., Lott, R.K., Dagneault, L.E. and Shelly, N. 1983. Some physical properties of bitumen and oil sand, revision 2. AOSTRA/ARC Joint Oil Sands Research Program. Alberta Research Council, Edmonton, Alberta. pp. 1-23.

Rallison, J.M. 1981. A numerical study of the deformation and burst of a viscous drop in general shear flows. *J. Fluid Mech.*, **109**, 465-482.

Rallison, J.M. 1984. The deformation of small viscous drops and bubbles in shear flows. *Ann. Rev. Fluid Mech.*, **16**, 45-66.

Rallison, J.M. & Acrivos, A. 1978. A numerical study of the deformation and burst of a viscous drop in an extensional flow. *J. Fluid Mech.*, **89**, 191-200.

Reisberg, J. & Doscher, T.M. 1956. Interfacial phenomena in crude-oil-water systems. *Producers Monthly*, **21**, 43-50.

Ruckenstein, E. 1988. Interfacial free energy, surface excess, and stability of macroemulsions. *Langmuir*, **4**, 1318-1321.

Ruhl, W. 1982. Tar (Extra Heavy Oil) Sands and Oil Shales, In: *Geology of Petroleum Volume 6* (H. Beckmann, Ed.). Enke Verlag, Stuttgart, Germany, pp. 1-43.

Salager, J., Briceno, M.I. & Bracho, C.L. 2001. Heavy hydrocarbon emulsions: making use of the state of the art in formulation engineering. In: *Encyclopedic Handbook of Emulsion Technology* (J. Sjoblom, Ed.). Marcel Dekker, New York. pp. 455-495.

Sanford, E.C. & Seyer, F.A. 1979. Processibility of Athabasca tar sand using a batch extraction unit: The role of NaOH. *CIM Bulliten*, **72**, 164-169.

Satherley, J., Girault, H.H.J. & Schiffrin, D.J. 1990. The measurement of ultralow interfacial tension by video digital techniques. *J. Colloid Interface Sci.*, **136**, 574-580.

Schramm, L.L. & Hepler, L.G. 1994. Surface and interfacial tensions of aqueous dispersions of charged colloidal (clay) particles. *Can. J. Chem.*, **72**, 1915-1920.

Schramm, L.L. & Kwak, J.C.T. 1988. The rheological properties of an Athabasca bitumen and some bituminous mixtures and dispersions. *J. Can. Petr. Tech.*, **27**, 26-35.

Schramm, L.L. & Smith, R.G. 1985. The influence of natural surfactants on interfacial charges in the hot-water process for recovering bitumen from the Athabasca oil sands. *Colloids Surfaces*, **14**, 67-85.

Schramm, L.L. & Smith, R.G. 1989. Some parametric studies of oil sand conditioning in the hot water flotation process. *AOSTRA J. Res.*, **5**, 87-107.

Schramm, L.L., Smith, R.G. & Stone, J.A. 1984. The influence of natural surfactant concentration on the hot water process for recovering bitumen from the Athabasca oil sands. *AOSTRA J. Res.*, **1**, 5-13.

Scriven L.E. 1960. Dynamics of a fluid interface: equations of motion for Newtonian surface fluids. *Chem. Eng. Sci.*, **12**, 98-108.

Sears, J.R. 1952. A fundamental investigation of surface viscosity and surface plasticity. M. Petr. Engr. Thesis, University of Oklahoma, Norman, Oklahoma.

Seyer, F.A. & Gyte, C.W. 1989. Viscosity. In: *AOSTRA Technical Handbook on Oil Sands, Bitumens and Heavy Oils* (L.G. Hepler & C. Hsi, Eds.). AOSTRA, Edmonton, AB. pp. 154-184.

Sharma, M.M., Jang, L.K. & Yen, T.F. 1989. Transient interfacial tension behaviour of crude-oil/caustic interfaces. *SPE Res. Eng.*, **4**, 228-236.

Shaw, D.J. 1970. Introduction to Colloid and Surface Chemistry, 2nd Edition. Butterworths, London. pp. 167-186.

Shaw, R.C., Schramm, L.L. & Czarnecki, J. 1996. Suspensions in the hot water flotation process for Canadian oil sands. In: *Suspensions: Fundamentals and Applications in the Petroleum Industry, Advances in Chemistry Series 251* (L.L. Schramm, Ed.). American Chemical Society, Washington, D.C. pp. 639-675.

Sherman, P. 1983. Rheological properties of emulsions. In: *Encyclopedia of Emulsion Technology, Volume 2* (P. Becher, Ed.). Marcel Dekker, New York. pp. 405-437.

Simon, R. & Poynter, W.G. 1968. Down-hole emulsification for improving viscous crude production. *J. Pet. Tech.*, **20**, 1349-1353.

Smith-Magowan, D., Skauge, A. & Hepler, L.G. 1982. Specific heats of Athabasca oil sands and components. *J. Can. Petr. Tech.*, **21**, 28-32.

Son, Y. 2001. Measurement of interfacial tension between polyamide-6 and poly(styrene-*co*-acrylonitrate) by breaking thread method. *Polymer*, **42**, 1287-1291.

Spiegel, M.R. 1991. Mathematical Handbook of Formulas and Tables. McGraw Hill, New York. pp. 146-147.

Stone, H. A. 1994. Dynamics of drop deformation and breakup in viscous fluids. *Ann. Rev. Fluid Mech.*, **26**, 65-102.

Stone, H.A., Bentley, B.J. & Leal, L.G. 1986. An experimental study of the transient effects in the breakup of viscous drops. *J. Fluid Mech.*, **173**, 131-158.

Stone, H.A. & Leal, L.G. 1989a . Relaxation and breakup of an initially extended drop in an otherwise quiescent fluid. *J. Fluid Mech.*, **198**, 399-427.

Stone, H.A. & Leal, L.G. 1989b. A note concerning drop deformation and breakup in biaxial extensional flows at low Reynolds numbers. *J. Colloid Interface Sci.*, **133**, 340-347.

Strassner, J.E. 1968. Effect of pH on interfacial films and stability of crude oil-water emulsions. *J. Petr. Tech.*, **20**, 303-312.

Sukanek, P.C. & Laurence, R.L. 1974. An experimental investigation of viscous heating in some simple shear flows. *AIChE J.*, **20**, 474-484.

Tadros, Th.F. 1994. Fundamental principles of emulsion rheology and their applications. *Colloids Surfaces A*, **91**, 39-55.

Tadros, Th.F. & Vincent, B. 1983a. Emulsion stability. In: *Encyclopedia of Emulsion Technology, Volume 1* (P. Becher, Ed.). Marcel Dekker, New York. pp. 129-287.

Tadros, Th.F. & Vincent, B. 1983b. Liquid/liquid interfaces. In: *Encyclopedia of Emulsion Technology, Volume 1* (P. Becher, Ed.). Marcel Dekker, New York. pp. 1-56.

Takamura, K. 1985. Physico-chemical characterization of Athabasca oil sand and its significance to bitumen recovery. *AOSTRA J. Res.*, **2**, 1-10.

Takamura, K. & Isaacs, E.E. 1989. Interfacial properties. In: *AOSTRA Technical Handbook on Oil Sands, Bitumens and Heavy Oils* (L.G. Hepler & C. Hsi, Eds.). AOSTRA, Edmonton, AB. pp. 100-128.

Taylor, G.I. 1932. The viscosity of a fluid containing small drops of another fluid. *Proc. Royal Soc. London A*, **138**, 41-48.

Taylor, G.I. 1934. The formation of emulsions in definable fields of flow. *Proc. Royal Soc. London* A, **146**, 501-523.

Taylor, G.I. 1964. Conical free surfaces and fluid interfaces. In: *Proc. Intl Congr. Appl. Mech.*, 11th, Munich. pp. 790-796.

Tjahjadi, M., Ottino, J.M. & Stone, H.A. 1994. Estimating interfacial tension via relaxation of drop shapes and filament breakup. *AIChE J.*, **40**, 385-394.

Tjahjadi, M., Stone, H.A. & Ottino, J.M. 1992. Satellite and subsatellite formation in capillary breakup. *J. Fluid Mech.*, **243**, 297-317.

Tran-Son-Tay, R., Needham, D., Yeung, A. & Hochmuth, M. 1991. Time-dependent recovery of passive neutrophils after large deformation. *Biophysics J.*, **60**, 856-866.

Trujillo, E.M. 1983. The static and dynamic interfacial tensions between crude oils and caustic solutions. *Soc. Petr. Eng. J.*, **23**, 645-656.

Verhoeckx, G.J., De Bruyn, P.L. & Overbeek, J.Th.G. 1987. On understanding microemulsions I. Interfacial tensions and adsorptions of SDS and pentanol at the cyclohexane/water interface. *J. Colloid Interface Sci.*, **119**, 409-421.

Walstra, P. 1974. Influence of rheological properties of both phases on droplet size of O/W emulsions obtained by homogenization and similar processes. *Dechema Monograph.*, **77**, 87-94.

Walstra, P. 1993. Principles of emulsion formation. *Chem. Eng. Sci.*, **48**, 333-349.

Ward, S.H. & Clark, K.A. 1950. Determination of the viscosities and specific gravities of the oils in samples of Athabaska bituminous sand. Research Council of Alberta, Report No. 57.

Watkins, V.H. & Hobbs, S.Y. 1993. Determination of the interfacial tensions between BPA polycarbonate and styrene-acrylonitrile copolymers from capillary thread instability measurements. *Polymer*, **34**, 3955-3959.

Whorlow, R.W. 1980. Rheological Techniques. Ellis Horwood, Chichester, UK. pp. 60-114, 115-193, 422-423.

Wilson, P.M.D. & Bradner, C.F. 1977. Aqueous surfactant solutions which exhibit ultralow tensions at the oil-water interface. *J. Colloid Interface Sci.*, **60**, 473-479.

Wilson, R.E. & Ries, E.D. 1923. Surface films as plastic solids. *Colloid Symposium Monograph*, University of Wisconsin Press, Madison, Wisconsin, pp. 145-173.

Yan, N. & Masliyah, J. 1994. The adsorption and desorption of clay particles at the oil-water interface. *J. Colloid Interface Sci.*, **168**, 386-392.

Yeung, A., Dabros, T., Czarnecki, J. & Masliyah, J. 1999. On the interfacial properties of micrometre-sized water droplets in crude oil. *Proc. Royal Soc. London A*, **455**, 3709-3723.

Yeung, A., Dabros, T. & Masliyah, J. 1998. Does equilibrium interfacial tension depend on method of measurement? *J. Colloid Interface Sci*, **208**, 241-247.

Yeung, A. & Pelton, R. 1996. Micromechanics: a new approach to studying the strength and breakup of flocs. *J. Colloid Interface Sci.*, **184**, 579-585.

Young, T. 1805. An essay on the cohesion of fluids. *Phil. Trans. Royal Soc. London*, **95**, 65-87.

Youngren, G.K. & Acrivos, A. 1975. Stokes flow past a particle of arbitrary shape: a numerical method of solution. *J. Fluid Mech.*, **69**, 377-403.

Youngren, G.K. & Acrivos, A. 1976. On the shape of a gas bubble in a viscous extensional flow. *J. Fluid Mech.*, **76**, 433-442.

Zakin, J.L., Pinaire, R. & Borgmeyer, M.E. 1979. Transport of oils as oil-in-water emulsions. *J. Fluids Eng.*, **101**, 100-104.

Appendix A
Thermodynamic Derivation of Equation 2.7

A thermodynamic derivation of the meridional drop curvature R_1^{-1} (equation 2.7) is presented. An emulsion drop, with a radius R_d in free aqueous suspension, is being stretched by two suction pipettes of radii r_1 and r_2 (figure 2.1). Under an axial force f, the drop is elongated to a length L while maintaining its volume (figure 2.1b). This is a reversible (equilibrium) process in which the applied axial load is balanced by the capillary forces at the bitumen-water interface. Without the influence of gravity, and with the two pipettes aligned along a common z axis as shown in figure 2.1, it is clear that the deformed drop will be rotationally symmetric about the same axis. Such a shape can, in general, be characterized by cylindrical coordinates (r, z) as shown in figure 2.1b. The same geometry can alternatively be specified by (s, ϕ), where s is the curvilinear distance (here, measured from $z = 0$) and ϕ is the angle between the surface normal and the axis of symmetry. These two sets of coordinates are interrelated by

$$\frac{\mathrm{d}r}{\mathrm{d}s} = \cos\phi \; ; \qquad \frac{\mathrm{d}z}{\mathrm{d}s} = \sin\phi , \tag{A.1}$$

where r, z and ϕ are implicit functions of s (cf. equations 2.1). When dealing with curved fluid-fluid interfaces, it is also important to quantify the local curvatures. With axisymmetry, the mean curvature J of the drop surface, defined as the sum of the two principal curvatures, is given by

$$J = \frac{\mathrm{d}\phi}{\mathrm{d}s} + \frac{\sin\phi}{r} . \tag{A.2}$$

Consider now an abstraction of the deformed drop as depicted in figure A.1. As the two pipettes in figure 2.1 (including the small drop protrusions inside them) behave effectively as rigid bodies, they are represented as: (a) an immovable wall on the left, corresponding to the reference position $z = 0$, and (b) a piston on the right, through which an axial force f can be exerted. The dashed line in figure A.1 outlines a thermodynamic system consisting of a drop (fluid A), of pressure p_A and volume V_A, and

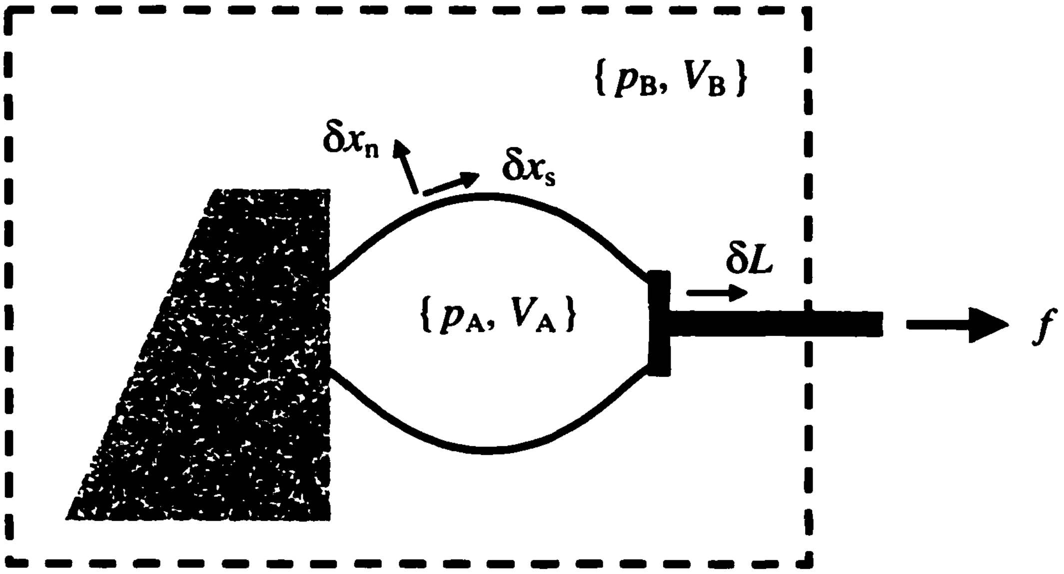

Figure A.1. An abstract representation of a stretched drop. The dashed line outlines a closed system (i.e., one of constant volume) which nevertheless allows external work be done on it through the action of a piston. Here, the drop is elongated by a small amount δL under an external force f; the resulting perturbation in interfacial shape is characterized by δx_n and δx_s. The left-hand side of the drop is anchored to an immovable wall.

the remaining domain, composed of fluid B, with corresponding state variables p_B and V_B. As this represents a general case, the fluids may be regarded as compressible at this stage. Such a system, however, is considered *closed* in that the total volume $V_A + V_B$ must remain constant. (The piston stem is assumed to occupy zero volume.) Nevertheless, mechanical work can still be done on the system via the action of the piston. Let δL be a small displacement of the piston under the external force f; the external work done on the system is therefore

$$\delta w_{\text{ext}} = f \cdot \delta L. \tag{A.3}$$

Owing to the movement of the piston, there will be perturbations of the drop shape. As depicted in figure A.1, the normal and tangential components of the surface displacements are denoted $\delta x_n(s)$ and $\delta x_s(s)$, respectively. These geometric variations in turn lead to small changes in the interfacial area and the two individual volumes, represented here as δA, δV_A and δV_B. Remembering that the total volume of a closed system must be constant, it is necessary that

$$\delta V_A + \delta V_B = 0. \tag{A.4}$$

At constant temperature, the variations δA, δV_A and δV_B will give rise to a small change in the Helmholtz free energy F of the system according to (Hunter, 1986)

$$\delta F = \gamma \cdot \delta A - p_A \cdot \delta V_A - p_B \cdot \delta V_B,$$

where γ is the interfacial tension between bitumen and the surrounding aqueous phase. Using equation A.4, the above expression simplifies to

$$\delta F = \gamma \cdot \delta A - \Delta p \cdot \delta V_A, \tag{A.5}$$

where Δp is defined as $p_A - p_B$. Provided the deformation process in figure A.1 is isothermal ($\mathrm{d}T = 0$), and given that the system is closed [$\delta(V_A + V_B) = 0$], the variation in Helmholtz free energy, δF, must equal the external mechanical work δw_{ext} performed on the system. Combining equations A.3 and A.5, we have

$$f \cdot \delta L = \gamma \cdot \delta A - \Delta p \cdot \delta V_A. \tag{A.6}$$

Equation A.6 expresses equality between the free energy variation δF and the virtual external work δw_{ext}. Continuing, first consider the term $-\Delta p \cdot \delta V_A$ in equation A.6. It is noted that, for small geometric perturbations, the change in volume is the sum of every (elemental area × normal displacement). From figure A.1, it is clear that the variation in volume is $\delta V_A = \pi r_2^2 \cdot \delta L + \int \delta x_n \mathrm{d}A$, and hence

$$-\Delta p \cdot \delta V_A = -\int (\Delta p \cdot \delta x_n)\mathrm{d}A - \pi r_2^2 \Delta p \cdot \delta L. \tag{A.7}$$

Next, the term $\gamma \cdot \delta A$ in equation A.6 is evaluated. Given the general displacement fields $\delta x_n(s)$ and $\delta x_s(s)$, it can be shown, using methods of differential geometry (Green and Zerna, 1968) that every elemental area $\mathrm{d}A$ is dilated by a factor

$$\frac{1}{r}\frac{\mathrm{d}(r\delta x_s)}{\mathrm{d}s} + J\,\delta x_n.$$

The variation in interfacial energy is thus

$$\gamma \cdot \delta A = \int \gamma\left(\frac{1}{r}\frac{\mathrm{d}(r\delta x_s)}{\mathrm{d}s} + J \cdot \delta x_n\right)\mathrm{d}A.$$

Recognizing that, for axisymmetric geometries, an elemental area is given by $\mathrm{d}A = 2\pi r\,\mathrm{d}s$, the above equation can be written as

$$\gamma \cdot \delta A = 2\pi \int \gamma \mathrm{d}(r\delta x_s) + \int (\gamma J \cdot \delta x_n)\mathrm{d}A.$$

Integrating the first term by parts, one has

$$\begin{aligned}\gamma \cdot \delta A &= 2\pi(\gamma r \cdot \delta x_s)_1^2 - 2\pi \int r\delta x_s \frac{\mathrm{d}\gamma}{\mathrm{d}s}\mathrm{d}s + \int (\gamma J \cdot \delta x_n)\mathrm{d}A \\ &= 2\pi(\gamma r \cdot \delta x_s)_1^2 + \int \left(\gamma J \cdot \delta x_n - \frac{\mathrm{d}\gamma}{\mathrm{d}s} \cdot \delta x_s\right)\mathrm{d}A,\end{aligned}$$

where the boundary terms at 1 and 2 correspond to $z = 0$ and $z = L$, respectively. As point 1 is attached to an immovable wall, $(\delta x_s)_1 = 0$. At the other end, $(\delta x_s)_2$ is related to δL through $(\delta x_s)_2 = \delta L \sin\phi_2$, i.e., $(\delta x_s)_2$ is the tangential projection of δL. One therefore has

$$\gamma \cdot \delta A = 2\pi\gamma r_2 \sin\phi_2 \cdot \delta L + \int \left(\gamma J \cdot \delta x_n - \frac{\mathrm{d}\gamma}{\mathrm{d}s} \cdot \delta x_s\right)\mathrm{d}A. \tag{A.8}$$

Substituting equations A.7 and A.8 into equation A.6, one arrives at equation A.9:

$$\left[f + \pi r_2^2 \cdot \Delta p - 2\pi r_2 \sin\phi_2 \cdot \gamma\right] \cdot \delta L - \int \left[(\gamma J - \Delta p) \cdot \delta x_n - \left(\frac{\mathrm{d}\gamma}{\mathrm{d}s}\right) \cdot \delta x_s\right]\mathrm{d}A = 0, \tag{A.9}$$

where the integral is over the entire interfacial surface and ϕ_2 is the angle ϕ at $z = L$. Since the only geometric constraint, up to this point, is the invariance of the total volume $V_A + V_B$, the variations δL, δx_n and δx_s must remain independent and arbitrary; in particular, they may assume any non-zero value. Consequently, to satisfy equation A.9, it is therefore required that

$$f + \pi r_2^2 \cdot \Delta p - 2\pi r_2 \sin\phi_2 \cdot \gamma = 0 \tag{A.10a}$$

$$\Delta p = \gamma J \tag{A.10b}$$

$$\frac{d\gamma}{ds} = 0. \tag{A.10c}$$

Equation A.10c points to the fact that, at thermodynamic equilibrium, no tension gradient can exist on the interfacial plane. Equation A.10b is the familiar Young-Laplace equation (cf. equation 1.1). Note that in the absence of hydrostatic gradients (i.e., at low Bond numbers), the pressure difference Δp across the interface must be uniform over the drop surface. As γ is also uniform (equation A.10c), it follows from the Young-Laplace equation that the elongated drop shape is one of *constant* mean curvature given by the ratio $J = \Delta p / \gamma$. An expression for J can be obtained from equation A.10a, which is a statement of axial force balance at the boundary. By rearranging equation A.10a, one has

$$J = \Delta p / \gamma = \frac{2\sin\phi_2}{r_2} - \frac{f}{\pi r_2^2 \gamma}. \tag{A.11}$$

Combining equations A.11 and A.2, the principal curvature in the s direction R_1^{-1} (equation 2.7) is given by

$$\frac{d\phi}{ds} = \left(\frac{2\sin\phi_2}{r_2} - \frac{f}{\pi r_2^2 \gamma} \right) - \frac{\sin\phi}{r}. \tag{A.12}$$

The second term on the right hand side of equation A.12 is R_2^{-1} (cf. equation 2.2). Equations A.1 and A.12 comprise three ordinary differential equations which specify the deformed drop shape. In practice, they must be solved simultaneously, according to the appropriate boundary conditions, by numerical means (Appendix B).

Appendix B

Axisymmetric Equilibrium Shape Analysis: Numerical Code

In chapter 2, a numerical procedure is required to simultaneously solve equations 2.6 and 2.7. The axisymmetry of the drop is described by equations 2.6, while equation 2.7 is a statement of the Young-Laplace relation (equation 1.1), which expresses the equilibrium mechanics of the drop. In addition to these equations, the drop volume V is tracked, and maintained constant, through the following differential equation

$$\frac{\mathrm{d}V}{\mathrm{d}s} = \pi r^2 \sin\phi; \qquad V(0) = 0. \tag{B.1}$$

In equation B.1, the variables are as defined in figure 2.1b. The numerical code (ds5.m) is written in Matlab (version 5.2) and invokes a shooting method, Runge-Kutta integration and Newton's method (numerically evaluated). The program requires an input of the drop, pipette, and cantilever diameters (in μm) and produces an output files (*.out) containing the dimensionless drop deflection and force values, and the drop contour at a given force.

```
%program ds5.m
%%%%%%%%%%%%%%%%%%%%%%%%%%%%%%%%%%%%%%%%%%%%%%%%%%%%%%%%%
% Theoretical drop shape and drop deflection for an applied force are determined by solving the following
% 5 ODE's, found in ds5eqn.m:
%
%       dt'/ds=2*sin(t)/Rc-f/(pi*Rc^2*s)-sin(t')/r
%       dr/ds=cos(t')
%       dz/ds=sin(t')
%       dA/ds=2*pi*r                                    % additional ODE not required for solution
%       dV/ds=pi*r^2*sin(t')
%
% where t=initial angle, t'=local angle,r=local radius,z=axial position A=area, V=volume, and s=local arc
% length. All variables except t, t' are dimensionless
%
% Variables:
% Dc - cantilever diameter (um)
% Dd - drop diameter (um)
% delta-drop deflection (-)
% Dp - pipette diameter (um)
% f  - applied force (-)
% J  - numerical Jacobian, wrt dt and dsf
% n  - next guess for arc length (sf,ssf) and initial angle (t,tt)
```

```
% R  -  residual vector, calculated in jacob.m
% Rc -  cantilever radius (-) = Dc/Dd
% Rd -  drop radius (-)  = Dd/Dd
% Rp -  dimensionless radius of the pipette, relative to drop diameter
% S  -  arc length output vector (-)
% sf -  end of drop arc, end of integration (-)
% so -  start of drop curve, start of integration (-)
% t  -  drop angle at so (rad)
% t2 -  spherical drop angle at cantilever (rad)
% V  -  initial drop volume (-)
% Y  -  output matrix corresponding to vector S  (Y(:,1)=t, Y(:,2)=r,
%                    Y(:,3)=z, Y(:,4)=A, and Y(:,5)=V)
% yo -  initial conditions vector for integration (y(1)=t,y(2)=Rc,
%                    y(3)=zo,y(4)=A(0),y(5)=V(0))
% zo -  axial length between pipettes when drop is spherical (-)
%
% Requires functions jacob5.m, ds5eqn.m
% Written by Kevin Moran, November 1998, in Matlab 5.2.
%%%%%%%%%%%%%%%%%%%%%%%%%%%%%%%%%%%%%%%%%%%%%%%%%%%%%%%%%%%%%%%%%%%%%%%%%%%%%
global Rp f t m V Rc so sf R

[file,path]=uigetfile('*.DAT','Load Experimental Geometric Data');
if file ~= 0,
        fid = fopen(file,'r');
        G = fscanf(fid,'%g',[2,15]);
        expdata=G';
end

fup=input('Enter the upper limit for dimensionless force :  ');

Dd=input('Enter the drop diameter (um):  ');
Dp=input('Enter the pipette inner diameter (um):  ');
Dc=input('Enter the cantilever inner diameter (um):  ');

Rp=Dp/Dd; Rc=Dc/Dd; Rd=Dd/Dd;                  % scale the input data

R=1;                                           % define residual vector

zo=sqrt((Rd-Rp^2))+sqrt((Rd-Rc^2));            % length between pipettes
t=asin(Rp);                                    % initial guess for angle between pipette and drop
t2=asin(Rc);

V=4/3*pi-pi/3*((cos(t))^3-3*cos(t)+(cos(t2))^3-3*cos(t2)+4);        % Correction to drop volume

j=1;delta(j)=0;F(j)=0;j=2;
tol=1e-8;
so=0; sf=2.5;
sspan=[0;2.5];
options=odeset('AbsTol',1e-8);

step=(fup-0.01)/12;
for f=0.01:step:fup
        while norm(R)>tol
                sspan=[0;sf];
                yo=[t Rp 0 0 0]';
                [S,Y]=ode45('ds5eqn',sspan,yo,options);
```

```
                i=length(Y);
                n=jacob5;                           % new guess for next Newton's method iteration
                sf=n(1);
                t=n(2);
        end

        F(j)=f
        delta(j)=Y(i,3)-zo;

        j=j+1;
        sf=S(i);                                    % initial guess for next force iteration
        t=Y(1,1);                                   % initial guess for next force iteration
        R=1;

end

plot(delta,F); ylabel('Dimensionless Force'); xlabel('delta/Rd')
T=[delta',F'];
YY=[Y(:,3),Y(:,2)];

[file,path]=uiputfile('*.out','Save the Output Data');          % save force-drop deformation data
if file~=0
        eval(['save ',path,file,' T -ascii'])
end

[file,path]=uiputfile('*.txt','Save the Output Data');          % save drop shape contour data (at given f)
if file~=0
        eval(['save ',path,file,' YY -ascii'])
end                                                             % end program
%%%%%%%%%%%%%%%%%%%%%%%%%%%%%%%%%%%%%%%%%%%%%%%%%%%%%%%%%%%%%%%%%%%%%%%%%%%%%%%%%%%%%%%%%%%%%%%


%%%%%%%%%%%%%%%%%%%%%%%%%%%%%%%%%%%%%%%%%%%%%%%%%%%%%%%%%%%%%%%%%%%%%%%%%%%%%%%%%%%%%%%%%%%%%%%
function g=ds5eqn(s,y)
%%%%%%%%%%%%%%%%%%%%%%%%%%%%%%%%%%%%%%%%%%%%%%%%%%%%%%%%%%%%%%%%%%%%%%%%%%%%%%%%%%%%%%%%%%%%%%%
% Calculates the 5 ODE's as required by ds5.m
%
% Variables:
% f - applied force (-)
% Rp - dimensionless radius of the pippette, relative to drop diameter
% t - drop angle at so (rad)
% y - variable's vector (y(1)=t,y(2)=Rc,y(3)=z,y(4)=A,y(5)=V)
%
% Required in program ds5.m
% Written by Kevin Moran, November1998, in Matlab 5.2.
%%%%%%%%%%%%%%%%%%%%%%%%%%%%%%%%%%%%%%%%%%%%%%%%%%%%%%%%%%%%%%%%%%%%%%%%%%%%%%%%%%%%%%%%%%%%%%%
global f Rp t m

g(1)=2*sin(t)/Rp-f/(pi*Rp^2)-sin(y(1))/y(2);
g(2)=cos(y(1));
g(3)=sin(y(1));
g(4)=2*pi*y(2);
g(5)=pi*y(2)^2*sin(y(1));
g=g';
%end subprogram ds5eqn..m
%%%%%%%%%%%%%%%%%%%%%%%%%%%%%%%%%%%%%%%%%%%%%%%%%%%%%%%%%%%%%%%%%%%%%%%%%%%%%%%%%%%%%%%%%%%%%%%
```

```
%%%%%%%%%%%%%%%%%%%%%%%%%%%%%%%%%%%%%%%%%%%%%%%%%%%%%%%%%
function n=jacob5
%%%%%%%%%%%%%%%%%%%%%%%%%%%%%%%%%%%%%%%%%%%%%%%%%%%%%%%%%
% Newton's Method is employed to generate the next guess for the arc length and initial angle of every
% drop. In this program the required Jacobian (ds5eqn2 wrt sf and t) is calculated numerically.
%
% Variables:
% dsf- perturbation of sf (-)
% dt - perturbation of initial angle (rad)
% f - applied force (-)
% J - numerical Jacobian, wrt dt and dsf
% n - next guess for arc length (sf,ssf) and initial angle (t,tt)
% Rr,Rv-Rc and volume residuals (-)
% Rc - cantilever radius (-)
% Rp - dimensionless radius of the pippette, relative to drop diameter
% sf,ssf-end of drop arc, end of integration (-)
% so - start of drop curve, start of integration (-)
% t,tt- drop angle at so (rad)
% V - initial drop volume (-)
%
% Required in function ds5.m, Requires use of function ds5eqn2.m
% Written by Kevin Moran, November 1998, in Matlab 5.2.
%%%%%%%%%%%%%%%%%%%%%%%%%%%%%%%%%%%%%%%%%%%%%%%%%%%%%%%%%
global Rp f t V Rc so sf R; global tt m
dsf=1e-7;dt=1e-7;
tt=ones(1,3);ssf=ones(1,3);Rr=ones(1,3);Rv=ones(1,3);

tt(1)=t; ssf(1)=sf;                                   % initial guesses
options=odeset('AbsTol',1e-8);
for m=1:3
        sspan=[so;ssf(m)];
        yo=[tt(m) Rp 0 0 0]';
        [S,Y]=ode45('ds5eqn2',sspan,yo,options);
        i=length(Y);

        Rr(m)=abs(Y(i,2)-Rc);
        Rv(m)=abs(Y(i,5)-V);

        if m==1
                m=m+1;
                ssf(m)=ssf(m-1)+dsf;
                tt(m)=tt(m-1);
        elseif m==2
                m=m+1;
                tt(m)=tt(m-1)+dt;
                ssf(m)=ssf(m-2);
        end
end

J(1,1)=(Rr(2)-Rr(1))/dsf; J(1,2)=(Rr(3)-Rr(1))/dt;
J(2,1)=(Rv(2)-Rv(1))/dsf; J(2,2)=(Rv(3)-Rv(1))/dt;

R=[Rr(1);Rv(1)];
n=[ssf(1);tt(1)];
n=n-inv(J)*R;                                         %end subprogram jacob5.m
%%%%%%%%%%%%%%%%%%%%%%%%%%%%%%%%%%%%%%%%%%%%%%%%%%%%%%%%%
```

```
%%%%%%%%%%%%%%%%%%%%%%%%%%%%%%%%%%%%%%%%%%%%%
function g=ds5eqn2(s,y)
%%%%%%%%%%%%%%%%%%%%%%%%%%%%%%%%%%%%%%%%%%%%%
% Calculates the 5 ODe's as required for numerical calculation of the Jacobian in jacob5.m within ds5.m
%
% Variables:
%
% f  - applied force (-)
% Rp - dimensionless radius of the pippette, relative to drop diameter
% tt  - drop angle at so (rad)
% y  - variable's vector (y(1)=t,y(2)=Rc,y(3)=z,y(4)=A,y(5)=V)
%
% Required in function jacob5.m
% Written by Kevin Moran, November 1998, in Matlab 5.2.
%%%%%%%%%%%%%%%%%%%%%%%%%%%%%%%%%%%%%%%%%%%%%
global f Rp tt m

g(1)=2*sin(tt(m))/Rp-f/(pi*Rp^2)-sin(y(1))/y(2);
g(2)=cos(y(1));
g(3)=sin(y(1));
g(4)=2*pi*y(2);
g(5)=pi*y(2)^2*sin(y(1));
g=g';
% end subprogram ds5eqn2.m
%%%%%%%%%%%%%%%%%%%%%%%%%%%%%%%%%%%%%%%%%%%%%
```

Appendix C

Calculating the Microcantilever Stiffness

C.1 Description

The stiffness of a microcantilever is given by $k_b = F_0 / \delta_h$, where F_0 is an axial (pulling) force applied at the tip of the cantilever, and δ_h is the resulting horizontal deflection. A mechanical abstraction of the microcantilever pipette is shown in figure C.1. For axial loading, the short segment at the end of the cantilever does not contribute to the overall flexibility and can therefore be neglected when evaluating beam deflections. The remaining L-shaped structure is clamped at point A and supported by a vertical force at B; an axial load F_0, considered a known quantity, is applied at point C. As indicated in figure 2.3, the vertical reaction force at the elbow (point B in figure C.1) results from resting the cantilever elbow on a solid surface. The rigid clamp at A, however, does not exist in reality; it represents a local cross section whose diameter is large enough for the beam to be considered immovable. With regard to axial dimensions, the vertical length L_2 is based on actual design of the cantilever (L_2 is typically 5 to 6 mm). The horizontal length L_1, on the other hand, can be arbitrary as long as the beam diameter at A exceeds ~100μm. This criterion for choosing point A is verified *a posteriori* by the invariance of the beam stiffness for different values of L_1. A free body diagram of the cantilever is shown in figure C.2. The support system, as shown, is statically indeterminate with a redundancy of unity. Here, "redundancy" is the number of supports which can be removed without resulting in collapse of the structure as a rigid body (Crandall et al., 1972). The reaction force F_B, as yet an indeterminate quantity, is required for ensuring zero vertical deflection at B. To prevent rigid body rotation, the bending moment at A must be

$$M_A = F_B L_1 - F_0 L_2. \tag{C.1}$$

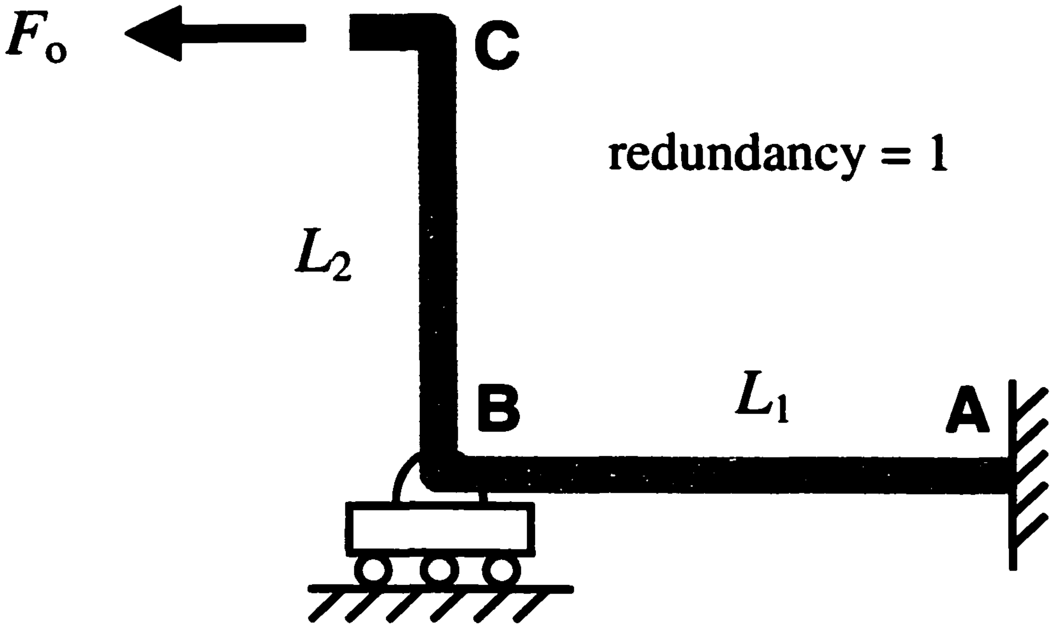

Figure C.1. A mechanical abstraction of the microcantilever (cf. figure 2.3). Although shown here as a uniform beam, the cross section can vary along the axial direction. The support at B represents a vertical reaction force, while F_o is the axial load. The structure, as depicted here, is a statically indeterminate system of redundancy one.

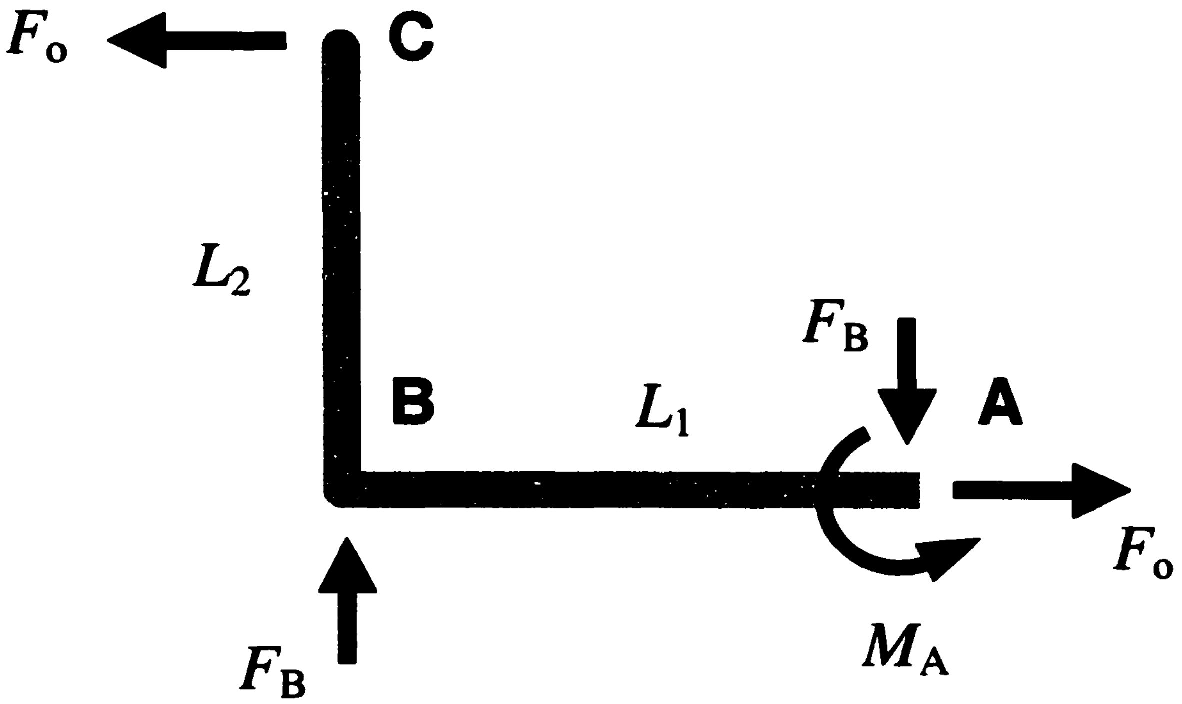

Figure C.2. Free body diagram of the structure shown in figure C.1. F_B is, as yet, an indeterminate force which ensures zero vertical deflection at point B.

Next, the L-shaped structure in figure A.2 is conceptually divided into two straight members of lengths L_1 and L_2 as depicted in figure C.3. The transverse deflections of these straight members, denoted z_1 and z_2, are assumed to be much smaller than their corresponding beam lengths. As such, the familiar moment-curvature relation for slender beams can be applied (Crandall et al., 1972):

$$\frac{d^2 z_i}{d x_i^2} = \frac{M_i}{E I_i}\ ; \quad i = 1, 2. \tag{C.2}$$

M_i and I_i are, respectively, the bending moment (N·m) and moment of inertia (m^4) of member i, and E is the Young's modulus for glass (0.7×10^{11} Pa).

The beam deflections z_i are obtained by integrating equation C.2. In general, both M_i and I_i can vary along the axial directions (i.e., they are functions of x_i). Using free body diagrams, it is easy to show that the bending moments in the two members are

$$\begin{aligned} M_1(x_1) &= F_B L_1 (1 - x_1/L_1) - F_0 L_2 \\ M_2(x_2) &= -F_0 L_2 (1 - x_2/L_2). \end{aligned} \tag{C.3}$$

Note that at the two ends of the microcantilever, we have $M_1(0) = M_A$ and $M_2(L_2) = 0$, as expected. Next, the moment of inertia I of a hollow cylinder (cross section of the cantilever) is given by

$$I = \frac{\pi}{4} r_{out}^4 \left(1 - \beta^4\right); \quad \beta \equiv \frac{r_{in}}{r_{out}}. \tag{C.4}$$

In view of the variable cross section (i.e., tapering) of the cantilever, the value of I will vary considerably along the axial direction. It is a curious observation that, for a tapered capillary formed by heat extrusion, the inner and outer diameters always maintain a constant ratio throughout its entire length – from the initial millimeter-sized tubing down to the micron-sized tip. In this study, the value $\beta = 0.6$ is observed at all cross sections. Finally, to obtain I from equation C.4, it is necessary to know the beam profile, i.e., the variation of the outer diameter $2r_{out}$ along the axial coordinates x_1 and x_2. In practice, beam diameters are measured at discrete locations (typically ten measurements for each straight member) and intermediate values are obtained by cubic spline interpolation. Knowing M_i (in terms of the forces F_0 and F_B; see equation C.3) and I_i (based on the

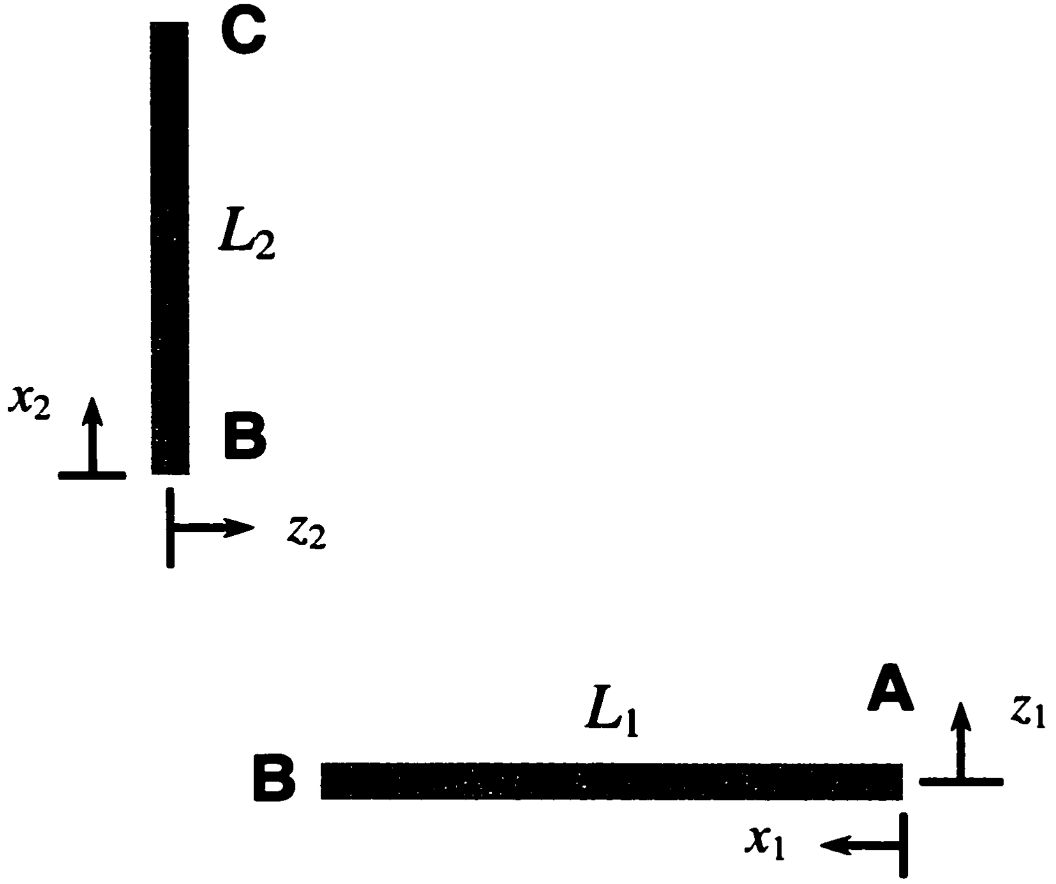

Figure C.3. Dividing the cantilever into two straight members, with coordinates as defined. The moment-curvature relation for slender beams (equation C.2) can now be applied to each individual member for evaluation of deflections.

measured beam profile), equation C.2 can now be integrated numerically. Assuming the clamp at point A and the right-angle elbow at point B are both rigid,[23] initial conditions for the moment-curvature relations are

$$z_1 = 0 \text{ and } \frac{dz_1}{dx_1} = 0 \text{ at } x_1 = 0$$
$$z_2 = 0 \text{ and } \frac{dz_2}{dx_2} = 0 \text{ at } x_2 = 0. \tag{C.5}$$

With these starting conditions, the two moment-curvature relations (equations C.2) are integrated numerically from point A to point B for member 1, and from B to C for member 2. Neglecting terms of second order in the displacements, the horizontal deflection at point C is given by

$$\delta_h = -\left[(z_2)_C + L_2 \left(\frac{dz_1}{dx_1} \right)_B \right], \tag{C.6}$$

while the vertical deflection at B is given by

$$\delta_v = -(z_1)_B. \tag{C.7}$$

Recall the beam deflection problem, as posed, has a redundancy of unity. The indeterminate variable F_B can now be obtained from equation C.7 through an iterative process; i.e., for a prescribed axial force F_0 (which is chosen rather arbitrarily), we find the value F_B which gives a vanishing δ_v. Having satisfied $\delta_v = 0$ at point B, the beam stiffness is finally obtained from the expression

$$k_b = F_0 / \delta_h .$$

The cantilever stiffness is calculated numerically using a Matlab (version 5.2) program (beam2s5.m) that requires geometric dimensions of the microcantilever (diameter at various axial locations). The ordinary differential equations (equation C.2) generated for each beam of the cantilever are contained in subprograms; eqnh2s5.m for the horizontal member L_1 (figure C.1) and eqnvs5.m for the vertical member L_2 (figure C.1).

---

[23] More precisely, a "rigid elbow" means the lines tangent to the two members intersect at 90°.

C.2 Computer Code

```
%%%%%%%%%%%%%%%%%%%%%%%%%%%%%%%%%%%%%%%%%%%%%%%%
% program beam2s5.m
%%%%%%%%%%%%%%%%%%%%%%%%%%%%%%%%%%%%%%%%%%%%%%%%
% Calculates the stiffness (kb) of a cantilever system consisting of two beams of concentric rings with
% tapering diameters. In this case, the "elbow" of the cantilever is resting against a solid support.
% This program:
%       a) requires two input files, 1st column=axial position (mm),
%          2nd column=beam outer diameter (microns)
%       b) approximates the beam profiles through the use of cubic splines
%          introduced in matlab functions eqnh2s5.m and eqnvs5.m
%       c) solves the following ODE's using Runge-Kutta technique (4/5th order):
%
%               d^2(deflection)/(dx)^2 = M/(E*I)
%
%          where I is the moment of inertia and is equal to
%
%               I = PI/4*(outer radius)^4*(1-nu^4)
%
%          and M is the bending moment and is equal to
%
%               M = fb*L1*(1-x/L1)-Mo   for the horizontal beam
%               M =  -Mo*(1-xxv/Lo)     for the vertical beam
%
%       d) requires the use of two Matlab functions, eqnh2s5.m and eqnvs5.m
%          containing the above equations
%
% Variables:
%       a  - ratio of total/maximum vertical to horizontal deflection
%       delh - total/maximum horizontal deflection (cm)
%       delv - maximum vertical deflection, ie. at beam joint (cm)
%       E -  Young's modulus (dyne/cm^2)
%       fb - reaction force as horizontal beam is pressed against wall (dyne)
%       fo - applied force at end of cantilever, @ xxv=Lo (dyne)
%       Lo - length of vertical beam/cantilever (cm)
%       kb - stiffness of cantilever (dyne/cm, mN/m)
%       Mo - moment at stiff end of horizontal beam, @ xxh=0 (dyne/cm)
%       nu - ratio of inner-to-outer diameter of beams
%       rrh - radius of horizontal beam @ xxh (cm)
%       rrv - radius of vertical beam @ xxv (cm)
%       xxh - corrected axial coordinate for horizontal beam (cm)
%       xxv - axial coordinate for vertical beam (cm)
%       Y - col(1) vertical deflection in horizontal beam at position Xh (cm)
%           col(2) slope of deflection in horizontal beam at Xh
%       Z - col(1) horizontal deflection in vertical beam at position Xv (cm)
%           col(2) slope of deflection in vertical beam at Xh
% Written by Kevin Moran, November 1998, in Matlab 5.2.
%%%%%%%%%%%%%%%%%%%%%%%%%%%%%%%%%%%%%%%%%%%%%%%%
global Mo Lo nu E xxh xxv rrh rrv fb L1 j

% Define Constants
fo=1e-4; % applied force (dyne)
nu=0.6;         % ratio of outer-to-inner diameter of cantilever
E=0.7e12;       % Young's modulus for glass (dyne/cm^2)
```

```
% Read beam profile data from two data files
[file,path]=uigetfile('*.txt','Load the Horizontal Beam Data');
if file ~= 0,
        fid = fopen(file,'r');
        F = fscanf(fid,'%g',[2,20]);
        datah=F';
        [file,path]=uigetfile('*.txt','Load the Vertical Beam Data');
        if file ~= 0,
                fid = fopen(file,'r');
                F = fscanf(fid,'%g',[2,20]);
                datav=F';
        end;
end;

% Convert raw data into cgs units and correct axes alignment
        dh=datah(:,2)/1e4; xh=datah(:,1)/10;
        i=length(xh); k=i;
        for j=1:i-1
                xxh(j)=xh(i)-xh(k);
                ddh(j)=dh(k);
                k=k-1;
        end
        xxh(i)=xh(i); ddh(i)=dh(1);

        ddv=datav(:,2)/1e4; xxv=datav(:,1)/10;
        ii=length(xxv); k=ii;


        rrh=ddh/2; rrv=ddv/2;  % Convert diameters to radii

        Lo=xxv(ii);         % length of vertical beam (cantilever)
        L1=xxh(i);          % length of horizontal beam
        Mo=fo*Lo;           % Moment at rigid part of beam one (xxh=0)

% Initial conditions, limits of integration and Implement the Runge-Kutta scheme to solve the ODE's in
% eqnh2s5.m for beam one (horizontal):

        fb=zeros(1,50);v=zeros(1,51);

        j=1; tol=1e-16;   fb(j)=0.5*fo; v(j)=-1e-6;
        xho=0; xhf=xxh(i);xs=[xho;xhf];
        odetol=odeset('RelTol',1e-8);
        yo=[0 0]';
        while abs(v(j))>tol
                [Xh,Y]=ode45('eqnh2s5',xs,yo,odetol);
                i=length(Y);
                j=j+1;
                v(j)=Y(i,1);
                b=v(j)*v(j-1);
                if b<0
                        j=j-2;
                        break
                end
                fb(j)=fb(j-1)+0.02*fo;
        end
```

```
        while abs(Y(i,1))>tol
                j=j+1;
                fb(j)=fb(j-1)-v(j)/((v(j)-v(j-1))/(fb(j-1)-fb(j-2)));
                [Xh,Y]=ode45(‘eqnh2s5’,xs,yo,odetol);
                i=length(Y);
                v(j+1)=Y(i,1);
        end

% Initial conditions, limits of integration and Implement the Runge-Kutta scheme to solve the ODE's in
% eqnvs5.m for beam two (vertical):

        xvo=0; xvf=xxv(ii); zo=[0 0]';xsv=[xvo;xxv(ii)];
        [Xv,Z]=ode45(‘eqnvs5’,xsv,zo,odetol);
        ii=length(Z);

% Calculate the horizontal deflection (cm)

        delh=-(Z(ii,1)+Lo*Y(i,2));

% Calculate the vertical deflection (cm)

        delv=-Y(i,1);

% Find the beam constant/stiffness (kb - dyne/cm, nN/um)

        kb=fo/delh;

% Find the ratio of vertical to horizontal deflection (a)

        a=delv/delh;

% end program
%%%%%%%%%%%%%%%%%%%%%%%%%%%%%%%%%%%%%%%%%%%%%%%%%%%%%%%%%%%%%%%%%%%%%%
```

```
%%%%%%%%%%%%%%%%%%%%%%%%%%%%%%%%%%%%%%%%%%%%%%%%%%%%
function f=eqnh2s5(x,y)
%%%%%%%%%%%%%%%%%%%%%%%%%%%%%%%%%%%%%%%%%%%%%%%%%%%%
% This function evaluates a set of ordinary differential equations required for a horizontal beam. Here
% f represents the first differential of y with respect to axial position. To be used with beam2s5.m and
% ode45.m or ode23.m. The outer radius of the horizontal beam is approximated through a cubic spline,
% evaluated at x. In this case the "elbow" of the cantilever is resting against a solid support.
%
% The second order differential equation to be solved is:
%
%                  d^2(Y)/(dx)^2 = M/(E*I)
%           where I is the moment of inertia and is equal to
%                  I = PI/4*(outer radius)^4*(1-nu^4)
%           and M is the bending moment and is equal to
%                  M = fb*L1*(1-x/L1)-Mo
%
% Variables:
%
%        E - Young's modulus (dyne/cm^2)
%        Lo - length of vertical beam/cantilever (cm)
%        Mo - moment at stiff end of horizontal beam, @ xxh=0 (dyne/cm)
%        nu - ratio of inner-to-outer diameter of beams
%        r  - outer radius of horizontal beam at x
%        rrh - outer radius of beam at position xxh (cm)
%        x - axial position (cm)
%        xxh - axial position, for use with rrh (cm)
%        y - vertical deflection at x (cm)

% Required in program beam2s5.m
% Written by Kevin Moran, November1998, in Matlab 5.2.
%%%%%%%%%%%%%%%%%%%%%%%%%%%%%%%%%%%%%%%%%%%%%%%%%%%%
global Mo xxh rrh nu E fb L1 j

r=spline(xxh,rrh,x); % outer radius of beam at position xxh
PI=3.141592653589793;

% Definition of the individual equations of the set of ODE's
f(1)=y(2);
f(2)=(fb(j)*L1*(1-x/L1)-Mo)/(E*PI/4*r^4*(1-nu^4));
f=f';
% end subprogram
%%%%%%%%%%%%%%%%%%%%%%%%%%%%%%%%%%%%%%%%%%%%%%%%%%%%
```

```
%%%%%%%%%%%%%%%%%%%%%%%%%%%%%%%%%%%%%%%%%%%%%%%%%%%%%%%%%%
function g=eqnvs5(w,z)
%%%%%%%%%%%%%%%%%%%%%%%%%%%%%%%%%%%%%%%%%%%%%%%%%%%%%%%%%%
% This function evaluates a set of ordinary differential equations required for a vertical beam.  Here
% g represents the first differential of z with respect to axial position.  To be used with beam2s5.m and
% ode45.m.  The outer radius of the vertical beam is approximated through a cubic spline, evaluated at w.
%
% The second order differential equation to be solved is:
%
%                   d^2(Z)/(dw)^2 = M/(E*I)
%          where I is the moment of inertia and is equal to
%                   I = PI/4*(outer radius)^4*(1-nu^4)
%          and M is the bending moment and is equal to
%                   M =  -Mo*(1-w/Lo)
% Variables:
%
%        E -  Young's modulus (dyne/cm^2)
%        Lo - length of vertical beam/cantilever (cm)
%        Mo - moment at stiff end of horizontal beam, @ xxh=0 (dyne/cm)
%        nu - ratio of inner-to-outer diameter of beams
%        q  - outer radius of horizontal beam at w (cm)
%        rrv - radius of vertical beam at xxv (cm)
%        w - axial position (cm)
%        xxv - axial position, to be used with rrv (cm)
%        z - horizontal deflection of vertical beam at w (cm)
%
% Required in program beam2s5.m
% Written by Kevin Moran, November1998, in Matlab 5.2.
%%%%%%%%%%%%%%%%%%%%%%%%%%%%%%%%%%%%%%%%%%%%%%%%%%%%%%%%%%
global Mo xxv rrv Lo nu E

q=spline(xxv,rrv,w);          % outer radius of beam at position xxv
PI=3.141592653589793;

% Definition of the individual equations of the set of ODE's

g(1)=z(2);
g(2)=-Mo*(1-w/Lo)/(E*PI/4*q^4*(1-nu^4));
g=g';
% end subprogram
%%%%%%%%%%%%%%%%%%%%%%%%%%%%%%%%%%%%%%%%%%%%%%%%%%%%%%%%%%
```

Appendix D

Calculating the Mean Curvature *J* and Transformation Angle ψ.

D.1 Local Drop Curvature *J*

In describing the mechanics of drops, the local curvature is important as evident in the Young-Laplace relation (Young, 1805; Laplace, 1806; see equation 1.1). In the Stokesian model discussed in chapter 4, numerical evaluation of the local curvature J is required. In the following, a simple method to represent the curvature in terms of the curvilinear coordinates (r, z, s; see figure 4.1) at any location is described through geometric derivatives of the drop shape.

First, note that the drop curvature J may be represented in general by

$$J = \frac{1}{R_1} + \frac{1}{R_2}, \tag{D.1}$$

in which R_1 and R_2 are the principal radii of curvature in the meridional and azimuthal directions for an axisymmetric shape. As noted in chapter 2, these principal radii of curvature can be expressed in terms of curvilinear geometry (cf. equations 2.2). These equations are rewritten here for clarity,

$$\frac{1}{R_1} = \frac{\mathrm{d}\phi}{\mathrm{d}s}; \qquad \frac{1}{R_2} = \frac{\sin\phi}{r}. \tag{D.2}$$

In this representation, the angle ϕ is that between the axis of symmetry (z axis) and a vector normal to the drop surface at curvilinear distance s (figure 4.1). This angle is expressed, in terms of trigonometric functions, as derivatives of the local drop geometry:

$$\cos\phi = \frac{\mathrm{d}r}{\mathrm{d}s}; \qquad \sin\phi = \frac{\mathrm{d}z}{\mathrm{d}s}. \tag{D.3}$$

Although an appropriate form for the radius of curvature R_2 is readily available from the second of these equations, further derivation is still required to give R_1 (cf. the first of equations D.2). Note that derivatives of equations D.3 with respect to s give

$$-\sin\phi\cdot\frac{d\phi}{ds} = \frac{d^2r}{ds^2}; \qquad \cos\phi\cdot\frac{d\phi}{ds} = \frac{d^2z}{ds^2}. \tag{D.4a,b}$$

Now, by multiplying equation D.4a by ($-\sin\phi$), equation D.4b by ($\cos\phi$), and summing these products, one arrives at

$$\left(\cos^2\phi+\sin^2\phi\right)\cdot\frac{d\phi}{ds} = \cos\phi\cdot\frac{d^2z}{ds^2} - \sin\phi\cdot\frac{d^2r}{ds^2}. \tag{D.5}$$

Recalling equations D.3 and the trigonometric identity $\cos^2\phi + \sin^2\phi = 1$, the following relation for radius of curvature R_1 is obtained

$$\frac{1}{R_1} = \frac{dr}{ds}\cdot\frac{d^2z}{ds^2} - \frac{dz}{ds}\cdot\frac{d^2r}{ds^2}, \tag{D.6}$$

such that the local curvature at any point on an axisymmetric drop surface is given by

$$J = \frac{dr}{ds}\cdot\frac{d^2z}{ds^2} - \frac{dz}{ds}\cdot\frac{d^2r}{ds^2} + \frac{1}{r}\cdot\frac{dz}{ds}. \tag{D.7}$$

In equation D.7, the first two terms on the right hand side represent $1/R_1$ and the last term gives the azimuthal curvature $1/R_2$.

Equation D.7 allows for the evaluation of the local drop curvature in terms of the geometric variables r, z, and s. For numerical calculations, however, the derivatives must be represented by finite difference equations. In the present analysis, the following finite difference formulas, at the i^{th} nodal point, are used

$$\left(\frac{dg}{ds}\right)_i \approx \frac{1}{2}\cdot\left(\frac{\Delta g_{i+1}}{\Delta s_{i+1}} + \frac{\Delta g_i}{\Delta s_i}\right),$$

$$\left(\frac{d^2g}{ds^2}\right)_i \approx \frac{2}{\left(\Delta s_{i+1}+\Delta s_i\right)}\cdot\left(\frac{\Delta g_{i+1}}{\Delta s_{i+1}} - \frac{\Delta g_i}{\Delta s_i}\right), \tag{D.8}$$

in which g represents the appropriate dependent variable (r, z), $\Delta g_i = (g_i - g_{i-1})$ and $\Delta s_i = (s_i - s_{i-1})$. In this manner, the local drop curvature (equation D.7) is calculated in the boundary least squares analysis of the Stokesian model described in chapter 4.

D.2 Transformation Angle ψ

The transformation angle ψ is defined as that between the R coordinate and a vector normal to the drop surface at curvilinear location s (figure 4.1). This angle is important to the Stokesian model as it describes the transformation required to represent both the capillary stresses and the hydrodynamic stresses at any arbitrary drop surface in spherical coordinates (R, θ). In this model, it is desired to give trigonometric functions of ψ in terms of the curvilinear coordinates (r, z, s) for use in equations 4.3 and 4.5.

The angle ϕ is represented above with trigonometric functions in terms of the desired curvilinear coordinates (equations D.3). In a similar fashion, the spherical coordinate θ (figure 4.1) may be given by

$$\cos\theta = \frac{z}{\sqrt{r^2 + z^2}}; \qquad \sin\theta = \frac{r}{\sqrt{r^2 + z^2}}, \tag{D.9}$$

where the denominator is an expression of the spherical coordinate R (figure 4.1).

The angle ψ may be described in terms of the other two angles previously discussed, ϕ and θ, using trigonometric addition formulae such that

$$\begin{aligned} \cos\psi &= \sin\phi \cdot \sin\theta - \cos\phi \cdot \cos\theta; \\ \sin\psi &= \sin\phi \cdot \cos\theta + \cos\phi \cdot \sin\theta, \end{aligned} \tag{D.10}$$

noting that $\psi = \Pi - (\phi + \theta)$. Invoking equations D.3 and equations D.9 allows for equations D.10 to be represented in terms of the desired curvilinear coordinates, giving

$$\begin{aligned} \cos\psi &= \frac{1}{\sqrt{r^2 + z^2}} \cdot \left(r \cdot \frac{dz}{ds} - z \cdot \frac{dr}{ds} \right); \\ \sin\psi &= \frac{1}{\sqrt{r^2 + z^2}} \cdot \left(z \cdot \frac{dz}{ds} + r \cdot \frac{dr}{ds} \right). \end{aligned} \tag{D.11}$$

The geometric derivatives in the above equations are handled numerically using the appropriate finite difference formula (equations D.8). In this study, equations D.11 are used in the evaluation of the stresses at any point (r, z) on the drop surface in the boundary least squares analysis of the Stokesian model.

Appendix E

Variational Solution to the Stokesian Model

The Stokesian model described in chapter 4 involves evaluating series solutions for the velocity and pressure fields within the drop by optimizing the series coefficients. In such an analysis, the partial derivative of an error functional (equation 4.9) is expanded in a first order Taylor series to give

$$\frac{\partial\varepsilon}{\partial a_i} \approx \left(\frac{\partial\varepsilon}{\partial a_i}\right)_o + \left(\frac{\partial^2\varepsilon}{\partial a_i\partial a_j}\right)\cdot a_j = 0, \tag{E.1}$$

where, for simplicity, the first partial derivative is evaluated at $\{a\} = 0$. As these equations represent a linear system, an iterative procedure is not required and the optimized coefficients a_j will result upon inverting equations E.1. As such, the partial derivatives given in equations E.1 may be expressed, directly from equations 4.9 as

$$\left(\frac{\partial\varepsilon}{\partial a_i}\right)_o = 2\int\left[T_R\cdot\frac{\partial(\sigma_R-\bar{\sigma}_R)}{\partial a_i}+T_\theta\cdot\frac{\partial(\sigma_\theta-\bar{\sigma}_\theta)}{\partial a_i}\right]r\,ds, \tag{E.2}$$

and

$$\frac{\partial^2\varepsilon}{\partial a_i\partial a_j} = 2\int\left[\begin{array}{c}\dfrac{\partial(\sigma_R-\bar{\sigma}_R)}{\partial a_i}\cdot\dfrac{\partial(\sigma_R-\bar{\sigma}_R)}{\partial a_j}+\dfrac{\partial(\sigma_\theta-\bar{\sigma}_\theta)}{\partial a_i}\cdot\dfrac{\partial(\sigma_\theta-\bar{\sigma}_\theta)}{\partial a_j}\\ +\dfrac{\partial(u_R-\bar{u}_R)}{\partial a_i}\cdot\dfrac{\partial(u_R-\bar{u}_R)}{\partial a_j}+\dfrac{\partial(u_\theta-\bar{u}_\theta)}{\partial a_i}\cdot\dfrac{\partial(u_\theta-\bar{u}_\theta)}{\partial a_j}\end{array}\right]r\,ds = 0. \tag{E.3}$$

The individual terms in the above equations are, with the exception of the capillary stress terms (T_R, T_θ; see equations 4.3), functions of the coefficient set $a_n = \{\Pi, B_2, C_2, D_2, A_n, B_n, C_n, D_n\}$, for $n > 2$. These coefficients are implicit to the velocity and pressure field series solutions (equations 4.6 and 4.7). Each of the partial derivative terms in equations E.2 and E.3 are now expanded in terms of this coefficient set. In the following, these derivatives will be presented in groups according to the coefficient in which the derivation is respect to, beginning with Π.

Partial derivatives with respect to Π

$$\frac{\partial(\sigma_R - \bar{\sigma}_R)}{\partial \Pi} = -\cos\psi \tag{E.4a}$$

$$\frac{\partial(\sigma_\theta - \bar{\sigma}_\theta)}{\partial \Pi} = -\sin\psi \tag{E.4b}$$

$$\frac{\partial(u_R - \bar{u}_R)}{\partial \Pi} = 0 \tag{E.4c}$$

$$\frac{\partial(u_\theta - \bar{u}_\theta)}{\partial \Pi} = 0 \tag{E.4d}$$

Partial derivatives with respect to B_2

$$\frac{\partial(\sigma_R - \bar{\sigma}_R)}{\partial B_2} = -3\bar{\mu}R^{-4}\cdot[2\cos\theta\cdot\cos\psi + \sin\theta\cdot \sin\psi] \tag{E.5a}$$

$$\frac{\partial(\sigma_\theta - \bar{\sigma}_\theta)}{\partial B_2} = 3\bar{\mu}R^{-4}\cdot[\cos\theta\cdot\sin\psi - \sin\theta\cdot\cos\psi] \tag{E.5b}$$

$$\frac{\partial(u_R - \bar{u}_R)}{\partial B_2} = R^{-3}\cos\theta \tag{E.5c}$$

$$\frac{\partial(u_\theta - \bar{u}_\theta)}{\partial B_2} = \frac{R^{-3}}{2}\cdot\sin\theta \tag{E.5d}$$

Partial derivatives with respect to C_2

$$\frac{\partial(\sigma_R - \bar{\sigma}_R)}{\partial C_2} = 3\mu R[2\cos\theta \cdot \cos\psi + \sin\theta \cdot sin\psi] \tag{E.6a}$$

$$\frac{\partial(\sigma_\theta - \bar{\sigma}_\theta)}{\partial C_2} = 3\mu R \cdot [sin\theta \cdot \cos\psi - \cos\theta \cdot \sin\psi] \tag{E.6b}$$

$$\frac{\partial(u_R - \bar{u}_R)}{\partial C_2} = -R^{-2}\cos\theta \tag{E.6c}$$

$$\frac{\partial(u_\theta - \bar{u}_\theta)}{\partial C_2} = 2R^2\sin\theta \tag{E.6d}$$

Partial derivatives with respect to D_2

$$\frac{\partial(\sigma_R - \bar{\sigma}_R)}{\partial D_2} = -3\bar{\mu}R^{-2}\cos\theta \cdot \cos\psi \tag{E.7a}$$

$$\frac{\partial(\sigma_\theta - \bar{\sigma}_\theta)}{\partial D_2} = 0 \tag{E.7b}$$

$$\frac{\partial(u_R - \bar{u}_R)}{\partial D_2} = R^{-1}\cos\theta \tag{E.7c}$$

$$\frac{\partial(u_\theta - \bar{u}_\theta)}{\partial D_2} = -\frac{R^{-1}}{2} \cdot sin\theta \tag{E.7d}$$

Partial derivatives with respect to A_n, $n > 2$

$$\frac{\partial(\sigma_R - \bar{\sigma}_R)}{\partial A_n} = 2\mu R^{n-3} \cdot \left[n(n-2) \cdot \frac{I_n}{\sin\theta} \cdot \sin\psi - (n-2)P_{n-1} \cdot \cos\psi \right] \qquad \text{(E.8a)}$$

$$\frac{\partial(\sigma_\theta - \bar{\sigma}_\theta)}{\partial A_n} = 2\mu R^{n-3} \cdot$$

$$\left[n(n-2) \cdot \frac{I_n}{\sin\theta} \cdot \cos\psi - \left((n-1) \cdot P_{n-1} - n\left(\frac{I_n \cdot \cos\theta}{1-\cos^2\theta} \right) \right) R^{n-1} \cdot \sin\psi \right] \qquad \text{(E.8b)}$$

$$\frac{\partial(u_R - \bar{u}_R)}{\partial A_n} = -R^{n-2} \cdot P_{n-1} \qquad \text{(E.8c)}$$

$$\frac{\partial(u_\theta - \bar{u}_\theta)}{\partial A_n} = nR^{n-2} \cdot \frac{I_n}{\sin\theta} \qquad \text{(E.8d)}$$

Partial derivatives with respect to B_n, $n > 2$

$$\frac{\partial(\sigma_R - \bar{\sigma}_R)}{\partial B_n} = -2\bar{\mu} R^{-n-2} \cdot \left[(n+1) \cdot P_{n-1} \cdot \cos\psi + (n^2-1) \cdot \frac{I_n}{\sin\theta} \right] \qquad \text{(E.9a)}$$

$$\frac{\partial(\sigma_\theta - \bar{\sigma}_\theta)}{\partial B_n} = 2\bar{\mu} R^{-n-2} \cdot$$

$$\left[\left(nP_{n-1} - (n-1) \cdot \frac{I_n \cdot \cos\theta}{1-\cos^2\theta} \right) \cdot \sin\psi - (n^2-1) \cdot \frac{I_n}{\sin\theta} \cdot \cos\psi \right] \qquad \text{(E.9b)}$$

$$\frac{\partial(u_R - \bar{u}_R)}{\partial B_n} = R^{-n-1} \cdot P_{n-1} \qquad \text{(E.9c)}$$

$$\frac{\partial(u_\theta - \bar{u}_\theta)}{\partial B_n} = (n-1)R^{-n-1} \cdot \frac{I_n}{\sin\theta} \qquad \text{(E.9d)}$$

Partial derivatives with respect to C_n, $n > 2$

$$\frac{\partial(\sigma_R - \bar{\sigma}_R)}{\partial C_n} = -2\mu R^{n-1} \cdot \left[(n^2 - 1) \cdot \frac{I_n}{\sin\theta} \cdot \sin\psi - \frac{n^2 - 3n - 1}{n - 1} \cdot P_{n-1} \cdot \cos\psi \right] \quad \text{(E.10a)}$$

$$\frac{\partial(\sigma_\theta - \bar{\sigma}_\theta)}{\partial C_n} = 2\mu R^{n-1} \cdot$$

$$\left[(n^2 - 1) \cdot \frac{I_n}{\sin\theta} \cdot \cos\psi + \left(\frac{n(n+2)}{n-1} \cdot P_{n-1} - (n+2) \cdot \frac{I_n \cdot \cos\theta}{1 - \cos^2\theta} \right) \cdot \sin\psi \right] \quad \text{(E.10b)}$$

$$\frac{\partial(u_R - \bar{u}_R)}{\partial C_n} = -R^n \cdot P_{n-1} \quad \text{(E.10c)}$$

$$\frac{\partial(u_\theta - \bar{u}_\theta)}{\partial C_n} = (n+2) \cdot R^{n-2} \cdot \frac{I_n}{\sin\theta} \quad \text{(E.10d)}$$

Partial derivatives with respect to D_n, $n > 2$

$$\frac{\partial(\sigma_R - \bar{\sigma}_R)}{\partial D_n} = -2\bar{\mu} R^{-n} \cdot \left[\frac{n^2 + n - 3}{n} \cdot P_{n-1} \cdot \cos\psi + n\,(n-2) \cdot \frac{I_n}{\sin\theta} \cdot \sin\psi \right] \quad \text{(E.11a)}$$

$$\frac{\partial(\sigma_\theta - \bar{\sigma}_\theta)}{\partial D_n} = 2\bar{\mu} R^{-n} \cdot$$

$$\left[(n-3) \cdot \left(\frac{n-1}{n} \cdot P_{n-1} - \frac{I_n \cdot \cos\theta}{1 - \cos^2\theta} \right) \cdot \sin\psi - n(n-2) \cdot \frac{I_n}{\sin\theta} \cdot \cos\psi \right] \quad \text{(E.11b)}$$

$$\frac{\partial(u_R - \bar{u}_R)}{\partial D_n} = R^{-n+1} \cdot P_{n-1} \quad \text{(E.11c)}$$

$$\frac{\partial(u_\theta - \bar{u}_\theta)}{\partial D_n} = (n-3) \cdot R^{-n-1} \cdot \frac{I_n}{\sin\theta} \quad \text{(E.11d)}$$

In the partial derivatives (equations E.4 to E.11), all variables are as defined in chapter 4. The Legendre polynomials (of the first kind) P_{n-1} in these equations are in terms of $\cos\theta$, such that $P_1 = \cos\theta$, $P_2 = (1/4)\cdot(1+3\cos(2\theta))$, etc. These functions are evaluated using the following recurrence formula (Spiegel, 1991)

$$(n+1)\cdot P_{n+1} + nP_{n-1} = (2n+1)\cdot\cos\theta\cdot P_n . \qquad \text{(E.12)}$$

As such, any Legendre polynomial at $n+1$ in the series may be computed from known values at n and $n-1$. The Gegenbauer functions (of the first kind) I_n appearing in the partial derivatives (equations E.8 to E.11) can be deduced from the corresponding Legendre polynomials since (Happel and Brenner, 1973)

$$I_n = \frac{P_{n-2} - P_n}{2n-1} . \qquad \text{(E.13)}$$

The boundary least squares analysis is used to optimize the series coefficients a_n to solve the moving boundary Stokesian model describing the recovery of an axisymmetrically elongated drop. The numerical code is presented in Appendix F.

Appendix F

Boundary Least Squares Analysis: Numerical Code

In chapter 4, a variational technique is used to numerically solve a moving boundary Stokesian model describing the recovery of an axisymmetrically stretched emulsion drop. The boundary least squares method, outlined in detail in Appendix E, involves inverting a linear system of equations (equations E.1) to optimize unknown coefficients in exact series solutions to the Stokesian model. The numerical code, written in Visual Fortran, is presented in this Appendix. A "canned" routine (subroutine "gaussj") is implemented to ultimately solve equations E.1 by Gauss-Jordan elimination techniques (Press et al., 1992).

```
!!!!!!!!!!!!!!!!!!!!!!!!!!!!!!!!!!!!!!!!!!!!!!!!!!!!!!!!!!!!!!!!!!!!!!!!!!!!!!!!!!!!!!!!!!!!!!!!!!!!!!!!!!!!!!!!!!!!!!!!!!!
PROGRAM viscio
!!!!!!!!!!!!!!!!!!!!!!!!!!!!!!!!!!!!!!!!!!!!!!!!!!!!!!!!!!!!!!!!!!!!!!!!!!!!!!!!!!!!!!!!!!!!!!!!!!!!!!!!!!!!!!!!!!!!!!!!!!!
      IMPLICIT REAL*8 (a-h,o-z)
      DIMENSION z(200),r(200),s(200),RR(200), P(100),G(100),
  *   dPRb(200),dPTb(200),deo(200),sdeo(200),Tdeo(200),d2e(200,200),
  *   sd2e(200,200),Td2e(400,400),vr(200),vz(200),A(200),D(3201),
  *   TT(3201),dvR(200),dvT(200),DJ(200)
      INTEGER i,j,l,m,n
      REAL*8 t,dr,dz,d2r,d2z,CJ,st,ct,sp,cp,V,pi,dt,MIU,Min

      OPEN(unit=3,file='iscigar.txt',status='old')  ! input file describing the initial shape of the drop
      OPEN (UNIT=7, FILE='ltcig.txt', STATUS='UNKNOWN')
      OPEN (UNIT=9, FILE='zrcig.txt', STATUS='UNKNOWN')

      PRINT *,'ENTER FINAL TIME '
      READ *,tf

      MIU=0.1d0 !0.1d0                          ! outer viscosity
      Min=1.d0 !0.01d0                          ! inner viscosity
      i=76                                      ! i=4*N-4, N =number of terms:
PI,C2,B2,D2,An,Cn,Bn,Dn...
      pi=3.141592653589793d0
      jj=181                                    ! number of nodes in shape profile
      j=1

      DO 81 n=1,jj
            READ(3,*) z(n), r(n)
            z(n)=z(n)
            r(n)=r(n)
 81   CONTINUE
```

```
          dt=0.025d0
          DO 100 t=0.d0,tf+.9*dt,dt                          ! time step incrementing
              V=0.0d0
              s(1)=0.0d0
              DO 101 n=2,jj
                  s(n)=s(n-1)+dsqrt((r(n)-r(n-1))**2+(z(n)-z(n-1))**2)
101           CONTINUE
              DO 102 n=1,jj
                  RR(n)=dsqrt(z(n)*z(n)+r(n)*r(n))
102           CONTINUE
              DO 98 l=1,i
              Tdeo(l)=0.d0
              sdeo(l)=0.d0
                  DO 99 m=1,i
                  Td2e(l,m)=0.d0
                      sd2e(l,m)=0.d0
99                CONTINUE
98            CONTINUE

              DO 103 n=2,jj-1
                  CALL LG1(n,i,z,RR,P,G) ! calculate Legendre and Gegenbauer polynomials
                  CALL FD(n,z,r,s,dr,dz,d2r,d2z)    ! calculate finite differences in geometry
                  CJ=dr*d2z-dz*d2r+dz/r(n)          ! calculate local shape curvature
                  DJ(n)=CJ
                  st=r(n)/RR(n)
                  ct=z(n)/RR(n)
                  sp=(z(n)*dz+r(n)*dr)/RR(n)
                  cp=(r(n)*dz-z(n)*dr)/RR(n)

                  ! calculate partial differentials, equations E4-E11
                  CALL PD(RR,ct,st,cp,sp,i,G,P,n,MIU,Min,dPRb,dPTb,dvR,dvT)
                  DO 104 l=1,i
                      deo(l)=CJ*(cp*dPRb(l)+sp*dPTb(l))*r(n)
                      Tdeo(l)=Tdeo(l)-(sdeo(l)+deo(l))/2.d0*(s(n)-s(n-1))
                          !"-" b/c need -Tdeo into gaussj subroutine
                      sdeo(l)=deo(l)
                      DO 105 m=1,i
                        d2e(m,l)=(dPRb(l)*dPRb(m)+dPTb(l)*dPTb(m)+dvR(l)*dvR(m)
     *                        +dvT(l)*dvT(m))*r(n)
                        Td2e(m,l)=Td2e(m,l)+(sd2e(m,l)+d2e(m,l))/2.d0*(s(n)-s(n-1))
                        sd2e(m,l)=d2e(m,l)
105               CONTINUE
104               CONTINUE
                  ! calculate volume to monitor continuity
                  V=V+pi/3.d0*(z(n)-z(n-1))*(r(n-1)**2+r(n)*r(n)+r(n)*r(n-1))

103           CONTINUE      ! location (nodal) incrementing

              DO 106 l=1,i
                      Tdeo(l)=Tdeo(l)-(deo(l)+0.d0)/2.d0*(s(n)-s(n-1))
                      DO 107 m=1,i
                          Td2e(m,l)=Td2e(m,l)+(d2e(m,l)+0.d0)/2.d0*(s(n)-s(n-1))
107               CONTINUE
106               CONTINUE
```

```
             CALL gaussj(Td2e,Tdeo,i,400)      ! gaussj - solve for unknown coefficient vector
             CALL VEL(Tdeo,i,RR,r,z,jj,vr,vz)  ! vel - solve velocities and increment shape

             D(j)=(z(jj)-z(1))           ! vector of length of drop along axisymmetric axis at time t
             TT(j)=t                     ! vector of corresponding time

             j=j+1

             PRINT *,t,V,D(j-1)
!            write z,r data at t=tf to file
             IF (t.ge.tf-0.005d0) then
             DO 901 n=1,jj
                     WRITE(9,200) z(n),r(n),s(n)/s(jj-1),DJ(n)
901          CONTINUE
             print *, 'z,r data written to file at t=', tf

             compute dt for final step if tf <t+dt
         endif
             IF ((t.gt.tf-dt+0.001).and.(t.lt.tf-0.001)) then
                     dt=tf-t
                     print *, 'the new dt increment is dt =  ', dt
             endif

!            increment shape (to give new shape at t+dt) for next iteration
             DO 108 n=1,jj
                     z(n)=z(n)+vz(n)*dt
                     r(n)=r(n)+vr(n)*dt
108          CONTINUE

100     continue             ! time incrementing

        DO 900 n=1,j-1
                WRITE(7,200) TT(n),D(n)
900     CONTINUE
        STOP
200     FORMAT (4(f19.16,1X))
999     format (3(d17.10,1x),i3)
        END                  !end of program

!!!!!!!!!!!!!!!!!!!!!!!!!!!!!!!!!!!!!!!!!!!!!!!!!!!!!!!!!!!!!!!!!!!!!!!!!!!!!!!!!!!!!!!!!!!!!!!!!!!!!!!!!!!!!!!!!!!!!!!!!!
        SUBROUTINE LG1(n,i,z,RR,P,G)
        IMPLICIT REAL*8 (a-h,o-z)
        INTEGER i,l,n
        DIMENSION z(200),RR(200),P(100),G(100)
        P(1)=z(n)/RR(n)
        G(1)=-P(1)
        l=2
        P(2)=((2*l-1)*P(1)*P(l-1)-(l-1))/(l+0.d0)
        G(2)=0.5d0*(1.d0-P(1)**2)
        DO 11 l=3,(i+4)/4
                P(l)=((2*l-1)*P(1)*P(l-1)-(l-1)*P(l-2))/(l+0.d0)
                G(l)=(P(l-2)-P(l))/(2*l-1.d0)
11      CONTINUE
        RETURN
        END
```

```
!!!!!!!!!!!!!!!!!!!!!!!!!!!!!!!!!!!!!!!!!!!!!!!!!!!!!!!!!!!!!!!!!!!!!!!!!!!!!!!!!!!!!!!!!!!!!!!!!!!!!!!!!!!!!!!!!!!!!!!!!!!!!!!!!!
      SUBROUTINE FD(n,z,r,s,dr,dz,d2r,d2z)
      IMPLICIT REAL*8 (a-h,o-z)
      DIMENSION z(200),r(200),s(200)
      INTEGER n
      REAL*8 dr,dz,d2r,d2z
      dr=(0.5d0)*((r(n+1)-r(n))/(s(n+1)-s(n))+(r(n)-r(n-1))
     *      /(s(n)-s(n-1)))
      dz=(0.5d0)*((z(n+1)-z(n))/(s(n+1)-s(n))+(z(n)-z(n-1))
     *      /(s(n)-s(n-1)))
      d2r=2.d0/(s(n+1)-s(n-1))*((r(n+1)-r(n))
     *      /(s(n+1)-s(n))-(r(n)-r(n-1))/(s(n)-s(n-1)))
      d2z=2.d0/(s(n+1)-s(n-1))*((z(n+1)-z(n))
     *      /(s(n+1)-s(n))-(z(n)-z(n-1))/(s(n)-s(n-1)))
      RETURN
      END
!!!!!!!!!!!!!!!!!!!!!!!!!!!!!!!!!!!!!!!!!!!!!!!!!!!!!!!!!!!!!!!!!!!!!!!!!!!!!!!!!!!!!!!!!!!!!!!!!!!!!!!!!!!!!!!!!!!!!!!!!!!!!!!!!!
      SUBROUTINE PD(RR,ct,st,cp,sp,i,G,P,n,MIU,Min,dPRb,dPTb,dvR,dvT)
      IMPLICIT REAL*8 (a-h,o-z)
      DIMENSION RR(200),dPRb(200),dPTb(200),G(100),P(100),dvR(200),dvT(200)
      INTEGER i,m,n,l
      REAL*8 ct,st,cp,sp,MIU,Min

      dPRb(1)=-Min*cp
              !wrt PI
      dPRb(2)=3.d0*Min*RR(n)*(2.d0*ct*cp+st*sp)             !wrt C2
      dPRb(3)=-3.d0*MIU*RR(n)**(-4)*(2.d0*ct*cp+st*sp)      !wrt B2
      dPRb(4)=-3.d0*MIU*RR(n)**(-2)*ct*cp                   !wrt D2

      dPTb(1)=-Min*sp                                       !wrt pi
      dPTb(2)=3.d0*Min*RR(n)*(st*cp+4.d0*ct*sp)             !wrt C2
      dPTb(3)=3.d0*MIU*RR(n)**(-4)*(ct*sp-st*cp)            !wrt B2
      dPTb(4)=0.d0                                          !wrt D2

      dvR(1)=0.d0                                           !wrt PI
      dvR(2)=-RR(n)*RR(n)*ct                                !wrt C2
      dvR(3)=RR(n)**(-3)*ct                                 !wrt B2
      dvR(4)=ct/RR(n)                                       !wrt D2

      dvT(1)=0.d0                                           !wrt PI
      dvT(2)=2.d0*RR(n)*RR(n)*st                            !wrt C2
      dvT(3)=RR(n)**(-3)/2.d0*st                            !wrt B2
      dvT(4)=-st/(RR(n)*2.d0)                               !wrt D2

!     w=3.0d0
      l=3
      DO 12 m=5,i-3,4
            dPRb(m)=2.d0*Min*RR(n)**(l-3)*(l*(l-2)*G(l)
     *      /st*sp-(l-2)*P(l-1)*cp)                                  !wrt Aw
            dPRb(m+1)=2.d0*Min*RR(n)**(l-1)*((l*l-1)*G(l)/st*sp
     *      -(l*l-3*l-1)/(l-1.d0)*P(l-1)*cp)                         !wrt Cw
            dPRb(m+2)=-2.d0*MIU*RR(n)**(-l-2)*((l+1)*P(l-1)*cp
     *      +(l*l-1)*G(l)/st*sp)                                     ! wrt Bw
            dPRb(m+3)=-2.d0*MIU*RR(n)**(-l)*((l*l+l-3)/(l+0.d0)*P(l-1)*cp
     *      +l*(l-2)*G(l)/st*sp)                                     ! wrt Dw
```

```
                dPTb(m)=2.d0*Min*RR(n)**(l-3)*(l*(l-2)*G(l)/st*cp+((l-1)
     *          *P(l-1)-l*G(l)*ct/(1.d0-ct*ct))*sp)                          !wrt Aw
                dPTb(m+1)=2.d0*Min*RR(n)**(l-1)*((l*l-1)*G(l)/st*cp+(l*(l+2)
     *          /(l-1.d0)*P(l-1)-(l+2)*G(l)*ct/(1.d0-ct*ct))*sp)             !wrt Cw
                dPTb(m+2)=2.d0*MIU*RR(n)**(-l-2)*((l*P(l-1)-(l-1)*G(l)
     *          *ct/(1.d0-ct*ct))*sp-(l*l-1)*G(l)/st*cp)                     !wrt Bw
                dPTb(m+3)=2.d0*MIU*RR(n)**(-l)*((l-3)*((l-1)/(l+0.d0)*P(l-1)
     *          -G(l)*ct/(1.d0-ct*ct))*sp-l*(l-2)*G(l)/st*cp)                !wrt Dw

                dvR(m)=-RR(n)**(l-2)*P(l-1)                                  !wrt Aw
                dvR(m+1)=-RR(n)**(l)*P(l-1)                                  !wrt Cw
                dvR(m+2)=RR(n)**(-l-1)*P(l-1)                                !wrt Bw
                dvR(m+3)=RR(n)**(-l+1)*P(l-1)                                !wrt Dw

                dvT(m)=l*RR(n)**(l-2)*G(l)/st                                !wrt Aw
                dvT(m+1)=(l+2)*RR(n)**(l)*G(l)/st                            !wrt Cw
                dvT(m+2)=(l-1)*RR(n)**(-l-1)*G(l)/st                         !wrt Bw
                dvT(m+3)=(l-3)*RR(n)**(-l+1)*G(l)/st                         !wrt Dw

      !         w=w+1.d0
                l=l+1
12    CONTINUE
      RETURN
      END
!!!!!!!!!!!!!!!!!!!!!!!!!!!!!!!!!!!!!!!!!!!!!!!!!!!!!!!!!!!!!!!!!!!!!!!!!!!!!!!!!!!!!!!!!!!!!!!!!!!!!!!!!!!!!!!!!!!!!!!!
      SUBROUTINE VEL(A,i,RR,r,z,jj,vr,vz)
      IMPLICIT REAL*8 (a-h,o-z)
      DIMENSION RR(200),r(200),z(200),G(100),P(100),vr(200),vz(200),
     *               A(100)
      INTEGER i,j,jj,m
      REAL*8 ct,st,cp,sp,w,vRn,vvRn,vTn,vvTn,vTns,vvTns
      DO 70 j=1,jj
                vRn=0.d0
                vTn=0.d0
                vTns=0.d0
                CALL LG1(j,i,z,RR,P,G)

                w=3.d0
                st=r(j)/RR(j)
                ct=z(j)/RR(j)
                DO 71 k=5,i-3,4
                        vvRn=(A(k)*RR(j)**(w-2.d0)+A(k+1)*RR(j)**w)*P(w-1.d0)
                  vvTns=(w*A(k)*RR(j)**(w-2.d0)+(w+2.d0)*A(k+1)*RR(j)**w)*G(w)
                        if (j.eq.1) then
                                vvTn=0.d0
                        elseif (j.eq.jj) then
                vvTn=0.d0
                        else
      vvTn=(w*A(k)*RR(j)**(w-2.d0)+(w+2.d0)*A(k+1)*RR(j)**w)*G(w)/st
                        endif
                        vRn=vRn+vvRn
                        vTns=vTns+vvTns
                        vTn=vTn+vvTn
                        w=w+1.d0
71              CONTINUE
```

```
                  vz(j)=(-A(2)*RR(j)**2*ct-vRn)*ct-(2.d0*A(2)*RR(j)**2
     *            *st*st+vTns)
                  vr(j)=(-A(2)*RR(j)**2*ct-vRn)*st+(2.d0*A(2)*RR(j)**2
     *            *st+vTn)*ct
 70       CONTINUE
          RETURN
          END
!!!!!!!!!!!!!!!!!!!!!!!!!!!!!!!!!!!!!!!!!!!!!!!!!!!!!!!!!!!!!!!!!!!!!!!!!!!!!!!!!!!!!!!!!!!!!!!!!!!!!!!!!!!!!!!!!!!!
          SUBROUTINE gaussj(a,b,n,np)
c    modified from Numerical Recipes (2nd ed) pp.30-31
          implicit real*8(a-h,o-z)
      INTEGER n,np,NMAX
      REAL*8 a(np,np),b(np)
      PARAMETER (NMAX=400)
      INTEGER i,icol,irow,j,k,l,ll,indxc(NMAX),indxr(NMAX),ipiv(NMAX)
      REAL*8 big,dum,pivinv
      do 11 j=1,n
        ipiv(j)=0
11    continue
      do 22 i=1,n
        big=0.d0
        do 13 j=1,n
          if(ipiv(j).ne.1)then
            do 12 k=1,n
              if (ipiv(k).eq.0) then
                if (dabs(a(j,k)).ge.big)then
                  big=dabs(a(j,k))
                  irow=j
                  icol=k
                endif
              else if (ipiv(k).gt.1) then
                pause 'singular matrix in gaussj'
              endif
12          continue
          endif
13      continue
        ipiv(icol)=ipiv(icol)+1
        if (irow.ne.icol) then
          do 14 l=1,nn
            dum=a(irow,l)
            a(irow,l)=a(icol,l)
            a(icol,l)=dum
14        continue
          dum=b(irow)
          b(irow)=b(icol)
          b(icol)=dum
        endif
        indxr(i)=irow
        indxc(i)=icol
        if (a(icol,icol).eq.0.d0) pause 'singular matrix in GAUSSJ'
        pivinv=1.d0/a(icol,icol)
        a(icol,icol)=1.d0
        do 16 l=1,n
          a(icol,l)=a(icol,l)*pivinv
16      continue
        b(icol)=b(icol)*pivinv
```

```
     do 21 ll=1,n
       if(ll.ne.icol)then
         dum=a(ll,icol)
         a(ll,icol)=0.d0
         do 18 l=1,n
           a(ll,l)=a(ll,l)-a(icol,l)*dum
18         continue
         b(ll)=b(ll)-b(icol)*dum
       endif
21     continue
22   continue
    do 24 l=n,1,-1
      if(indxr(l).ne.indxc(l))then
        do 23 k=1,n
          dum=a(k,indxr(l))
          a(k,indxr(l))=a(k,indxc(l))
          a(k,indxc(l))=dum
23        continue
      endif
24    continue
    return
    END
!!!!!!!!!!!!!!!!!!!!!!!!!!!!!!!!!!!!!!!!!!!!!!!!!!!!!!!!!!!!!!!!!!!!!!!!!!!!!!!!!!!!!!!!!!!!!!!!!!!!!!!!!!!!!!!!!
```

Appendix G

Numerical Approximation of Initial Extended Drop Shapes

The variational solution to the Stokesian model introduced in chapter 4 requires, as an input, the initial maximum shape of the extended drop under consideration. This shape is initially obtained from digitized photographs of the drop, by noting its contour, at a recovery time of $t = 0$ seconds. In the interest of simplifying the experimental procedure, relatively few contour data points are collected (typically less than 50) and recorded in cylindrical coordinates (r, z). However, it is necessary to provide many more nodal points to ensure that the numerical procedure is robust. The shape contour must be continuous and twice differentiable for the calculation of the drop mean curvature J (Appendix D). This continuity is accomplished by approximating the drop shape with an appropriate function.

Due to the axisymmetric nature of the drop recovery experiments, it is necessary that the fitted contour have an infinite slope at the axis of symmetry. Previous studies examining recoveries of drops, that were initially cylindrical (with hemispherical endcaps), fitted axisymmetric contours with cubic spline functions (Stone and Leal, 1989a). However, due to the unusual drop shapes observed in the present study (all drops display an inflection point in their contours), a cubic spline provides a poor representation and an alternate function is introduced. The computer program used to fit the experimental drop shapes follows the description of this function.

G.1 Description

To begin, consider the following transformation ζ to describe the drop contour

$$\zeta = \frac{2R}{L_0} - 1, \tag{G.1}$$

where L_0 is the maximum axial length of the drop (at time $t = 0$ seconds) and R is a spherical coordinate (figure 4.1). Note that as the drop contour intersects the axis of symmetry, where $R = 0.5L_o$, $\zeta = 0$. To satisfy the condition of infinite contour slopes at intersections with the axis of symmetry, this transformation must be constrained by

$$\frac{d\zeta}{d\theta} = 0 \qquad \text{at} \qquad \theta = 0, \pi. \tag{G.2}$$

Equation G.2 clearly shows the advantage of the transformation function (equation G.1) in that the slopes at the $\theta = 0$ and π (corresponding to the points at which the drop contour intersects the axis of symmetry) are now defined.

Note that at any point i on the drop contour can be described in spherical coordinates in terms of the cylindrical coordinates r and z,

$$R_i = \sqrt{(z_o - z_i)^2 + r_i^2}\,;$$
$$\theta_i = \arccos\left[\frac{(z_o - z_i)}{R_i}\right]. \tag{G.3a,b}$$

A typical experimental drop contour is shown in figure G.1 (circles). Due to the axisymmetric nature of the drop, only the half-contour ($r \geq 0$) is required. In addition, a discretized equation G.1 is plotted (circles) for the same contour data points (figure G.2).

To better represent the drop contour in a continuous fashion, the transformation function (equation G.1) is expanded in a Fourier sine series, such that at each point i,

$$\Phi_i = \sum_j a_j \sin(j\theta_i), \tag{G.4}$$

where a_j are constants to be determined. These constants may be solved for through the following function that assesses the deviation between the observed points ζ_i and the series approximation Φ_i,

$$\varepsilon = \sum_i \frac{1}{2} \cdot \left(\sum_j a_j \sin(j\theta_i) - \zeta_i \right)^2. \tag{G.5}$$

By expanding the partial derivative of this function (with respect to the unknown coefficients) in a first order Taylor series, this linear set of equations may be easily solved. However, the solution must incorporate the constraints (equations G.2) to ensure

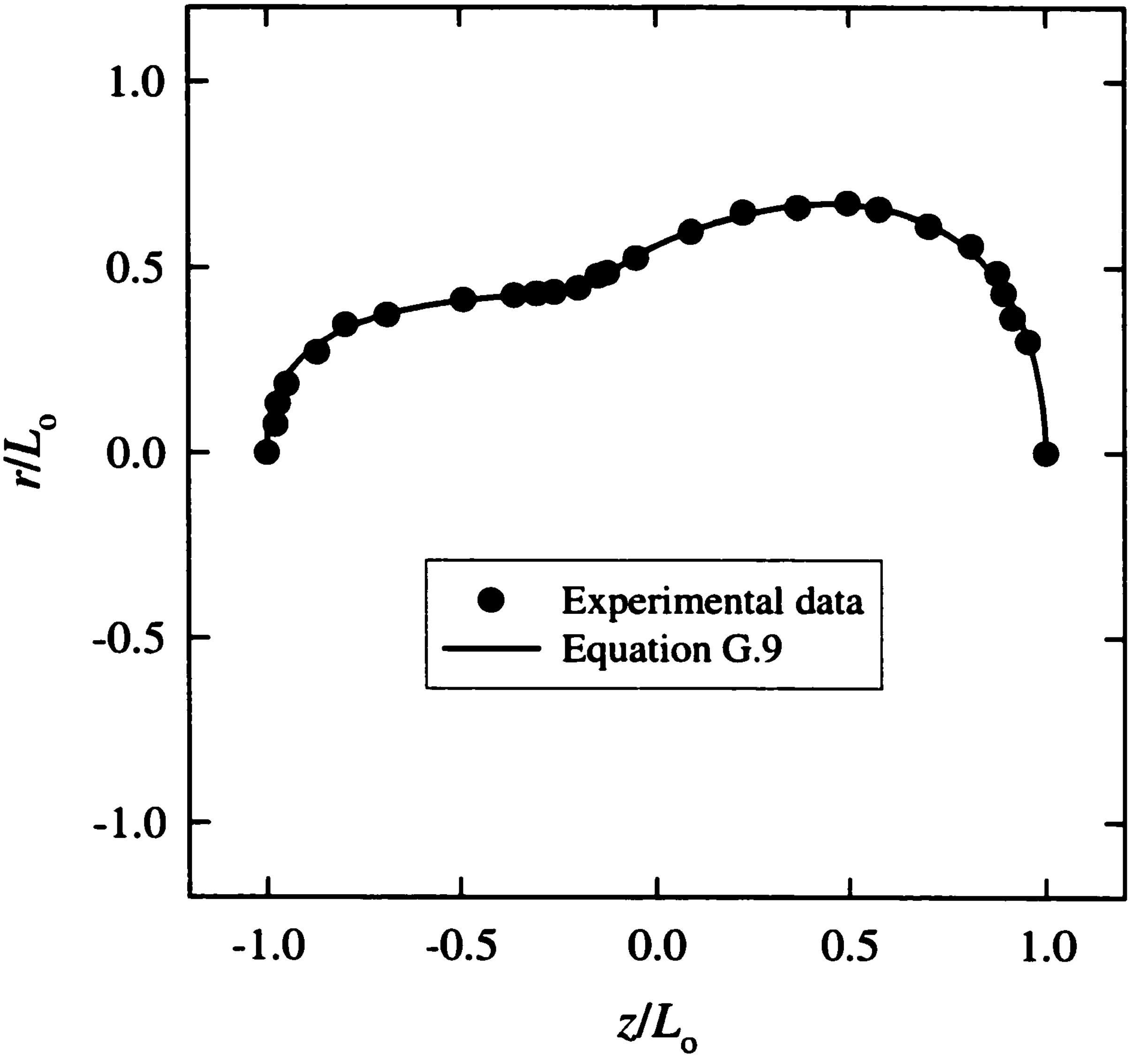

Figure G.1. Initial drop contour. Experimental data (solid symbols) depicting the drop contour is obtained in relatively few data points. This shape contour is then fit using a Fourier sine series (equation G.4) of a transformation function (equation G.1) and replotted (solid line) as a continuous function (equation G.9).

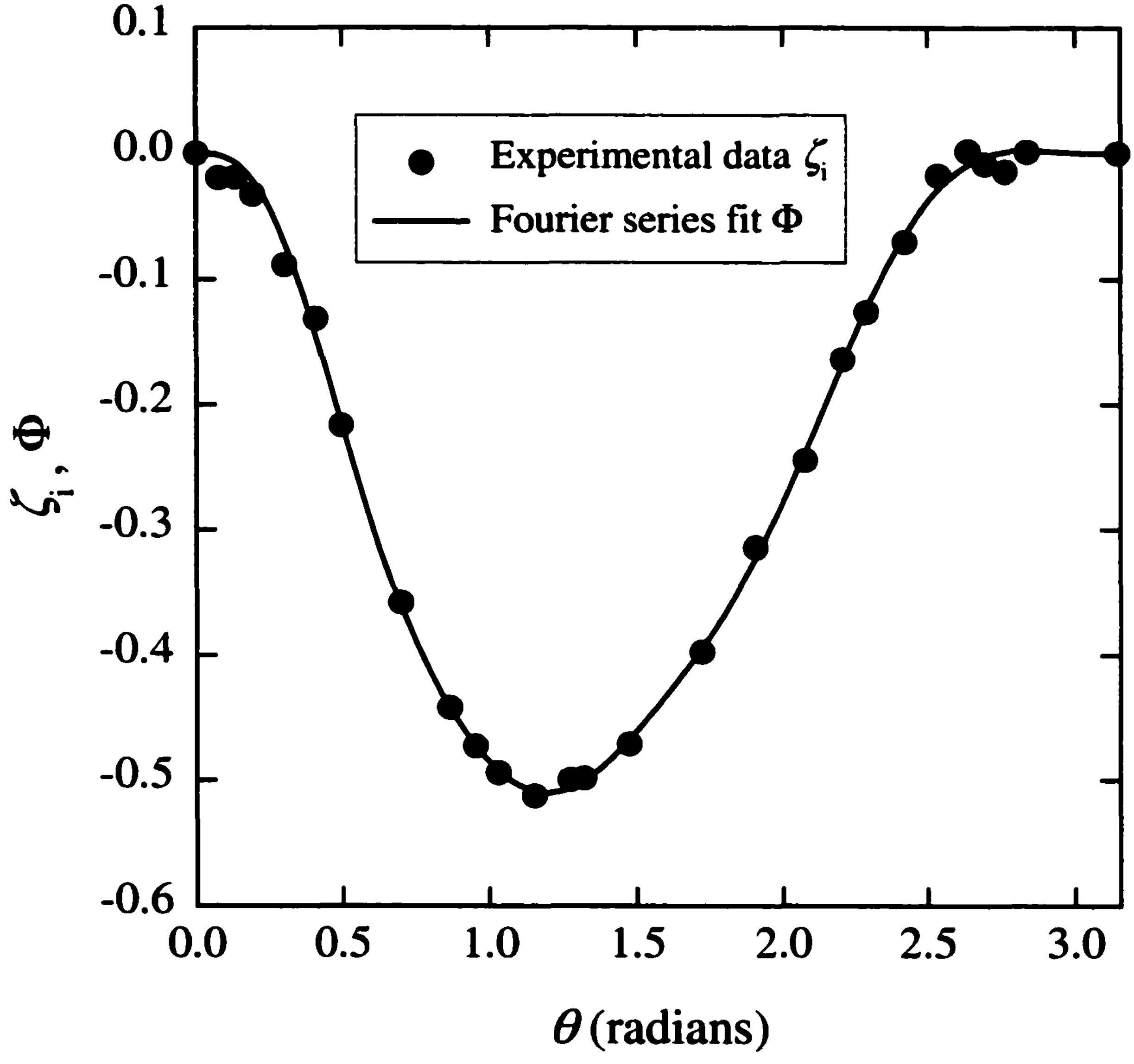

Figure G.2. Drop contour transformation function. The discretized transformation function ζ_i is plotted as a function of θ. Experimental data (solid symbols) is transformed by a discretized equation G.1. The Fourier sine series fit Φ (equation G.4) of the transformed experimental data indicates excellent agreement. This fit is optimized by recognizing boundary conditions stating that the slope of Φ is zero at $\theta = 0$ and π.

the appropriate conditions are observed. Thus, a modified function that must be minimized is introduced to allow for these constraints, giving

$$\varepsilon' = \varepsilon + \lambda_1 G_1 + \lambda_2 G_2, \tag{G.6}$$

where λ_1 and λ_2 are Lagrange multipliers. The functions G_1 and G_2 represent the two constraints (equations G.2) and are given as series solutions in terms of the unknowns a_j,

$$\begin{aligned} G_1 &= \frac{d\zeta}{d\theta}(0) = \sum_j j a_j = 0; \\ G_2 &= \frac{d\zeta}{d\theta}(\pi) = \sum_j (-1)^j j a_j = 0. \end{aligned} \tag{G.7}$$

As such, a system of linear algebraic equations may be set up allowing for the solution of the unknown constants. This linear system is of the following form

$$\left(\begin{array}{c|cc} \dfrac{\partial^2\varepsilon}{\partial a_m \partial a_n} & \dfrac{\partial G_1}{\partial a_n} & \dfrac{\partial G_2}{\partial a_n} \\ \hline \dfrac{\partial G_1}{\partial a_m} & 0 & 0 \\ \dfrac{\partial G_2}{\partial a_m} & 0 & 0 \end{array}\right) \cdot \left(\begin{array}{c} a_m \\ \hline \lambda_1 \\ \lambda_2 \end{array}\right) = -\left(\begin{array}{c} \left(\dfrac{\partial \varepsilon}{\partial a_m}\right)_o \\ \hline 0 \\ 0 \end{array}\right). \tag{G.8}$$

In this set of equations, $\left(\dfrac{\partial \varepsilon}{\partial a_m}\right)_o$ is evaluated at $\{a\} = 0$ in order to simplify the equations.

Once the constants a_j are uniquely determined, a continuous equation G.4 may be constructed over the range $0 \le \theta \le \pi$ (solid line in figure G.2). The continuous drop contour is calculated from the following equation,

$$R = \frac{L_o}{2} \cdot \left(1 + \sum_j a_j \sin(j\theta)\right) \tag{G.9}$$

in which $\{a\}$ are the optimized coefficients in the Fourier sine series (equation G.4). A typical fit of the drop contour is shown as the solid line in figure G.1. This continuous contour is then discretized into 181 nodal points (in cylindrical coordinates r, z) for input into the boundary least squares solution for the Stokesian model (chapter 4).

G.2 Computer Code

The fitting procedure described above is implemented with a computer program written in Matlab.

```
%%%%%%%%%%%%%%%%%%%%%%%%%%%%%%%%%%%%%%%%%%%%
% getshape
% Program getshape.m inputs axisymmetric drop shape data and produces a continuous description of such
% a shape contour.
%Written by Kevin Moran in Matlab V.5.2, March, 2000.
%%%%%%%%%%%%%%%%%%%%%%%%%%%%%%%%%%%%%%%%%%%%

% Read experimental input data
[file,path]=uigetfile('*.TXT','Load Experimental Geometric Shape Data');
if file ~= 0,
        fid = fopen(file,'r');
        G = fscanf(fid,'%g',[2,200]);
        expdata=G';
end
%%%%%%%%%%%%%%%%%%%%%%%%%%%%%%%%%%%%%%%%%%%%

% Dimensionalize input data to give rr, zz
L=abs((expdata(length(expdata),1)-expdata(1,1))); % length L of major (axisymmetric) axis
ttt=abs((expdata(length(expdata),1)-expdata(1,1))/L);          % cosine of incidence angle with z axis

zz=(expdata(:,1)/ttt-(min(expdata(:,1)/ttt)))/L;               % rescale length of drop on z axis
rr=abs((expdata(:,2)-expdata(1,2)))/L;                         % r coordinate of drop
rr=rr-rr(length(zz))*(zz-zz(1))/(zz(length(zz))-zz(1));        % correction to r for incidence angle
%%%%%%%%%%%%%%%%%%%%%%%%%%%%%%%%%%%%%%%%%%%%

% Define Transformation function and reexpress rr, zz data
z0=max(zz)/2;                                                  %define a reference point
RR=sqrt((zz-z0).^2+rr.^2);                                     % spherical coordinate relative to z0
th=acos((z0-zz)./RR);                                          %angle between RR and z axis
phi=RR/z0-1;                                                   %transformation function phi
%%%%%%%%%%%%%%%%%%%%%%%%%%%%%%%%%%%%%%%%%%%%

% Approximate transformation function via Fourier sine series and solve for sine series coefficients a
j=10;                                                          %# of terms in Fourier approximation of phi
dd2e=zeros(j+2);dde=zeros(j+2,1);
% calculate dd2e matrix and dde vector
for m=1:j
  dd2e(m,j+1)=m;
  dd2e(m,j+2)=m*(-1)^m;
  for i=1:length(zz)
     dde(m)=dde(m)-phi(i)*sin(m*th(i));
  end
  for n=1:j
    dd2e(j+1,n)=n;
    dd2e(j+2,n)=n*(-1)^n;
    for i=1:length(zz)
      dd2e(m,n)=dd2e(m,n)+sin(m*th(i))*sin(n*th(i));
    end
  end
 end
```

```
% Calculate a (coefficients in Fourier sine series) vector by matrix inversion
a=dd2e\(-dde)                                   % solve linear equations for a vector
%%%%%%%%%%%%%%%%%%%%%%%%%%%%%%%%%%%%%%%%

 % Calculate spherical coordinate R from a and Fourier sine series function pphi
 Rsum=0;tth=0:pi/180:pi;
  for m=1:j
   Rsum=Rsum+a(m)*sin(m*tth);                   % a(m) from FS series approximation
 end
 R=z0*(1+Rsum);

pphi=R/z0-1';
plot(th,phi,'+',tth,pphi)

% Calculate new 'continuous' coordinates r, z from Fourier series approximation
 r=R.*sin(tth);
 z=z0-R.*cos(tth)-1;

 zz=zz-1;
plot(zz,rr,'+',z,r)
g(:,1)= z';
g(:,2)= r';
%%%%%%%%%%%%%%%%%%%%%%%%%%%%%%%%%%%%%%%%

% Write new contour coordinates to file
[file,path]=uiputfile('*.txt','Save the Shape Data');
if file~=0
        eval(['save ',path,file,' g -ascii'])
end
%%%%%%%%%%%%%%%%%%%%%%%%%%%%%%%%%%%%%%%%
```